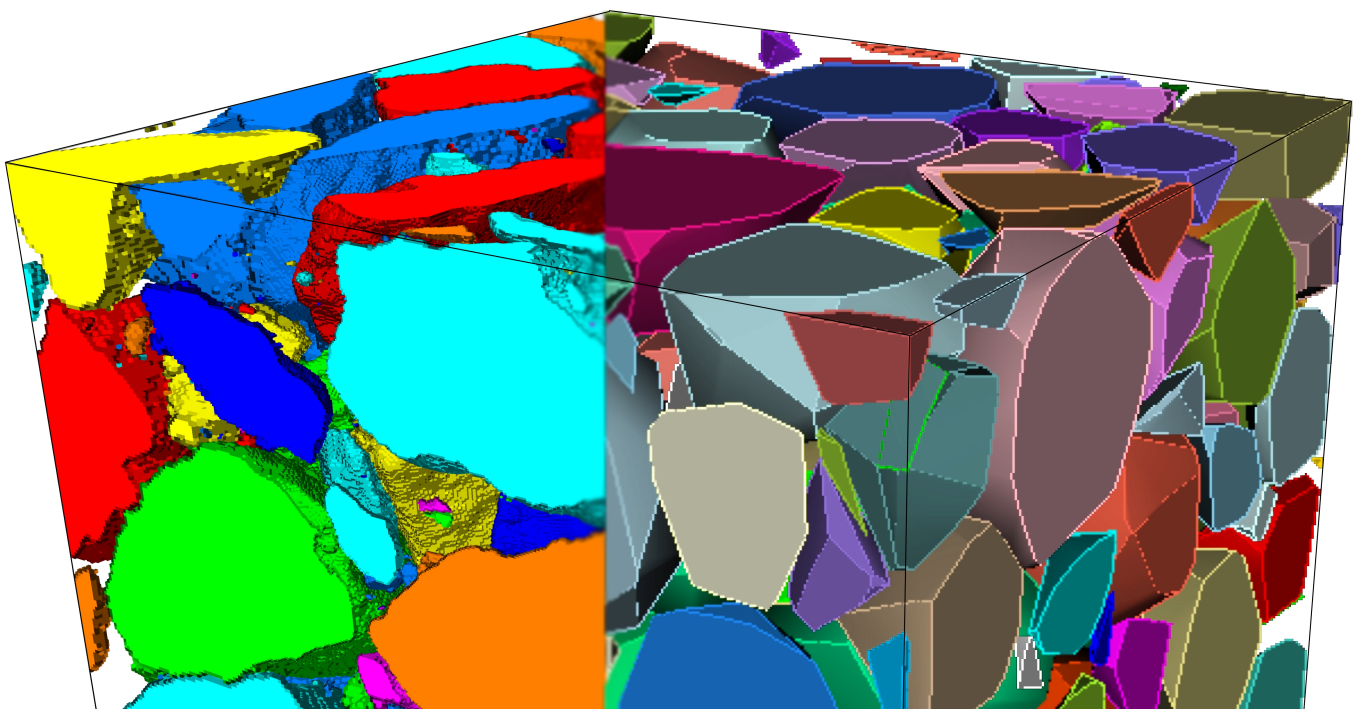


# Asphalt Concrete: Rheology, Microstructures and Numerical Simulations

Thorsten Schüler





# **Asphalt Concrete: Rheology, Microstructures and Numerical Simulations**

Dissertation  
zur  
Erlangung des Grades  
Doktor-Ingenieur

der  
Fakultät für Maschinenbau  
der Ruhr-Universität Bochum

von

**Thorsten Schüler**

aus Essen

Bochum 2017

Dissertation eingereicht am: 22.08.2017

Tag der mündlichen Prüfung: 07.11.2017

Erstgutachter: Prof. Dr.-Ing Holger Steeb

Zweitgutachter: Prof. Dr.-Ing Ralf Jänicke

Drittgutachter: Prof. Dr. rer. nat. Stefan Luding

# Danksagung

Die vorliegende Arbeit entstand hauptsächlich während meiner Tätigkeit am Lehrstuhl für Kontinuumsmechanik der Ruhr-Universität Bochum in den Jahren 2011 bis 2016. Diese Seite möchte ich nun nutzen, um all den Menschen zu danken, die zum Gelingen dieser Arbeit beigetragen haben.

Prof. Dr.-Ing. Holger Steeb möchte ich für die Möglichkeit der Promotion am Lehrstuhl und für die Betreuung meiner Arbeit danken. Ihr Optimismus, Ihre offene Art und Ihr Einsatz für die Forschung wird mir noch lange in Erinnerung bleiben.

Prof. Dr.-Ing. Ralf Jänicke möchte ich für die ständige Gesprächsbereitschaft und für die enge Betreuung meiner Arbeit danken. Du bist ein wirklich guter Lehrer, ohne Dich wäre ich wohl nicht so weit gekommen.

Prof. Dr. rer. nat. Stefan Luding möchte ich für das Interesse an meiner Arbeit und die Übernahme des Drittgutachtens danken.

Prof. Dr.-Ing. Martin Radenberg und Ricarda Manke möchte ich für die Unterstützung auf dem Gebiet der Straßenbautechnik und für die Bereitstellung der experimentellen Daten danken.

An dieser Stelle möchte ich mich auch bei meinen Bacheloranden und Masteranden bedanken, die ebenfalls zum Gelingen dieser Arbeit beigetragen haben. Insbesondere möchte ich mich hier bei Benjamin Dickhöver, Patrick Schmidt und Narendran Anumula bedanken, die mir sehr gut in Erinnerung geblieben sind.

Allen Kolleginnen und Kollegen am Lehrstuhl möchte ich natürlich auch Danke sagen. Zuallererst natürlich für die fachlichen Diskussionen und das tolle Arbeitsklima, aber auch für die schöne Zeit, die wir abseits der Forschung miteinander verbracht haben.

Meinen Eltern möchte ich insbesondere für die Unterstützung in den ersten Jahren des Studiums danken. Ihr habt es mir ermöglicht, mich auf mein Studium zu konzentrieren und trotzdem noch genug Zeit für andere Dinge im Leben zu haben.

Meiner Frau Sabrina möchte ich dafür danken, dass Sie mich immer bestärkt und nie den Glauben an mich verliert. Meiner Tochter Juna möchte ich danken, weil Sie mich jeden Tag aufs Neue begeistert und mir geholfen hat insbesondere in der finalen Phase der Arbeit nicht den Überblick zu verlieren. Ihr zeigt mir immer wieder, was das Wichtigste im Leben ist.



# Abstract

Asphalt concrete is a multi-component material with spatially varying constituents, typically consisting of a mineral filler (e.g. crushed rock), a bituminous binding agent, pores and further additives. In contrast to many other compounds used in materials science, the partial microscopic material bulk properties of the constituents of asphalt concrete can be considered to be well investigated and known and are accessible by physical testing. To predict apparent mechanical properties of such complex materials on the macroscopic level, a detailed knowledge of the micro-scale behavior of the particular constituents is required.

Within this thesis, asphalt concrete is investigated from different sides. Starting with bitumen-filler mastics with regard to the general master-curve relation from William, Landel and Ferry, an extension to this concept with regard to filler concentration is presented. This extension is based on experimental data for thermo-rheologically simple bitumen and bitumen-filler mastics and a mathematical procedure to define a function which holds as a shift function for varying filler concentrations and varying frequencies.

Furthermore, modeling aspects of the whole compound with regard to upscaling routines based on volume averaging are investigated. By using periodic microstructures, possible boundary layer effects during computational homogenization are minimized and in particular, the influence of the choice of micro-level boundary conditions on the apparent stiffness of the macro-level are investigated. With regard to this aspect, the apparent viscoelastic properties are as well discussed and analyzed in the frequency domain.

Special attention in this thesis is paid to a methodological framework to investigate the effective mechanical properties of asphalt concrete with consideration of realistic microstructures. The creation of artificial Statistical Volume Elements (SVEs) with a novel algorithm, which uses morphological informations from X-Ray Computed Tomography (XRCT) data or given granulometric curves from asphalt concrete specimens is presented. The algorithm combines a discrete particle simulation to generate a densely packed sphere model with a pre-defined Particle Size Distribution (PSD) for the mineral filler particles and in a second step a weighted Voronoi diagram, which is also capable of applying a stochastic shrinkage process of the Voronoi cells. Using these artificial microstructures for numerical simulations, helps to gain a better understanding of the prevalent physical phenomena and can help to trigger the real behavior of asphalt concrete.



# Kurzfassung

Asphalt ist ein Verbundwerkstoff aus mehreren Komponenten, mit unterschiedlichen Konstituenten. Typischerweise besteht Asphalt jedoch aus einem mineralischen Füllstoff (z.B. gebrochenem Gestein), einem bituminösen Bindemittel, Porenraum und verschiedenen weiteren Zuschlagsstoffen. Im Vergleich zu vielen anderen Verbundwerkstoffen in den Materialwissenschaften lassen sich die einzelnen Materialeigenschaften der Konstituenten von Asphalt sehr gut charakterisieren und experimentell bestimmen. Um die effektiven mechanischen Eigenschaften eines solch komplexen Materials auf makroskopischer Ebene zu bestimmen, ist ein detailliertes Wissen über die mikroskopischen Verhaltensweisen der einzelnen Konstituenten unabdingbar.

Innerhalb dieser Arbeit wird Asphalt von verschiedenen Seiten untersucht. Zuallererst werden Bitumen-Gestein Mischungen in Hinsicht auf das klassische Masterkurven-Konzept von William, Landel und Ferry mit einer Erweiterung für Füllerkonzentrationen untersucht. Diese Erweiterung basiert auf eigenen experimentellen Daten für thermo-rheologisch einfache Bitumen und Bitumen-Gestein Mischungen und einem mathematischen Ansatz zur Definition einer Funktion, welche die Abhängigkeit der Masterkurven für verschiedene Füllerkonzentrationen und verschiedene Frequenzen wiedergibt.

Des Weiteren werden Modellierungsaspekte des Asphalts in Hinsicht auf die Homogenisierung mithilfe der Volumenmittlung betrachtet. Bei dieser Betrachtung werden durch die Verwendung von periodischen Mikrostrukturen, mögliche Randeffekte während der Homogenisierung minimiert. Im speziellen wird dann auf den Einfluss der Wahl der Randbedingungen in Bezug zu den effektiven Eigenschaften auf der Makroebene eingegangen. In diesem Fall werden die effektiven viskoelastischen Eigenschaften auch im Frequenzraum analysiert und diskutiert.

Ein besonderes Augenmerk wird in dieser Arbeit auf den methodischen Rahmen für die Untersuchung von effektiven mechanischen Eigenschaften von Asphalt mit realitätsnahen Mikrostrukturen gelegt. Für die Erstellung der statistisch ähnlichen künstlichen Mikrostrukturen dient ein neuer Algorithmus, welcher als Informationsbasis Daten von einem Röntgencomputertomographen oder granulometrische Vorgaben verwerten kann. Die entwickelte Methode kombiniert eine Simulation diskreter Partikel unter Vorgabe der Kornverteilungskurve für die mineralischen Partikel mit einem gewichteten Voronoi Diagramm, welches als zusätzliche Funktion das stochastische Schrumpfen der Voronoi Zellen ermöglicht. Die numerische Simulation dieser künstlichen Mikrostrukturen führt zu einem besseren Verständnis der vorherrschenden physikalischen Phänomene, was dazu dient, die realen Eigenschaften von Asphalt besser zu steuern.



# Contents

<b>List of Figures</b>	<b>III</b>
<b>List of Tables</b>	<b>VII</b>
<b>1 Introduction</b>	<b>1</b>
1.1 Background and motivation . . . . .	1
1.2 Aims and outline . . . . .	3
<b>2 Theoretical aspects</b>	<b>5</b>
2.1 Kinematics . . . . .	5
2.2 Balance equations . . . . .	8
2.2.1 Balance of mass . . . . .	8
2.2.2 Balance of momentum . . . . .	9
2.2.3 Balance of moment of momentum . . . . .	9
2.2.4 Balance of energy . . . . .	9
2.2.5 Balance of entropy . . . . .	10
<b>3 Constitutive theory and material modeling</b>	<b>11</b>
3.1 Introduction . . . . .	11
3.2 Linear elastic solid . . . . .	12
3.3 Rheology of a viscoelastic solid/fluid . . . . .	13
3.3.1 Measurement methods . . . . .	24
3.3.2 Fitting . . . . .	26
3.4 Numerical realization . . . . .	27
<b>4 Extended master-curve concept for bitumen-filler mastics</b>	<b>31</b>
4.1 Introduction . . . . .	31
4.2 Material and methods . . . . .	33
4.3 Results and Discussion . . . . .	35
4.4 Conclusions . . . . .	41

<b>5</b>	<b>Multi-scale modeling of elastic/viscoelastic compounds</b>	<b>45</b>
5.1	Introduction . . . . .	46
5.2	Micro-scale modeling . . . . .	48
5.3	Macro-scale modeling by homogenization . . . . .	53
5.3.1	Microscopic Dirichlet boundary value problem – local stress relaxation test . . . . .	54
5.3.2	Microscopic Neumann boundary value problem – local creep test . . . . .	55
5.3.3	Effective viscoelastic properties on the macro-scale . . . . .	56
5.4	Viscoelastic properties on the effective scale . . . . .	56
5.4.1	Influence of the micro-scale boundary conditions . . . . .	57
5.4.2	Size of Representative Volume Element and effective properties of the compound . . . . .	61
5.5	Conclusions . . . . .	61
<b>6</b>	<b>Nonlinear modeling and computational homogenization of asphalt concrete on the basis of XRCT scans</b>	<b>65</b>
6.1	Introduction . . . . .	66
6.2	Material and methods . . . . .	69
6.2.1	XRCT data processing . . . . .	69
6.2.2	Generation of artificial microstructures . . . . .	73
6.3	Nonlinear viscoelastic properties on the effective scale . . . . .	79
6.3.1	Micro-scale modeling and homogenization . . . . .	79
6.3.2	3-dim nonlinear viscoelastic modeling approach . . . . .	81
6.3.3	Influence of the macroscopic loading velocity, and fluid-like properties of the mastic . . . . .	83
6.3.4	Nonlinear effects on the small scale and apparent macroscopic behavior . . . . .	85
6.4	Conclusions . . . . .	87
<b>7</b>	<b>Artificial microstructures on the basis of granulometric data</b>	<b>91</b>
7.1	Introduction . . . . .	91
7.2	Parameters for the discrete microstructure . . . . .	93
7.3	Results and Discussion . . . . .	94
<b>8</b>	<b>Conclusions and outlook</b>	<b>99</b>
<b>A</b>	<b>APPENDIX</b>	<b>103</b>
A.1	Linear-viscoelasticity . . . . .	103
	<b>Bibliography</b>	<b>106</b>
	<b>Curriculum Vitae</b>	<b>115</b>

# List of Figures

1.1	Schematic representation of a pavement structure to introduce different notions. . . . .	2
2.1	Reference and actual configuration of the body $\mathcal{B}$ . . . . .	6
3.1	Maxwell-Zener model. . . . .	13
3.2	Extension of the Maxwell-Zener model, the $(2n+1)$ -parameter model. .	17
3.3	3-dim extension of the Maxwell-Zener model. . . . .	18
3.4	Pure 20/30 penetration grade bituminous binding agent. a) Master-curve pinpointed with one Maxwell-Chain. b) Master-curve with three Maxwell-Chains to underline the fitting aspects. . . . .	27
3.5	Possible boundary conditions of body $\mathcal{B}$ . . . . .	29
4.1	a) Storage modulus $G'$ and b) loss modulus $G''$ for pure 20/30 penetration grade bituminous binder for six different temperatures in a frequency range $0.1 \text{ Hz} \leq f \leq 10 \text{ Hz}$ . . . . .	33
4.2	a) Dynamic modulus $ G^* $ for pure 20/30 penetration grade bituminous binder and b) the resulting master-curve. . . . .	34
4.3	Granulometric curve of the filler. . . . .	35
4.4	a) Master-curves of the dynamic modulus $ G^* $ and b) of the dynamic viscosity $ \eta^* $ for five different filler mass fractions $w^p$ . . . . .	36
4.5	WLF function on the basis of six different temperatures $\theta$ and five different filler mass fractions $w^p$ . . . . .	36
4.6	Shift factors $\beta_p$ in a double-logarithmic representation for the five different filler mass fractions $w^p$ with fitted linear regression functions for data set. . . . .	37
4.7	a) Linear function for slope $m$ and quadratic function for intercept $n$ . . . . .	38
4.8	3-dim view of the function for $\beta_p$ and the corresponding experimental data. . . . .	39
4.9	Storage modulus $G'$ for the elastic limit ( $f = 10^6 \text{ Hz}$ ) in comparison with lower and upper HS bounds. . . . .	39
4.10	Effective viscosity $\eta^R$ for the viscous fluid limit ( $f = 10^{-2} \text{ Hz}$ ) in comparison with different formulas taken from relevant literature. . . . .	40

4.11	a) Master-curve for storage modulus $G'$ and loss modulus $G''$ for pure 20/30 penetration grade bituminous binder. . . . .	43
4.12	a) Master-curves of storage modulus $G'$ and loss modulus $G''$ for five different filler mass fractions $w^p$ . . . . .	43
5.1	<b>a</b> Storage modulus $G'$ and <b>b</b> loss modulus $G''$ gained by DSR experiments for non-modified 20/30 binder. The results for six different temperatures in a frequency range from $10^{-1}$ Hz to $10^1$ Hz are shown. $\Theta = 20^\circ\text{C}$ is chosen as the reference temperature for the master-curve. . . . .	50
5.2	Experimental DSR results for the dynamic modulus $ G^* $ with master-curve (non-modified 20/30 binder). The characteristic frequencies for the generalized Maxwell-Zener model are indicated by the thin gray lines. . . . .	51
5.3	3-dim generalized Maxwell-Zener model. The incompressibility of the binder is considered due to the fact, that $K^i \gg G^i$ . . . . .	51
5.4	Each material point of the effective medium at position $\bar{\mathbf{x}}$ is identified with an attached micro-volume $V_\square$ at the local position $\Delta\mathbf{x} \ll \bar{\mathbf{x}}$ . . . . .	53
5.5	Effective shear strain state $\varepsilon_{12}$ for the different boundary conditions on the micro-level at state of equilibrium ( $t \rightarrow \infty$ ). <b>a</b> Linear displacement (Dirichlet) boundary conditions, <b>b</b> periodic boundary conditions (PBC) and <b>c</b> constant traction (Neumann) boundary conditions for identical effective shear deformation states $\langle \varepsilon_{12} \rangle$ . . . . .	58
5.6	Functions of <b>a</b> effective shear strain and <b>b</b> effective shear stress over the time $t$ . For linear displacement (Dirichlet) boundary conditions as well as for periodic boundary conditions (PBC), the shear test takes the form of a stress relaxation experiment. If constant traction (Neumann) boundary conditions are considered, the experiment is represented by a creep test. . . . .	58
5.7	<b>a</b> Effective storage modulus $\bar{G}'$ and <b>b</b> effective loss modulus $\bar{G}''$ by the different types of boundary conditions on the micro-level and the homogeneous pure binder. . . . .	59
5.8	Loss factor $\tan \bar{\delta}$ for the different boundary conditions and the homogeneous pure binder. . . . .	60
5.9	<b>a</b> Loss factor $\tan \bar{\delta}$ for four different numbers of particles under periodic boundary conditions. <b>b</b> Numerical results and master curve for the dynamic modulus $ \bar{G}^* $ with 7 particles. The first four characteristic frequencies for the generalized Maxwell-Zener model are indicated by the thin gray lines. . . . .	62
6.1	Different scales for asphalt concrete. . . . .	66
6.2	Raw data from the XRCT. Illustration in 3-dim in terms of orthogonal slices. Each voxel has a resolution of $24.5 \mu\text{m}$ . The white cubic frame ( $1000^3$ voxels $\hat{=} (24.5 \text{ mm})^3$ ) indicates the control volume for further analysis. . . . .	70

6.3	2-dim slices before a) and after b) applying the non-local means filter.	71
6.4	Visualisation of a) large intra-class variance, b) small inter-class variance and c) small intra-class variance in combination with a large inter-class variance. . . . .	71
6.5	Normalized histogram for a three phase asphalt concrete with phases $\varphi^g$ , $\varphi^f$ and $\varphi^s$ a) before and b) after applying the non-local means filter.	72
6.6	2-dim illustration of the a) mineral aggregates $\varphi^s$ , b) the bituminous binding agent $\varphi^f$ and c) a biphasic coloration of both. The black phase indicates air $\varphi^g$ . . . . .	72
6.7	3-dim illustration of the $1000^3$ voxel cube showing the a) mineral aggregates $\varphi^s$ , b) the bituminous binding agent $\varphi^f$ and c) a biphasic coloration of both constituents. . . . .	73
6.8	Graphical visualization of the Lubachevsky-Stillinger algorithm. The spherical particles $\mathcal{P}_i$ and $\mathcal{P}_j$ , $i, j = 1, 2, \dots, N$ , move within a unit cube $\mathcal{C}$ . Their radius is computed as $r_i(t) = g_i t$ with the individual but constant growth rate $g_i$ . . . . .	74
6.9	a) Final dense sphere packing structure and b) cumulative volume fraction of the dense sphere packing structure (Input model) and the Voronoi tessellation (Voronoi). The results are normalized to the maximum of the volume fraction $n^s$ . . . . .	75
6.10	a) Illustration of the stochastic shrinking of a corner point $k$ . The local coordinate $\mathbf{c}_k$ before and $\mathbf{c}_k^s$ after the shrinking process is evaluated with respect to the origin $\mathcal{O}_i$ of the Voronoi cell $V_i$ , $i = 1, 2, \dots, N$ , $k = 1, 2, \dots, N_c$ . The randomly chosen parameter $s_k$ represents the displacement of the corner position $\mathbf{c}_k$ towards $\mathcal{O}_i$ . b) Comparison of a 2-dim slice taken from a 3-dim dense sphere packing and the corresponding shrunk Voronoi cells. For some particles, the spheres are outside of the slice and only the shrunk cells are visible. . . . .	77
6.11	Unit cube (right-hand side) with periodic continuation (left-hand side).	78
6.12	a) $1000^3$ voxel cube from the XRCT scan and b) one random artificial counterpart from the Voronoi tessellation. . . . .	78
6.13	a) Experimental DSR results in a logarithmic plot for the dynamic modulus $ G^* $ with master-curve (first, non-modified 20/30 bituminous binding agent with $m^p/m^f = 0.65$ and, second, $m^p/m^f = 0.0$ ). The characteristic frequencies $f^i$ for the generalized Maxwell-Zener model are indicated by the vertical lines. b) Phase angle. . . . .	80
6.14	Three different states for the stress relaxations. The loading times range from $t^* = 1\text{E-}4\text{s}$ over $t^* = 1\text{E-}1\text{s}$ to $t^* = 1\text{E+}1\text{s}$ . The applied stretch is always $\bar{\lambda}_1 = 2.0$ . . . . .	84
6.15	Normalized deviation of the stress relaxation curves for three different stretches with respect to the geometrically nonlinear Neo-Hookean result.	85
6.16	Example mesh with approximately 2 Mio. degrees of freedom. . . . .	86

6.17	a) Strain boundary condition for the uniaxial pressure with a smooth step function. The maximum displacement of $\bar{H}_{11} = -0.02$ is reached after $t^* = 1\text{E-}3\text{s}$ , whilst all further components $\bar{H}_{ij} = 0, i, j = 1, 2, 3$ . b) Relaxation of the von Mises stress $\bar{T}_v$ for five different examples on the effective scale. . . . .	87
6.18	Maximum principal strain $E_{\max.} = \max(E_1, E_2, E_3)$ inside an example SVE under uniaxial pressure $\bar{H}_{11} = -0.02$ . . . . .	88
6.19	a) Stress relaxation for five different examples on the effective scale for simple shear boundary conditions with a smooth step function. The maximum displacement of $\bar{H}_{12} = 0.01$ is reached after $t^* = 1\text{E-}3\text{s}$ . b) Stress relaxation under uniaxial tension $\bar{H}_{33} = 0.02$ . . . . .	89
6.20	Normalized stress relaxation curve for different smooth step loads with $t^* = 1\text{E-}3\text{s}$ and $t^* = 1\text{E-}6\text{s}$ for one exemplary SVE. Both curves have an underlying set of three different strain boundary conditions: $\bar{H}_{12} = 0.01, \bar{H}_{12} = 0.001$ and $\bar{H}_{12} = 0.0001$ . . . . .	90
6.21	a) Difference of strain and b) difference of stress between the effective scale and a single integration point in the bituminous binding agent for the simple shear boundary condition. . . . .	90
7.1	a) The densely packed spheres after the Lubachevsky-Stillinger algorithm and their representation after the shrinking procedure of the weighted Voronoi diagram. b) The final microstructure for the mastic asphalt concrete MA8S with $N = 605$ discretely modeled particles. . .	96
7.2	Discretely modeled particles and requirements for a) the MA8S and b) the PA8 asphalt concrete. . . . .	97

# List of Tables

4.1	Mass fraction $w^p$ and volume fraction $n^p$ of the admixed filler. . . . .	35
5.1	Experimentally determined parameters of the generalized Maxwell-Zener model. . . . .	52
5.2	Determined parameters of the generalized Maxwell-Zener model for four characteristic frequencies under periodic boundary conditions on the effective scale. . . . .	61
6.1	Experimentally determined parameters of the generalized Maxwell-Zener model with consideration of $G^0 \approx 0$ MPa. . . . .	84
7.1	Mesh sizes and sieve values for MA8S and PA8 [1]. . . . .	92
7.2	Given values are marked with blue color, all other values are derived. . . . .	95
7.3	Discretely modeled particles. . . . .	95
7.4	Absolute values for MA8S and PA8 depending on the number of mineral aggregates. . . . .	96



# Chapter 1

## Introduction

### 1.1 Background and motivation

Asphalt concrete is well known to the general public since almost everybody has been in contact with asphalt concrete in some kind of way. What is not known to the general public is the fact that asphalt concrete is a highly complex material composite which can be constructed in a wide variety of shapes and sizes to fulfill different requirements. Due to the fact that asphalt concrete is used all over the world, the conditions under which the material needs to withstand different kinds of loads is huge. Asphalt concrete is used for road surfaces, airport start- and landing runways, parking lots and sidewalks, just to name a few. Considering the expected loads for these different applications and taking into account the different environmental influences all over the world will lead to a broad range of different asphalt concrete types.

From a scientific point of view, asphalt concrete requires to investigate it from many different sides, e.g. fatigue behavior, noise reduction, fluid absorption, to name only a few. All these investigations have in common that the first step is always a thorough understanding of the mechanical effects within the material, accompanied by the constitutive description and morphology. In general, an asphalt compound consists of three major constituents, namely stiff mineral aggregates, a soft viscoelastic binding agent and air-voids. Furthermore, it is built up by different layers as presented in Figure 1.1 [34, 89]. Many more additives can be used for the compound, but are strongly dependent on the application. Waxes and rubber parts are two of the more common additives which can be used for the overall compound [34].

As mentioned before, Figure 1.1 shows a schematic representation of the different layers of an asphalt concrete, typically used for road construction. It is to say that the construction again depends on the application and therefore the expected loads. The differences between base, binder and surface course lies in the different combination of mineral aggregates and bituminous binding agent. It usually ranges from large mineral aggregate sizes with low bituminous binding agent amount in the base course,

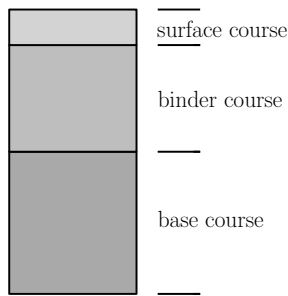


Figure 1.1: Schematic representation of a pavement structure to introduce different notions.

to small mineral aggregate sizes and high bituminous binding agent amount in the surface course. This thesis mainly deals with the surface course of the complete asphalt structure but its findings are also applicable to the other courses. As stated before, asphalt concrete is well known to the general public, so everybody can think of everyday problems like potholes or noise pollution. The investigation of the occurrence and its prevention for both conditions is vitally important. Considering the second point mentioned, noise reduction of roads in cities is highly interesting with an ever-increasing traffic density. The acoustic properties of different asphalt concrete types and their advantages and disadvantages needs to be investigated. Even though the investigation of potholes or acoustic properties is not mainly discussed in this thesis, it makes a contribution to the fundamental questions behind these phenomena. To get to the analysis of the two aforementioned topics, and these are only a few in the wide field of interest concerning asphalt concrete, a fundamental knowledge from a mechanical point of view about asphalt concrete is required. This thesis deals with some of these fundamental questions, like the transition from micro- to macro-scale behavior of asphalt concrete and the morphology of the compound to help understanding the inherent relations [72, 73]. The micro-scale is defined as the pre-scale of the compound, whereas the macro-scale is the directly visible scale of the whole component or in this case of the compound. Furthermore, this thesis deals with the abstraction of asphalt concrete to artificial structures for a more efficient way of numerical simulations [74, 75]. The before mentioned multi-scale modeling is one point that makes asphalt concrete so interesting. Unlike many other multi-scale materials, the behavior of the constituents within asphalt concrete can be characterized and modeled on the micro-scale level very accurately. Another very interesting point are large deformations on the micro-scale level and their possible influence on the macro-scale behavior. Large deformations in the bituminous binding agent occur due to the high stiffness difference compared to the mineral aggregates, which lead to relative distortions and dislocations of the mineral aggregates. In general it can be said that asphalt concrete is a very interesting material which is worth investigating and which gives room for potential development from a mechanical point of view. Especially with

regard to material modeling, asphalt concrete builds a perfect basis for application-oriented material design. The varying load conditions and requirements with respect to environmental influences and applications build such a large variety of applications that a suitable material design helps to fulfill the demands of the material.

## 1.2 Aims and outline

As partly touched in the previous section, the intention of this work is to get a deeper insight in the complexity of modeling asphalt concrete from a constitutive point of view, but also from a morphological point of view. Therefore, this work mainly focuses on two closely linked fields of interest. First, the constitutive modeling of the constituents of asphalt concrete, with special focus on the bituminous binding agent. Second, the morphological conditions within asphalt concrete and the numerical representation of these conditions. To get these topics covered, the work is structured in the following way:

- Required theoretical aspects for a better understanding of the topic are given in Chapter 2 and 3. Topics which are introduced are part of continuum mechanics and in detail kinematics, balance equations and constitutive modeling. The different parts are introduced from a mathematical and mechanical point of view.
- In Chapter 4, the rheology of bitumen-filler mastics with focus on general master-curve relations and an extension of this concept with regard to filler concentrations is provided. Based on experimental data for thermo-rheologically simple bitumen and bitumen-filler mastics a mathematical procedure is described to define a function which serves as a shift function enriching the time-temperature superposition principle by the content of filler particles.
- Chapter 5 is concerned with the requirements of an efficient multi-scale modeling approach for elastic/viscoelastic compounds such as bituminous asphalt concrete. Prediction of effective mechanical properties of such complex materials on the macroscopic level requires a detailed knowledge of the micro-scale behavior of the particular constituents. In this chapter, the focus lies on modeling aspects due to upscaling routines based on volume averaging and the influence of micro-level boundary conditions.
- Chapter 6 provides a methodological framework to investigate effective mechanical properties of asphalt concrete. Numerical tools based on morphological X-Ray Computed Tomography (XRCT) data from asphalt concrete specimen are used to create artificial Statistical Volume Elements (SVEs) for numerical simulations. A discrete particle simulation is applied to generate a densely packed sphere model with a pre-defined Particle Size Distribution (PSD) as a first representation of the mineral filler particles. This model serves as the starting point

for a weighted Voronoi diagram. Finally, the volume fractions are adjusted by a stochastic shrinkage process of the Voronoi cells. This chapter also focuses on the constitutive description of the bituminous binding agent, which we interpret as a viscoelastic fluid.

- Chapter 7 extends Chapter 6 with regard to artificial Statistical Volume Elements based on norms and standards instead of XRCT data. Based on one mastic asphalt (MA8S) and one porous asphalt (PA8), this chapter gives details about the calculations that are necessary to create microstructures for further mechanical or other simulation and highlights the flexibility of the algorithm.
- Finally, the main results of this investigation are summarized in Chapter 8 and an outlook is given for further possible research approaches.

To be noted is that parts of this work will be submitted for publication or are already published in scientific peer-reviewed journals. Chapter 4 will be submitted for publication in *Journal of Rheology*. The results of Chapter 5 are published in *Journal of Applied Mathematics and Mechanics* [72] and partly in *Proceedings in Applied Mathematics and Mechanics* [73]. Chapter 6 is the basis of a publication in *Construction and Building Materials* [75], whereas preliminary results of this chapter are published in *Proceedings in Applied Mathematics and Mechanics* [74].

# Chapter 2

## Theoretical aspects

*In this and the following chapter all relevant mathematical and mechanical aspects are presented, which are required to understand the basis of this work. This includes the three parts of continuum mechanics, e.g. [22, 25]*

- *kinematics,*
- *balance equations,*
- *constitutive modeling,*

*and in addition to these parts, the initial boundary value problem. Since this work deals in many ways with specific questions concerning material modeling, Chapter 3 expands this theoretical chapter and deals in particular with constitutive modeling and all relevant material laws for this thesis solely.*

### 2.1 Kinematics

Kinematics deals with the geometrical basics which describes movement and deformation of a body. Reasons for these movements and deformations are not yet scope of the theory. Looking at a material body  $\mathcal{B}$ , which simply acts as a collection of material points  $P$  in a 2-dim  $\mathbb{R}^2$  or 3-dim  $\mathbb{R}^3$  Euclidean space. The outer border of the body is defined as  $\partial\mathcal{B}$ . Each material point is given an exact position in a Cartesian coordinate system with basic vectors  $\mathbf{e}_i$ . First, the reference configuration is considered, which usually describes the undeformed state or the state at time  $t = t_0$ . In this case, the position of a specific material point out of the set of all points  $\mathcal{P}$  is described by the position vector  $\mathbf{X}$ . Of further interest is the position and deformation of the body  $\mathcal{B}$  to a specific time  $t > t_0$ . This state is called actual or current configuration of body  $\mathcal{B}$ . The position of all material points is again described via position vectors referring to the already introduced origin. Defined are these position vectors as  $\mathbf{x}$ .

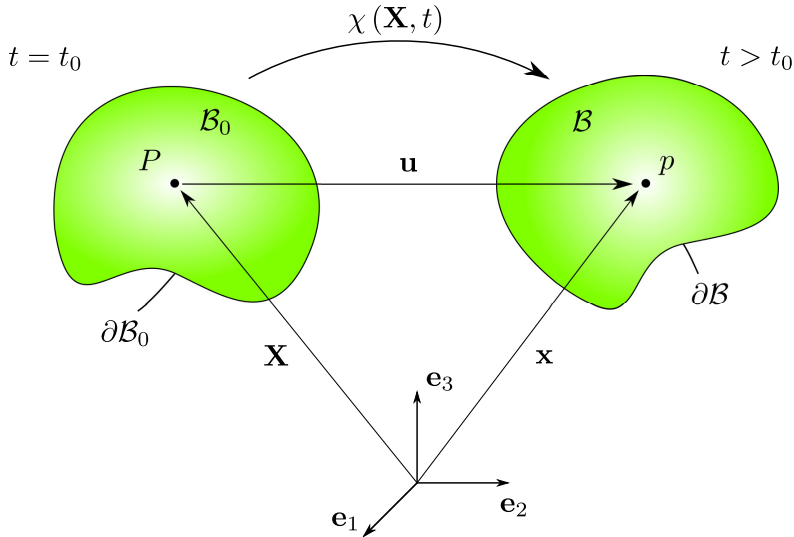


Figure 2.1: Reference and actual configuration of the body  $\mathcal{B}$ .

The position vector for the actual configuration is defined as a function of the position vector for the reference configuration

$$P \longrightarrow \mathbf{x} = \chi(\mathbf{X}, t) = \chi_t(\mathbf{X}). \quad (2.1)$$

With the parameter time  $t$ , the motion function  $\chi_t$  is introduced. This definition assigns a specific location to every material point within the Euclidean space. Using the Lagrangian description, at time  $t = t_0$  for the reference configuration, the motion function needs to fulfill

$$\mathbf{x} = \chi(\mathbf{X}, t_0). \quad (2.2)$$

Under the assumption that neighboring points always stay as neighboring points and a specific point can only be occupied by a single material point, the inversion of the motion function is possible

$$\mathbf{X} = \chi_t^{-1}(\mathbf{x}). \quad (2.3)$$

This formulation goes hand in hand with an Eulerian formulation. The motion or differently called the change from reference to actual configuration, is nothing else than a motion of all material points  $P$ , which can be described by the displacement vector  $\mathbf{u}$ . The displacement vector is the difference of the position vectors for the actual configuration  $\mathbf{x}$  at time  $t$  and the reference configuration  $\mathbf{X}$  at time  $t_0$ ,

$$\mathbf{u} = \mathbf{x} - \mathbf{X}, \quad (2.4)$$

$$\mathbf{u}(\mathbf{X}, t) = \mathbf{x}(\mathbf{X}, t) - \mathbf{X}. \quad (2.5)$$

Another important quantity for further investigations and definitions is the deformation gradient  $\mathbf{F}$

$$d\mathbf{x} = \mathbf{F} \cdot d\mathbf{X} \quad \Leftrightarrow \quad \mathbf{F} = \frac{d\mathbf{x}}{d\mathbf{X}} = \text{Grad } \mathbf{x}, \quad (2.6)$$

which transforms the line elements of the reference configuration  $d\mathbf{X}$  to line elements of the actual configuration  $d\mathbf{x}$ . The inverse of the deformation gradient is defined as

$$\mathbf{F}^{-1} = \frac{d\mathbf{X}}{d\mathbf{x}} = \text{grad } \mathbf{X}. \quad (2.7)$$

Based on the deformation gradient, transformations for infinitesimal surface and volume elements from the reference to the actual configuration are defined as

$$d\mathbf{a} = J \mathbf{F}^{-T} \cdot d\mathbf{A}, \quad (2.8)$$

for surface elements and as

$$dv = J dV \quad \text{with} \quad J = \det \mathbf{F} > 0 \quad (2.9)$$

for volume elements. The limitation for positive determinants of the deformation gradient guarantees the inverse map of the volume elements and prevents a self-penetration by only positive volume elements.

Based on the above introduced motion function, a velocity  $\mathbf{v} = \dot{\mathbf{x}}(\mathbf{x}, t)$  and an acceleration  $\mathbf{a} = \ddot{\mathbf{x}}(\mathbf{x}, t)$  in an Eulerian description are introduced. A corresponding Lagrangian description is also possible and reads

$$\mathbf{v} = \dot{\mathbf{x}}(\mathbf{X}, t = 0) = \frac{\partial \chi(\mathbf{X}, t_0)}{\partial t} \quad \text{and} \quad \mathbf{a} = \ddot{\mathbf{x}}(\mathbf{X}, t = 0) = \frac{\partial^2 \chi(\mathbf{X}, t_0)}{\partial t^2}. \quad (2.10)$$

The material time derivative of an arbitrary field quantity  $[\Psi]$  is defined by

$$\dot{\Psi} = \frac{\partial \Psi}{\partial t} + \text{grad } \Psi \cdot \dot{\mathbf{x}}, \quad (2.11)$$

which describes the temporal change of a material point of the field quantity  $[\Psi]$ , observed from a spatial position, meaning  $\mathbf{X}$  is fixed. The first part of the equation defines the intrinsic variation of the field quantity, whereas the second part defines the convective derivative, which describes the change due to transport of the field quantity. With regard to a linear description, the convective derivative is not considered and therefore neglected.

The velocity of the body  $\mathcal{B}$  is further defined by introducing a velocity gradient in a material description

$$\mathbf{L} = \text{Grad } \mathbf{v} = \dot{\mathbf{F}} \quad (2.12)$$

and a spatial description

$$\mathbf{l} = \text{grad } \mathbf{v} = \dot{\mathbf{F}} \cdot \mathbf{F}^{-1}, \quad (2.13)$$

using a Push-Forward transformation. The additive decomposition, here only shown for the spatial description, leads to a symmetric part  $\mathbf{d}$  and skew-symmetric part  $\mathbf{w}$

$$\mathbf{l} = \mathbf{d} + \mathbf{w} = \frac{1}{2}(\mathbf{l} + \mathbf{l}^T) + \frac{1}{2}(\mathbf{l} - \mathbf{l}^T). \quad (2.14)$$

With regard to deformation tensors, the right Cauchy-Green deformation tensor

$$\mathbf{C} = \mathbf{F}^T \cdot \mathbf{F} \quad (2.15)$$

of the reference configuration and the left Cauchy-Green deformation tensor

$$\mathbf{B} = \mathbf{F} \cdot \mathbf{F}^T \quad (2.16)$$

of the actual configuration is introduced. In a further step, the Green-Lagrange strain tensor

$$\mathbf{E} = \frac{1}{2}(\mathbf{C} - \mathbf{I}) \quad (2.17)$$

with

$$\mathbf{I} = \delta_{ij} \mathbf{e}_i \otimes \mathbf{e}_j, \quad (2.18)$$

$$\delta_{ij} = 1 \quad \forall \quad i = j \quad \text{and} \quad \delta_{ij} = 0 \quad \forall \quad i \neq j \quad (2.19)$$

and the Euler-Almansi tensor

$$\mathbf{A} = \frac{1}{2}(\mathbf{I} - \mathbf{B}^{-1}) \quad (2.20)$$

can be introduced as strain tensors of the reference or actual configuration, respectively. Any further theoretical background concerning kinematics can be found in many relevant literature, for example in [22, 25].

## 2.2 Balance equations

In this section the basic balance equations are introduced and the most important parts for this work are discussed. In classic continuum mechanics five balance relations are of importance, mass, momentum, moment of momentum, energy and entropy.

### 2.2.1 Balance of mass

Within this thesis the mass of the material body is assumed to be constant. No gain or loss of mass is assumed. With spatial density  $\rho = \rho(\mathbf{x}, t)$  related to volume elements of the actual configuration  $dv$  and material density  $\rho_0 = \rho_0(\mathbf{X}, t)$  related to volume elements of the reference configuration  $dV$ , the balance of mass reads

$$m = \int_B \rho \, dv = \int_{B_0} \rho_0 \, dV = \text{const.} \quad (2.21)$$

The change in density can be derived via  $\rho_0 = J\rho$ . Using the material time derivative  $\dot{m}$  of the complete mass and with  $\dot{J} = J \operatorname{div} \dot{\mathbf{x}}$  the local form of the balance of mass reads

$$\dot{\rho} + \rho \operatorname{div} \dot{\mathbf{x}} = 0. \quad (2.22)$$

### 2.2.2 Balance of momentum

The balance of momentum is an important balance equation. The underlying idea is Newton's Axiom which is equivalent to the formulation that the sum of all acting forces on a body  $\mathcal{B}$  is equal to the change in momentum

$$\frac{d}{dt} \int_{\mathcal{B}} \rho \dot{\mathbf{x}} \, dv = \int_{\partial \mathcal{B}} \mathbf{t} \, da + \int_{\mathcal{B}} \rho \mathbf{b} \, dv. \quad (2.23)$$

Here  $\rho \mathbf{b}$  are body forces. The before mentioned momentum is the product of the density  $\rho$  and the velocity  $\dot{\mathbf{x}}$  of the body  $\mathcal{B}$ . The relation between the Cauchy stress tensor  $\mathbf{T}$  and the normal vector  $\mathbf{n}$  is called Cauchy Theorem and reads

$$\mathbf{t} = \mathbf{T} \cdot \mathbf{n}. \quad (2.24)$$

Using the divergence theorem, the balance of mass and the consideration of individual areas of the body  $\mathcal{B}$  leads to the local form of the balance of momentum

$$\rho \ddot{\mathbf{x}} = \operatorname{div} \mathbf{T} + \rho \mathbf{b}. \quad (2.25)$$

### 2.2.3 Balance of moment of momentum

Next to the balance of momentum, the balance of moment of momentum is also based on Newton's Axiom and balances the change of the moment of momentum with the moment of external forces, it reads

$$\frac{d}{dt} \int_{\mathcal{B}} \rho \mathbf{x} \times \dot{\mathbf{x}} \, dv = \int_{\mathcal{B}} \rho \mathbf{x} \times \mathbf{b} \, dv + \int_{\partial \mathcal{B}} \mathbf{x} \times \mathbf{t} \, da. \quad (2.26)$$

The local form of the balance of moment of momentum leads to symmetry of Cauchy's stress tensor

$$\mathbf{T} = \mathbf{T}^T. \quad (2.27)$$

### 2.2.4 Balance of energy

The balance of energy states in accordance to the first law of thermodynamics that the energy of a material body changes with external power, which can be either mechanical or thermal. The global energy balance reads

$$\frac{d}{dt} \int_{\mathcal{B}} \rho \left( e + \frac{1}{2} \dot{\mathbf{x}} \cdot \dot{\mathbf{x}} \right) \, dv = \int_{\mathcal{B}} \rho (\mathbf{b} \cdot \dot{\mathbf{x}} + r) \, dv + \int_{\partial \mathcal{B}} (\mathbf{t} \cdot \dot{\mathbf{x}} - q) \, da, \quad (2.28)$$

with the heat flux  $q$  defined by the theorem

$$q = \mathbf{q} \cdot \mathbf{n}, \quad (2.29)$$

including the heat flux vector  $\mathbf{q}$ . The sign of the heat flux  $q$  in Eq. (2.28) is determined based on the direction of the unit vector  $\mathbf{n}$ . With  $\mathbf{n}$  pointing outwards,  $q$  is defined as heat outflux. The right side of Eq. (2.28) shows the before mentioned mechanical

$$\mathcal{P} = \int_{\mathcal{B}} \rho \mathbf{b} \cdot \dot{\mathbf{x}} \, dv + \int_{\partial \mathcal{B}} \mathbf{t} \cdot \dot{\mathbf{x}} \, da \quad (2.30)$$

and thermal

$$\mathcal{Q} = \int_{\mathcal{B}} \rho r \, dv + \int_{\partial \mathcal{B}} -q \, da \quad (2.31)$$

parts of the power, with  $r$  being the energy source. On the left side,  $e$  reflects the mass-specific inner part of the energy. The local form derived by using the divergence theorem reads

$$\rho \dot{e} = \mathbf{T} : \mathbf{d} + \rho r - \operatorname{div} \mathbf{q}. \quad (2.32)$$

## 2.2.5 Balance of entropy

The balance of entropy can be described using the basic principle of an inequality, which formulates that the entropy production  $\hat{\eta}$  of a material body may not be negative,

$$\rho \dot{\eta} + \operatorname{div} \left( \frac{\mathbf{q}}{\theta} \right) - \frac{\rho r}{\theta} = \hat{\eta} \geq 0. \quad (2.33)$$

Within this inequality,  $\dot{\eta}$  is introduced as the change of entropy and  $\theta$  is introduced as the temperature. By using the Helmholtz free energy

$$\Psi = e - \theta \eta \quad (2.34)$$

and its formulation in dependency of  $\Psi$  and  $\theta$ , the Clausius-Duhem inequality is introduced based on Eq. (2.33) as

$$-\rho \dot{\Psi} - \rho \eta \dot{\theta} - \frac{\mathbf{q}}{\theta} \cdot \operatorname{grad} \theta + \mathbf{T} : \mathbf{d} \geq 0, \quad (2.35)$$

for the actual configuration. With regard to this thesis and only isothermal processes with  $\theta = \text{constant}$ , the Clausius-Planck inequality is derived from the Clausius-Duhem inequality and reads

$$\mathbf{T} : \mathbf{d} - \rho \dot{\Psi} \geq 0. \quad (2.36)$$

This last equation is used for the constitutive modeling of the viscoelastic material, which is introduced in the next chapter.

## Chapter 3

# Constitutive theory and material modeling

*This chapter is concerned with theoretical aspects of constitutive theory and material modeling. Within the constitutive theory the connection between deformations of a body and the body forces inside and outside of the body are established. In the previous sections 2.1 and 2.2, the kinematic relationships and the balance equations are introduced, which are universal for the defined body. The constitutive theory enables to define different material behavior by using different constitutive equations, which leads at the same time to material modeling. In addition to the already mentioned literature, the contributions [30, 80, 91], serve as a good background for this chapter.*

### 3.1 Introduction

The scientific field of material modeling deals with the development of a phenomenological model, which describes the mechanical properties of a material. In many numerical applications the quality of the results strongly depend on the correctness of the theoretical model. The overall goal of all developed material models is the preferably exact description of the complex mechanical behavior of the material. In this work, two materials are of main focus, the bituminous binder and the solid aggregates. The solid aggregates are interpreted as linear elastic isotropic solids, whose modeling is rather simple compared to modeling the bituminous binder. The bituminous binder is interpreted as a viscoelastic fluid, whose modeling will be a main focus in this thesis. Both material models have in common that the starting points are material data taken from reliable, but different sources. Namely these are literature and own experimental data.

Another important term which needs a short introduction is the term rheology. Rhe-

ology is the study of the deformation and flow of matter in response to applied forces. For the general modeling of material behavior, rheology is based on three different elements, the elastic element (Hooke's body), the viscous element (Newton's body) and the plastic element. The plastic element is not considered in this thesis and is therefore not scope for this theoretical background chapter. Therefore, the next sections deal with the elastic and viscous element in more detail. The chapter closes with the numerical realization of the introduced material models.

## 3.2 Linear elastic solid

When looking at solid bodies at the state of small deformations, the theory of linear elasticity is applied. In this theory, Robert Hooke described the relationship between stress and strain. For a linear elastic solid and under the assumption of small deformation and isotropy,

$$\boldsymbol{\sigma} = 2G \boldsymbol{\varepsilon} + \lambda (\text{tr } \boldsymbol{\varepsilon}) \mathbf{I} \quad (3.1)$$

defines the 3-dim dependency between stresses and strains. Here,  $\boldsymbol{\varepsilon}$  is the linearized strain tensor,  $G$  the shear modulus,  $\lambda$  the Lamé parameter and  $\mathbf{I}$  the unity tensor.  $\text{tr } \boldsymbol{\varepsilon}$  is the trace of the strain tensor which is defined by

$$\text{tr } \boldsymbol{\varepsilon} = \varepsilon_{ii}. \quad (3.2)$$

The linearized strain tensor reads

$$\boldsymbol{\varepsilon} = \frac{1}{2} [\text{grad } \mathbf{u} + (\text{grad } \mathbf{u})^T]. \quad (3.3)$$

The elastic modulus  $E$  and the Poisson's ratio  $\nu$  can be calculated based on the shear modulus  $G$  and the Lamé parameter  $\lambda$  as

$$E = \frac{G(3\lambda + 2G)}{\lambda + G} \quad (3.4)$$

and

$$\nu = \frac{\lambda}{2(\lambda + G)}. \quad (3.5)$$

The inverse calculation is possible as well, but not further mentioned here. In addition, the bulk modulus is defined as

$$K = \lambda + \frac{2G}{3}. \quad (3.6)$$

For a simple load case, such as uniaxial tension, Eq. (3.1) simplifies to

$$\boldsymbol{\sigma} = E \boldsymbol{\varepsilon}. \quad (3.7)$$

This equation is independent of time and based on the observations from linear springs

$$F = c x. \quad (3.8)$$

In this equation  $c$  is a constant factor, characteristic of the spring which is comparable to the elastic modulus  $E$ , so its stiffness.  $F$  is the force that is needed to extend or compress the spring by some distance  $x$ , where  $x$  is small compared to the possible complete deformation of the spring. Especially in section 3.3 this relationship becomes even more important when modeling linear viscoelastic solids and fluids. Similar to the uniaxial tension case a proportionality for a simple shear load case can be described as well. With shear stress  $\tau$  proportional to shearing angle  $\gamma$ , the equation reads

$$\tau = G \gamma. \quad (3.9)$$

### 3.3 Rheology of a viscoelastic solid/fluid

As described in the previous section, the constitutive behavior of an elastic solid is characterized by the elasticity constants. With regard to viscoelastic materials, this behavior is enriched by a viscous behavior which needs to be considered when describing the more complex overall behavior in material models. For a simple linear

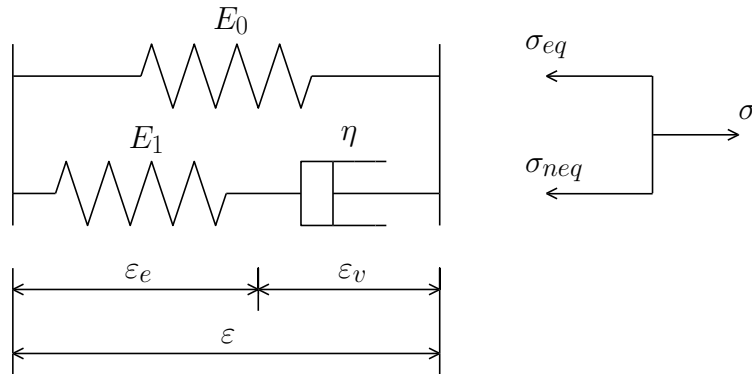


Figure 3.1: Maxwell-Zener model.

viscoelastic solid, the material model is known as Maxwell-Zener model [80]. This model is shown in Figure 3.1 and visualizes that the model consists of a Maxwell-element and a single spring in parallel. The mentioned Maxwell-Element is a series connection of a spring and a dashpot, which will be introduced as the viscous element or Newton's body. For the exact description of most viscoelastic materials, the Maxwell-Zener model is not sufficient and the model needs to be extended, but for the purpose of a theoretical background, this simple model is considered first and extended later in this section.

Referring to Figure 3.1 the overall stress  $\sigma$  consists of an equilibrium part  $\sigma_{eq}$  and a non-equilibrium part  $\sigma_{neq}$

$$\sigma = \sigma_{eq} + \sigma_{neq}. \quad (3.10)$$

The equilibrium part  $\sigma_{eq}$  is triggered by the spring with stress

$$\sigma_{eq} = E_0 \varepsilon \quad (3.11)$$

and the non-equilibrium part by the Maxwell-element (spring and dashpot)

$$\sigma_{neq} = E_1 \varepsilon_e = \eta \dot{\varepsilon}_v. \quad (3.12)$$

The overall strain of the model is made up of the elastic strain from the spring and the inelastic strain of the dashpot

$$\varepsilon = \varepsilon_e + \varepsilon_v. \quad (3.13)$$

The time derivative of  $\sigma$  reads

$$\dot{\sigma} = E_0 \dot{\varepsilon} + E_1 (\dot{\varepsilon} - \dot{\varepsilon}_v), \quad (3.14)$$

with

$$\dot{\varepsilon}_v = \frac{1}{\eta} \sigma_{neq} \quad (3.15)$$

$$= \frac{\sigma - \sigma_{eq}}{\eta} \quad (3.16)$$

$$= \frac{1}{\eta} (\sigma - E_0 \varepsilon) \quad (3.17)$$

$$= \frac{1}{\eta} (E_0 \varepsilon + E_1 (\varepsilon - \varepsilon_v) - E_0 \varepsilon) \quad (3.18)$$

$$= \frac{E_1}{\eta} (\varepsilon - \varepsilon_v). \quad (3.19)$$

The last equation shows the evolution equation of the Maxwell-Zener model. Going back to the time derivative of  $\sigma$  in Eq. (3.14), the evolution equation in the form  $\dot{\varepsilon}_v = \frac{1}{\eta} (\sigma - E_0 \varepsilon)$ , helps to derive a differential equation by inserting the same, which leads to

$$\dot{\sigma} = E_0 \dot{\varepsilon} + E_1 \left( \dot{\varepsilon} - \frac{1}{\eta} (\sigma - E_0 \varepsilon) \right) \quad (3.20)$$

$$\dot{\sigma} = (E_0 + E_1) \dot{\varepsilon} - E_1 \frac{1}{\eta} (\sigma - E_0 \varepsilon) \quad (3.21)$$

$$\dot{\sigma} + \frac{E_1}{\eta} \sigma = (E_0 + E_1) \dot{\varepsilon} + \frac{E_0 E_1}{\eta} \varepsilon. \quad (3.22)$$

This is the first order differential equation of the Maxwell-Zener model with the relaxation time

$$T_1 = \frac{\eta}{E_1}. \quad (3.23)$$

Considering the evolution equation in Eq. (3.19) for the given differential equation of the Maxwell-Zener model, cf. Eq. (3.22), the concept of internal variables needs to be used [50]. Internal variables in form of ordinary differential equations help to derive the stress answer of the system. The concept of internal variables can also be used for more complex material behavior, where more than one Maxwell-Chain is implemented, and for 3-dim material models. To solve the initial value problem for the differential equation, The Backward Euler method can be used. This leads to an implicit description of Eq. (3.19), which reads

$$\frac{(\varepsilon_v)_{n+1} - (\varepsilon_v)_n}{\Delta t} = \frac{1}{T_1} ((\varepsilon)_{n+1} - (\varepsilon_v)_{n+1}). \quad (3.24)$$

The different time steps are described as  $t_{n+1}$  for the time step following the current step  $t_n$ . To solve this equation and to get the information of the viscous part for the next time integration, the equation needs to be reformulated to

$$(\varepsilon_v)_{n+1} = \frac{\Delta t}{T_1 + \Delta t} (\varepsilon)_{n+1} - \frac{T_1}{T_1 + \Delta t} (\varepsilon_v)_n. \quad (3.25)$$

This equation shows, how the viscous strain is implemented in the material modeling approach. The Backward Euler method can be used as well for more than one Maxwell-Chain and for the 3-dim extension of the model.

The differential equation depicted in Eq. (3.22) describes the development of the stress with applied strain and a known stress at  $t = 0$ , or the development of strain with applied stress and known strain at  $t = 0$ . Using the harmonic Ansatz

$$\sigma(t) = \hat{\sigma} \exp(i\omega t) \Rightarrow \dot{\sigma}(t) = i\omega \hat{\sigma} \exp(i\omega t), \quad (3.26)$$

$$\varepsilon(t) = \hat{\varepsilon} \exp(i\omega t) \Rightarrow \dot{\varepsilon}(t) = i\omega \hat{\varepsilon} \exp(i\omega t), \quad (3.27)$$

for the differential equation, it results in

$$\begin{aligned}
i\omega \hat{\sigma} \exp(i\omega t) + \frac{E_1}{\eta} \hat{\sigma} \exp(i\omega t) &= (E_0 + E_1) i\omega \hat{\varepsilon} \exp(i\omega t) + \frac{E_0 E_1}{\eta} \hat{\varepsilon} \exp(i\omega t) \\
i\omega \hat{\sigma} + \frac{E_1}{\eta} \hat{\sigma} &= (E_0 + E_1) i\omega \hat{\varepsilon} + \frac{E_0 E_1}{\eta} \hat{\varepsilon} \\
\hat{\sigma} (i\omega \eta + E_1) &= \hat{\varepsilon} ((E_0 + E_1) i\omega \eta + E_0 E_1) \\
\hat{\sigma} (i\omega T_1 + 1) &= \hat{\varepsilon} ((E_0 + E_1) i\omega T_1 + E_0) \\
\frac{\hat{\sigma}}{\hat{\varepsilon}} &= \frac{(E_0 + E_1) i\omega T_1 + E_0}{i\omega T_1 + 1} \\
\frac{\hat{\sigma}}{\hat{\varepsilon}} &= \frac{E_0 (i\omega T_1 + 1) + E_1 i\omega T_1}{i\omega T_1 + 1} \\
\frac{\hat{\sigma}}{\hat{\varepsilon}} &= E_0 + \frac{E_1 i\omega T_1}{i\omega T_1 + 1} \\
\frac{\hat{\sigma}}{\hat{\varepsilon}} &= E_0 + \frac{E_1 i\omega T_1}{(i\omega T_1 + 1)} \cdot \frac{(i\omega T_1 - 1)}{(i\omega T_1 - 1)} \\
\frac{\hat{\sigma}}{\hat{\varepsilon}} &= E_0 + \frac{-E_1 \omega^2 T_1^2 - E_1 i\omega T_1}{(-\omega^2 T_1^2 - 1^2)} \\
\frac{\hat{\sigma}}{\hat{\varepsilon}} &= E_0 + \frac{E_1 \omega^2 T_1^2 + E_1 i\omega T_1}{\omega^2 T_1^2 + 1} \\
\frac{\hat{\sigma}}{\hat{\varepsilon}} &= E_0 + \frac{E_1 \omega^2 T_1^2}{\omega^2 T_1^2 + 1} + i \frac{E_1 \omega T_1}{\omega^2 T_1^2 + 1} \\
\frac{\hat{\sigma}}{\hat{\varepsilon}} &= E'(\omega) + i E''(\omega),
\end{aligned}$$

with  $E'$  as tensile storage modulus and  $E''$  as tensile loss modulus. These descriptions and their physical meanings are introduced a little later in this section.

Using the characteristic frequency  $\omega_m = \frac{1}{T_1} \iff T_1 = \frac{1}{\omega_m}$  will lead to a different kind of formulation which is sometimes used in literature like [68],

$$C(\omega)_{0-dim} = \frac{\hat{\sigma}}{\hat{\varepsilon}} = E_0 + \frac{E_1 \omega^2 T_1^2}{\omega^2 T_1^2 + 1} + i \frac{E_1 \omega T_1}{\omega^2 T_1^2 + 1} \quad (3.28)$$

$$\frac{\hat{\sigma}}{\hat{\varepsilon}} = E_0 + \frac{E_1 \omega^2 \frac{1}{\omega_m^2}}{\omega^2 \frac{1}{\omega_m^2} + 1} + \frac{E_1 i \omega \frac{1}{\omega_m}}{\omega^2 \frac{1}{\omega_m^2} + 1} \quad (3.29)$$

$$\frac{\hat{\sigma}}{\hat{\varepsilon}} = E_0 + \frac{E_1 \omega^2}{\omega^2 + \omega_m^2} + \frac{E_1 i \omega}{\omega^2 \frac{1}{\omega_m} + \omega_m} \quad (3.30)$$

$$\frac{\hat{\sigma}}{\hat{\varepsilon}} = E_0 + \frac{E_1 \omega^2}{\omega^2 + \omega_m^2} + \frac{E_1 i \omega \omega_m}{\omega^2 + \omega_m^2} \quad (3.31)$$

$$\frac{\hat{\sigma}}{\hat{\varepsilon}} = E_0 + \frac{E_1 \omega^2 + E_1 i \omega \omega_m}{\omega^2 + \omega_m^2}. \quad (3.32)$$

The proof that the given equation is the same as presented in [68], is given in Chapter A.

Considering a viscoelastic fluid, the difference to the before presented model is mainly to omit the parallel single spring in the model since a viscoelastic fluid does not have a basic stiffness. This assumption can also be applied on the forthcoming introduction of the next models. Within the different chapters of this thesis it is again stated if a viscoelastic solid or fluid is modeled.

### (2n+1)-parameter model

For more complex material behavior the basic Maxwell-Zener model is usually not sufficient. The reason lies in the number of Maxwell elements, the Maxwell-Zener model only has one. To describe a more complex material behavior, the fitting procedure of the material values shows a lack of flexibility, when only using one Maxwell element representing a single characteristic relaxation time. For a more detailed description, see section 3.3.2. With an extension in numbers of the Maxwell elements and with

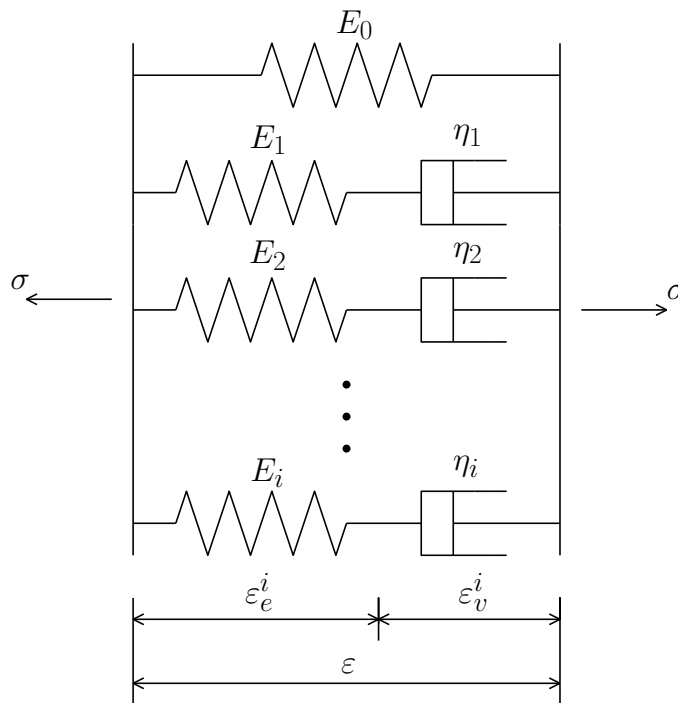


Figure 3.2: Extension of the Maxwell-Zener model, the (2n+1)-parameter model.

different properties for each Maxwell element, a more complex material behavior can be described. With each added Maxwell element, two more material parameters  $E_i$  und  $\eta_i$  are required. By summing up the non-equilibrium stresses in Figure 3.2 and by adding the single equilibrium stress, the overall stress of the extended Maxwell-Zener

model reads

$$\boldsymbol{\sigma} = \boldsymbol{\sigma}_{eq} + \sum_{i=1}^n \boldsymbol{\sigma}_{neq}^i \quad \forall \quad i = \{1, \dots, n\}. \quad (3.33)$$

Requirement for this equation is of course the description of the equilibrium stress and non-equilibrium stress as already introduced in the preceding part of this section. The equilibrium stress is defined by

$$\boldsymbol{\sigma}_{eq} = E_0 \boldsymbol{\varepsilon} \quad (3.34)$$

and the each single non-equilibrium stress  $\boldsymbol{\sigma}_{neq}^i$  is defined by

$$\boldsymbol{\sigma}_{neq}^i = E_i (\boldsymbol{\varepsilon} - \boldsymbol{\varepsilon}_v^i). \quad (3.35)$$

Since the before mentioned models are introduced in a 0-dim sense, the next section deals with an extension to 3-dim.

### 3-dim extension of the Maxwell-Zener model

The 3-dim extension of the Maxwell-Zener model is shown in Figure 3.3. As for the

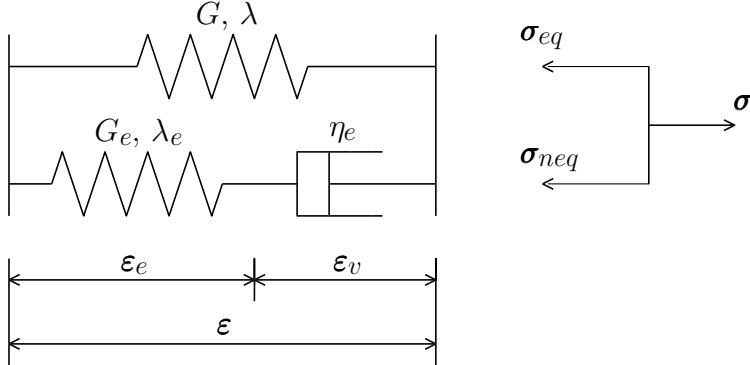


Figure 3.3: 3-dim extension of the Maxwell-Zener model.

0-dim case, the overall stress of the shown 0-dim model consists of an equilibrium part  $\boldsymbol{\sigma}_{eq}$  and a non-equilibrium part  $\boldsymbol{\sigma}_{neq}$ . Considering all the scalar factors in Figure 3.1, the 3-dim consideration leads to second-order tensors. Besides that, the properties of the spring element are now described by two material parameters, the shear modulus  $G$  and the Lamé parameter  $\lambda$ . Therefore, the equation for stress can be written as

$$\boldsymbol{\sigma} = \boldsymbol{\sigma}_{eq} + \boldsymbol{\sigma}_{neq} \quad (3.36)$$

$$\boldsymbol{\sigma} = 2G \boldsymbol{\varepsilon} + \lambda (\text{tr } \boldsymbol{\varepsilon}) \mathbf{I} + 2G_e \boldsymbol{\varepsilon}_e + \lambda_e (\text{tr } \boldsymbol{\varepsilon}_e) \mathbf{I}. \quad (3.37)$$

The function of free energy for the 3-dim model reads

$$\rho_0 \Psi = \rho_0 \Psi(\boldsymbol{\varepsilon}, \boldsymbol{\varepsilon}_e) = G \boldsymbol{\varepsilon} : \boldsymbol{\varepsilon} + \frac{1}{2} \lambda (\boldsymbol{\varepsilon} : \mathbf{I})^2 + G_e \boldsymbol{\varepsilon}_e : \boldsymbol{\varepsilon}_e + \frac{1}{2} \lambda_e (\boldsymbol{\varepsilon}_e : \mathbf{I})^2. \quad (3.38)$$

Furthermore, the Clausius-Duhem inequality is given as

$$\boldsymbol{\sigma} : \dot{\boldsymbol{\varepsilon}} - \rho_0 \dot{\Psi} \geq 0 \quad (3.39)$$

for isothermal processes. The material derivative of the function of free energy (3.38) reads

$$\rho_0 \dot{\Psi} = [2G \boldsymbol{\varepsilon} + \lambda (\text{tr } \boldsymbol{\varepsilon}) \mathbf{I}] : \dot{\boldsymbol{\varepsilon}} + [2G_e \boldsymbol{\varepsilon}_e + \lambda_e (\text{tr } \boldsymbol{\varepsilon}_e) \mathbf{I}] : \dot{\boldsymbol{\varepsilon}}_e. \quad (3.40)$$

Due to the connection of  $\boldsymbol{\varepsilon}_e = \boldsymbol{\varepsilon} - \boldsymbol{\varepsilon}_v$ , it is also possible to replace the time derivative  $\dot{\boldsymbol{\varepsilon}}_e = \dot{\boldsymbol{\varepsilon}} - \dot{\boldsymbol{\varepsilon}}_v$ . With this assumptions, the before mentioned equation leads to

$$\rho_0 \dot{\Psi} = [2G \boldsymbol{\varepsilon} + \lambda (\text{tr } \boldsymbol{\varepsilon}) \mathbf{I}] : \dot{\boldsymbol{\varepsilon}} + [2G_e \boldsymbol{\varepsilon}_e + \lambda_e (\text{tr } \boldsymbol{\varepsilon}_e) \mathbf{I}] : \dot{\boldsymbol{\varepsilon}} - [2G_e \boldsymbol{\varepsilon}_e + \lambda_e (\text{tr } \boldsymbol{\varepsilon}_e) \mathbf{I}] : \dot{\boldsymbol{\varepsilon}}_v, \quad (3.41)$$

where

$$\boldsymbol{\sigma}_{eq} = \frac{\partial \rho_0 \Psi}{\partial \boldsymbol{\varepsilon}} = 2G \boldsymbol{\varepsilon} + \lambda (\text{tr } \boldsymbol{\varepsilon}) \mathbf{I} \quad (3.42)$$

and

$$\boldsymbol{\sigma}_{neq} = \frac{\partial \rho_0 \Psi}{\partial \boldsymbol{\varepsilon}_v} = 2G_e \boldsymbol{\varepsilon}_e + \lambda_e (\text{tr } \boldsymbol{\varepsilon}_e) \mathbf{I}. \quad (3.43)$$

This gives the opportunity to write Eq. (3.41) in the form of

$$\rho_0 \dot{\Psi} = \boldsymbol{\sigma} : \dot{\boldsymbol{\varepsilon}} - \boldsymbol{\sigma}_{neq} : \dot{\boldsymbol{\varepsilon}}_v. \quad (3.44)$$

By taking this equation and inserting it into the Clausius-Duhem inequality, the outcome is an equation in the form of

$$\boldsymbol{\sigma} : \dot{\boldsymbol{\varepsilon}} - \boldsymbol{\sigma} : \dot{\boldsymbol{\varepsilon}} + \boldsymbol{\sigma}_{neq} : \dot{\boldsymbol{\varepsilon}}_v \geq 0 \iff \boldsymbol{\sigma}_{neq} : \dot{\boldsymbol{\varepsilon}}_v \geq 0. \quad (3.45)$$

This requirement needs to be fulfilled at any time and it is, if the tensors are coaxial. As previously stated for the 0-dim case,

$$\boldsymbol{\sigma}_{neq} = \eta_e \dot{\boldsymbol{\varepsilon}}_v \quad (3.46)$$

and therefore

$$\dot{\boldsymbol{\varepsilon}}_v = \frac{1}{\eta_e} [2G_e \boldsymbol{\varepsilon}_e + \lambda_e (\text{tr } \boldsymbol{\varepsilon}_e) \mathbf{I}]. \quad (3.47)$$

It is important to remark that the given material can be incompressible by nature. This means under the assumption of small deformations that  $\det \mathbf{F} = 1$ . An assumption of incompressibility means as well that  $\text{tr } \boldsymbol{\varepsilon} = 0$  and  $\text{tr } \boldsymbol{\varepsilon}_e = \text{tr } \boldsymbol{\varepsilon}_v = 0$ . Starting

with incompressibility, a volumetric-deviatoric split is introduced, exemplary shown for the equilibrium stress

$$\begin{aligned}
\boldsymbol{\sigma}_{eq} &= 2G \boldsymbol{\varepsilon} + \lambda (\text{tr } \boldsymbol{\varepsilon}) \mathbf{I} \\
&= 2G \boldsymbol{\varepsilon} + K (\text{tr } \boldsymbol{\varepsilon}) \mathbf{I} - \frac{2}{3} G (\text{tr } \boldsymbol{\varepsilon}) \mathbf{I} \\
&= 2G \boldsymbol{\varepsilon} + K (\text{tr } \boldsymbol{\varepsilon}) \mathbf{I} - \frac{2}{3} G n \boldsymbol{\varepsilon}^{\text{vol}} \\
&= 2G \boldsymbol{\varepsilon} + K (\text{tr } \boldsymbol{\varepsilon}) \mathbf{I} - \frac{2}{3} G n (\boldsymbol{\varepsilon} - \boldsymbol{\varepsilon}^{\text{dev}}) \\
&= K (\text{tr } \boldsymbol{\varepsilon}) \mathbf{I} + 2G \boldsymbol{\varepsilon}^{\text{dev}}.
\end{aligned} \tag{3.48}$$

It is to mention that the value  $n$  is a parameter depending on the dimension of the problem, which is here  $n = 3$ . For a better understanding of the deviation it is to add that the strain tensor  $\boldsymbol{\varepsilon}$  can be split in a volumetric and a deviatoric part

$$\boldsymbol{\varepsilon} = \boldsymbol{\varepsilon}^{\text{vol}} + \boldsymbol{\varepsilon}^{\text{dev}}. \tag{3.49}$$

The volumetric part is calculated via

$$\boldsymbol{\varepsilon}^{\text{vol}} = \frac{1}{n} (\text{tr } \boldsymbol{\varepsilon}) \mathbf{I}. \tag{3.50}$$

Time derivative of  $\boldsymbol{\sigma}$  reads

$$\dot{\boldsymbol{\sigma}} = 2G \dot{\boldsymbol{\varepsilon}}^{\text{dev}} + 2G_e \dot{\boldsymbol{\varepsilon}}_e^{\text{dev}} \tag{3.51}$$

$$= 2G \dot{\boldsymbol{\varepsilon}}^{\text{dev}} + 2G_e (\dot{\boldsymbol{\varepsilon}}^{\text{dev}} - \dot{\boldsymbol{\varepsilon}}_v^{\text{dev}}). \tag{3.52}$$

The evolution equation for the 3-dim case can be derived based on Eq. (3.46) as

$$\dot{\boldsymbol{\varepsilon}}_v = \frac{1}{\eta_e} \boldsymbol{\sigma}_{neq}^{\text{dev}} \tag{3.53}$$

$$= \frac{1}{\eta_e} (\boldsymbol{\sigma}_{neq} - \boldsymbol{\sigma}_{neq}^{\text{vol}}) \tag{3.54}$$

$$= \frac{1}{\eta_e} 2G_e [(\boldsymbol{\varepsilon} - \boldsymbol{\varepsilon}_v) - \frac{1}{3} \text{tr}(\boldsymbol{\varepsilon} - \boldsymbol{\varepsilon}_v) \mathbf{I}] \tag{3.55}$$

$$= \frac{1}{\eta_e} 2G_e (\boldsymbol{\varepsilon} - \boldsymbol{\varepsilon}_v) \tag{3.56}$$

$$= \frac{1}{\eta_e} \boldsymbol{\sigma}_{neq} \tag{3.57}$$

$$= \frac{1}{\eta_e} (\boldsymbol{\sigma} - 2G \boldsymbol{\varepsilon}). \tag{3.58}$$

For incompressible material behavior the bulk moduli  $K$  and  $K_e$ , of the single spring and the attached Maxwell-Chain, can be set to very high values ( $\gg G$ ).

The definition of the relaxation time reads

$$T = \frac{\eta_e}{G_e}. \tag{3.59}$$

On condition that  $\text{tr } \boldsymbol{\varepsilon}_e = 0$ , the evolution equation can be written in the following way

$$\dot{\boldsymbol{\varepsilon}}_v = \frac{2}{T} (\boldsymbol{\varepsilon}^{\text{dev}} - \boldsymbol{\varepsilon}_v^{\text{dev}}) = \frac{2}{T} (\boldsymbol{\varepsilon} - \boldsymbol{\varepsilon}_v). \quad (3.60)$$

Eq. (3.60) comprises the assumption that bulk viscosity is neglected. In combination with the stress-strain relationship, shown for the equilibrium stress  $\boldsymbol{\sigma}_{eq}$  in Eq. (3.48), the evolution equation builds the basis for the evaluation of viscoelastic material. As already introduced in one of the previous sections, the concept of internal variables needs to be used [50] and the evolution equation for the 3-dim case can be solved using the Backward Euler method.

Going back to the time derivative of  $\boldsymbol{\sigma}$  we use  $\dot{\boldsymbol{\varepsilon}}_v = \frac{1}{\eta_e} (\boldsymbol{\sigma} - 2G\boldsymbol{\varepsilon})$  for further steps and it follows

$$\dot{\boldsymbol{\sigma}} = 2G\dot{\boldsymbol{\varepsilon}}^{\text{dev}} + 2G_e(\dot{\boldsymbol{\varepsilon}}^{\text{dev}} - \dot{\boldsymbol{\varepsilon}}_v^{\text{dev}}) \quad (3.61)$$

$$\dot{\boldsymbol{\sigma}} = 2G\dot{\boldsymbol{\varepsilon}}^{\text{dev}} + 2G_e\dot{\boldsymbol{\varepsilon}}^{\text{dev}} - 2G_e\frac{\boldsymbol{\sigma}}{\eta_e} + \frac{4GG_e}{\eta_e}\boldsymbol{\varepsilon}^{\text{dev}} \quad (3.62)$$

$$\dot{\boldsymbol{\sigma}} + 2G_e\frac{\boldsymbol{\sigma}}{\eta_e} = 2(G + G_e)\dot{\boldsymbol{\varepsilon}}^{\text{dev}} + \frac{4GG_e}{\eta_e}\boldsymbol{\varepsilon}^{\text{dev}}. \quad (3.63)$$

As already done before in the 0-dim case, the harmonic Ansatz

$$\boldsymbol{\sigma}(t) = \hat{\boldsymbol{\sigma}} \exp(i\omega t) \Rightarrow \dot{\boldsymbol{\sigma}}(t) = i\omega \hat{\boldsymbol{\sigma}} \exp(i\omega t), \quad (3.64)$$

$$\boldsymbol{\varepsilon}(t) = \hat{\boldsymbol{\varepsilon}} \exp(i\omega t) \Rightarrow \dot{\boldsymbol{\varepsilon}}(t) = i\omega \hat{\boldsymbol{\varepsilon}} \exp(i\omega t), \quad (3.65)$$

is used for the differential equation as for the 0-dim case before. This leads in the 3-dim case to

$$i\omega \hat{\sigma} \exp(i\omega t) + \frac{2G_e}{\eta_e} \hat{\sigma} \exp(i\omega t) = 2(G + G_e) i\omega \hat{\varepsilon} \exp(i\omega t) + 4 \frac{GG_e}{\eta_e} \hat{\varepsilon} \exp(i\omega t) \quad (3.66)$$

$$i\omega \hat{\sigma} + \frac{2G_e}{\eta_e} \hat{\sigma} = 2(G + G_e) i\omega \hat{\varepsilon} + 4 \frac{GG_e}{\eta_e} \hat{\varepsilon} \quad (3.67)$$

$$\hat{\sigma} (i\omega \eta_e + 2G_e) = \hat{\varepsilon} (2(G + G_e) i\omega \eta_e + 4GG_e) \quad (3.68)$$

$$\hat{\sigma} (i\omega T_1 + 2) = \hat{\varepsilon} (2(G + G_e) i\omega T_1 + 4G) \quad (3.69)$$

$$\hat{\sigma} : \hat{\varepsilon}^{-1} = \frac{2(G + G_e) i\omega T_1 + 4G}{i\omega T_1 + 2} \quad (3.70)$$

$$\hat{\sigma} : \hat{\varepsilon}^{-1} = \frac{2G(i\omega T_1 + 2) + 2G_e i\omega T_1}{i\omega T_1 + 2} \quad (3.71)$$

$$\hat{\sigma} : \hat{\varepsilon}^{-1} = 2G + \frac{2G_e i\omega T_1}{i\omega T_1 + 2} \quad (3.72)$$

$$\hat{\sigma} : \hat{\varepsilon}^{-1} = 2G + \frac{2G_e i\omega T_1}{(i\omega T_1 + 2)} \cdot \frac{(i\omega T_1 - 2)}{(i\omega T_1 - 2)} \quad (3.73)$$

$$\hat{\sigma} : \hat{\varepsilon}^{-1} = 2G + \frac{-2G_e \omega^2 T_1^2 - 4G_e i\omega T_1}{(-\omega^2 T_1^2 - 2^2)} \quad (3.74)$$

$$\hat{\sigma} : \hat{\varepsilon}^{-1} = 2G + \frac{2G_e \omega^2 T_1^2 + 4G_e i\omega T_1}{\omega^2 T_1^2 + 4} \quad (3.75)$$

$$\hat{\sigma} : \hat{\varepsilon}^{-1} = 2G + \frac{2G_e \omega^2 T_1^2}{\omega^2 T_1^2 + 4} + i \frac{4G_e \omega T_1}{\omega^2 T_1^2 + 4} \quad (3.76)$$

$$\hat{\sigma} : \hat{\varepsilon}^{-1} = G'(\omega) + iG''(\omega), \quad (3.77)$$

with  $G'$  as shear storage modulus and  $G''$  as shear loss modulus. The translation with dependency of  $\omega_m = \frac{1}{T_1} \iff T_1 = \frac{1}{\omega_m}$ , which will again result in a different kind of formulation, is given as

$$\hat{\sigma} : \hat{\varepsilon}^{-1} = 2G + \frac{2G_e \omega^2 T_1^2}{\omega^2 T_1^2 + 4} + i \frac{4G_e \omega T_1}{\omega^2 T_1^2 + 4} \quad (3.78)$$

$$\hat{\sigma} : \hat{\varepsilon}^{-1} = 2G + \frac{2G_e \omega^2 \frac{1}{\omega_m^2}}{\omega^2 \frac{1}{\omega_m^2} + 4} + i \frac{4G_e \omega \frac{1}{\omega_m}}{\omega^2 \frac{1}{\omega_m^2} + 4} \quad (3.79)$$

$$\hat{\sigma} : \hat{\varepsilon}^{-1} = 2G + \frac{2G_e \omega^2}{\omega^2 + 4\omega_m^2} + \frac{4G_e i\omega}{\omega^2 \frac{1}{\omega_m} + 4\omega_m} \quad (3.80)$$

$$\hat{\sigma} : \hat{\varepsilon}^{-1} = 2G + \frac{2G_e \omega^2}{\omega^2 + 4\omega_m^2} + \frac{4G_e i\omega \omega_m}{\omega^2 + 4\omega_m^2} \quad (3.81)$$

$$C(\omega)_{3-dim} = \hat{\sigma} : \hat{\varepsilon}^{-1} = 2G + \frac{2G_e \omega^2 + 4G_e i\omega \omega_m}{\omega^2 + 4\omega_m^2}. \quad (3.82)$$

### 3-dim nonlinear viscoelastic modeling approach

This thesis also deals with a 3-dim formulation of nonlinear viscoelasticity, which is required when the theory is extended to moderate geometrical nonlinearities. The theoretical background for this specific part is described in section 6.3.2 where it is applied to experimental data and numerically investigated.

For the purpose of the nonlinear description at this point, we introduce, for each added Maxwell-Chain  $i = 1, 2, \dots, n$  to the above presented 3-dim Maxwell-Zener model, the multiplicative split of the deformation gradient into an elastic part  $\mathbf{F}_e^i$  and an inelastic or viscous part  $\mathbf{F}_v^i$ , see [45, 47, 48], and write

$$\mathbf{F} = \mathbf{F}_e^i \cdot \mathbf{F}_v^i. \quad (3.83)$$

With the already introduced right Cauchy-Green deformation tensor  $\mathbf{C}$  and the left Cauchy-Green deformation tensor  $\mathbf{B}$ , the viscous part of the right Cauchy-Green deformation tensor

$$\mathbf{C}_v^i = (\mathbf{F}_v^i)^T \cdot \mathbf{F}_v^i \quad (3.84)$$

and the elastic part of the left Cauchy-Green deformation tensor

$$\mathbf{B}_e^i = \mathbf{F}_e^i \cdot (\mathbf{F}_e^i)^T. \quad (3.85)$$

For more details please consider e.g. [25, 30]. The tensors  $\mathbf{C}_v^i, i = 1, 2, \dots, n$ , are interpreted as internal variables of the viscoelastic model described by an evolution equation, as already introduced for the linear modeling approach. Given an appropriate strain energy density function  $W$ , the Cauchy stress tensor is computed as

$$\mathbf{T} = 2 \frac{1}{J} \mathbf{B} \cdot \frac{\partial W}{\partial \mathbf{B}}. \quad (3.86)$$

For the scope of this work, the nonlinear approach which is described at this point is introduced to take the fact into account that within asphalt concrete locally large, i.e. finite strains, are expected. Therefore, the springs in the generalized Maxwell-Zener model can be modeled in terms of a Neo-Hookean strain energy density function with a volumetric-deviatoric split

$$W = W_{\text{eq}}(\mathbf{B}) + \sum_{i=1}^8 W_{\text{neq}}(\mathbf{B}_e^i) \quad (3.87)$$

$$= W_{\text{eq}}^{\text{vol}}(\mathbf{B}) + W_{\text{eq}}^{\text{dev}}(\mathbf{B}) + \sum_{i=1}^8 W_{\text{neq}}^{\text{dev},i}(\mathbf{B}_e^i) \quad (3.88)$$

$$= \frac{K}{2} (J - 1)^2 + \frac{G^0}{2} (I_1 - 3) + \sum_{i=1}^n \frac{G_e^i}{2} (I_1 - 3). \quad (3.89)$$

Hereby,  $G^0$  and  $G_e^i$  are the shear moduli of the springs and  $K$  is the bulk modulus. The volumetric contribution  $W_{\text{eq}}^{\text{vol}}(\mathbf{B})$  is introduced in the sense of a weak compressible

material, mainly for numerical reasons [30]. Moreover,  $I_1 = \lambda_1 + \lambda_2 + \lambda_3$  is the first strain invariant and  $J^2 = \lambda_1 \lambda_2 \lambda_3$ . With the Cauchy stress defined as

$$\mathbf{T} = \mathbf{T}_{\text{eq}}^{\text{vol}} + \mathbf{T}_{\text{eq}}^{\text{dev}} + \sum_{i=1}^8 \mathbf{T}_{\text{neq}}^{\text{dev},i} \quad (3.90)$$

$$= 2 \frac{1}{J} \left( \mathbf{B} \cdot \frac{\partial W_{\text{eq}}^{\text{vol}}}{\partial \mathbf{B}} + \mathbf{B} \cdot \frac{\partial W_{\text{eq}}^{\text{dev}}}{\partial \mathbf{B}} + \sum_{i=1}^8 \mathbf{B}_e^i \cdot \frac{\partial W_{\text{neq}}^{\text{dev},i}}{\partial \mathbf{B}_e^i} \right) \quad (3.91)$$

and the given strain energy density function, the constitutive equation reads

$$\mathbf{T} = K (J - 1) \mathbf{I} + \frac{1}{J} G^0 \mathbf{B}^0 + \sum_{i=1}^n \frac{1}{J} G_e^i \mathbf{B}_e^i. \quad (3.92)$$

Knowing that the Dynamic Shear Rheometer (DSR) experiments for the bituminous binding agent result in a viscoelastic fluid, the equilibrium part of the stress tensor ( $\mathbf{T}_{\text{eq}}$ ) has no deviatoric contribution ( $G^0 \approx 0$  MPa), and the constitutive equation in its final version states

$$\mathbf{T} = K (J - 1) \mathbf{I} + \sum_{i=1}^n \frac{1}{J} G_e^i \mathbf{B}_e^i. \quad (3.93)$$

Given this constitutive relation, it remains to define the viscoelastic equation system to be solved for the micro-scale. The evolution of the before mentioned internal variables is described in terms of an evolution equation of the form

$$\frac{d}{dt} (\mathbf{C}_v^i) = \dot{\mathbf{C}}_v^i = \frac{2}{JT_i} \left[ \mathbf{C} - \frac{1}{3} \text{tr} \left( \mathbf{C} \cdot (\mathbf{C}_v^i)^{-1} \right) \mathbf{C}_v^i \right]. \quad (3.94)$$

The solution of the evolution equation is geometrically nonlinear and can be solved using the already introduced Backward Euler method in time with

$$\left( \dot{\mathbf{C}}_v^i \right)_{n+1} = \frac{(\mathbf{C}_v^i)_{n+1} - (\mathbf{C}_v^i)_n}{\Delta t}. \quad (3.95)$$

### 3.3.1 Measurement methods

The behavior of viscoelastic materials can be determined by different methods. This includes the creep- or relaxation test and tests with dynamic loads on the material. During creep tests, the viscoelastic specimen is loaded with a predefined stress which is kept constant and the strain answer is measured over time. The resulting function is called creep function, which describes the delayed strain answer of the material. The relaxation- or stress relaxation test is the counterpart of the creep test. The specimen is stretched by a predefined value and kept in this position. The stretch is usually applied under simple tension- or shear conditions. The applied stretch results in a stress answer which relaxes over time, this result is called the relaxation function. In contrast to these two measurement methods, the stimulation in a dynamic test can

be applied with a sinusoidal strain or stress load. Using a time dependent strain with such a sinusoidal form

$$\tau(t) = \tau_0 \sin(\omega t), \quad (3.96)$$

for an ideal elastic solid

$$\tau(t) = G\gamma(t), \quad (3.97)$$

results in a stress answer

$$\tau(t) = \tau_0 \sin(\omega t), \quad (3.98)$$

which is sinusoidal as well. This means that under the condition of an ideal elastic solid, strain load and stress answer happen without a fraction of delay. This means the phase angle  $\delta$  between strain and stress is equal to 0. It should be mentioned that isotropic material behavior in 0-dim is provided. For more dimensional considerations this behavior applies correspondingly. In contrast to the ideal elastic solid, the stress for an ideal viscous fluid reads

$$\tau(t) = \eta \dot{\gamma}(t), \quad (3.99)$$

with the corresponding stress answer

$$\tau(t) = \omega \tau_0 \cos(\omega t). \quad (3.100)$$

Therefore, the stress answer is towards the time dependent strain shifted by  $\delta = \frac{\pi}{2}$ . The two previously shown examples for the ideal elastic solid and the ideal viscous fluid are extreme examples with regard to the phase angle  $\delta$ . For any other arbitrary viscoelastic behavior, the phase angle is placed somewhere in between these two extreme values. The general stress answer reads

$$\tau(t) = \tau_0 \sin(\omega t + \delta) \quad (3.101)$$

and this results in

$$\tau(t) = \tau_0 [\sin(\omega t) \cos\delta + \cos(\omega t) \sin\delta]. \quad (3.102)$$

With another change in this formulation, it is immediately displayed that the stress answer consists of an elastic part, which oscillates in phase with the stimulation and a viscous part, which oscillates shifted in phase by  $\delta = \frac{\pi}{2}$ ,

$$\tau(t) = \tau_0 \sin(\omega t) \cos\delta + \tau_0 \cos(\omega t) \sin\delta. \quad (3.103)$$

This fact enables to introduce two moduli. One modulus for the part which oscillates in phase and another modulus for the part which oscillates phase shifted. The stress-strain relation results in

$$\tau(t) = \gamma_0 G' \sin(\omega t) + \gamma_0 G'' \cos(\omega t), \quad (3.104)$$

with shear storage modulus

$$G' = \frac{\tau_0}{\gamma_0} \cos\delta \quad (3.105)$$

and shear loss modulus

$$G'' = \frac{\tau_0}{\gamma_0} \sin\delta. \quad (3.106)$$

If the stress-strain relation is in phase, the supplied energy is stored as potential energy and remains available. The viscous part is described by the loss modulus, where the supplied energy is dissipated as heat. Therefore, the loss factor  $\tan\delta$  describes the ratio between stored and dissipated energy and is calculated by the quotient of loss- and storage modulus

$$\tan\delta = \frac{G''}{G'}. \quad (3.107)$$

The here presented method is especially important when it comes to the experimental determination of viscoelastic material behavior and the creation of a rheological model based on the gained data. Corresponding to the shear storage- and loss modulus, the tensile moduli,  $E'$  and  $E''$  can be derived in a similar manner.

### 3.3.2 Fitting

The development of a rheological model for the bituminous binding agent is based on experimental data and later implemented in a Finite Element formulation. As already mentioned in Chapter 3.1, throughout this thesis the used rheological model for the bituminous binding agent is the 3-dim extension of the Maxwell-Zener model. With DSR testing an identification of the complex modulus  $G^*$  and the phase angle  $\delta$  is possible. The formulation for the shear storage- and loss modulus is derived a few pages ago and read

$$G' = 2G_0 + \sum_{i=1}^n \frac{2G_i\omega^2 T_i^2}{\omega^2 T_i^2 + 4}, \quad (3.108)$$

$$G'' = \sum_{i=1}^n \frac{4G_i\omega T_i}{\omega^2 T_i^2 + 4}. \quad (3.109)$$

In these equations  $\omega$  is the frequency,  $T_i$  the different relaxation times and  $G_i$  the different elasticities or more specific the different shear moduli. The dynamic shear modulus reads

$$|G^*| = \sqrt{G'^2 + G''^2} \quad (3.110)$$

and enables a fitting procedure for the experimental data. Figure 3.4 a) illustrates the result for one Maxwell-Chain without separate elasticity  $G_0$  which are in value characterized as

$$G_1 = 170 \text{ MPa} \quad (3.111)$$

and

$$T_1 = 0.001 \text{ s} \Rightarrow f_m = \frac{1}{T_1} = 1000 \text{ Hz.} \quad (3.112)$$

With this pinpointing procedure, the problem with the fitting process is visualized

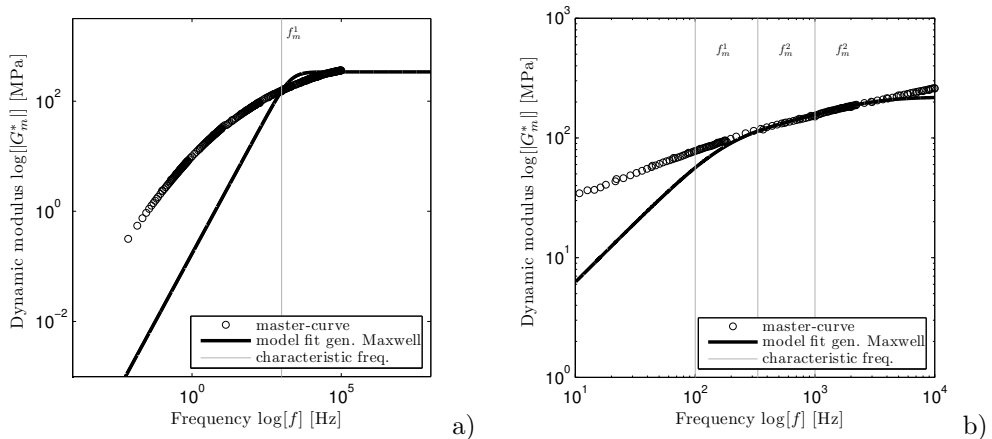


Figure 3.4: Pure 20/30 penetration grade bituminous binding agent. a) Master-curve pinpointed with one Maxwell-Chain. b) Master-curve with three Maxwell-Chains to underline the fitting aspects.

very well. Since the relaxation itself follows exponential behavior  $\Rightarrow e^{-\frac{t}{T}}$  there is no possibility to fit a single Maxwell-Chain to another slope than the one that follows  $e^{-\frac{t}{T}}$ . In the following, a short list of characteristic values of percentages for the relaxation of a specific elasticity  $G$  in the time domain:

- $t = 0.69 T \Rightarrow 0.500 G$
- $t = 1.00 T \Rightarrow \frac{1}{e} \Rightarrow 0.368 G$
- $t = 2.00 T \Rightarrow 0.135 G$
- $t = 3.00 T \Rightarrow 0.050 G$

By using more than one Maxwell-Chain it is possible to fit the model to another slope. Figure 3.4 b) shows an example for three different Maxwell-Chains with different characteristic frequencies. It is clear that with increasing amount of Maxwell-Chains the quality of the fit becomes more and more exact. The downside of an increasing number of Maxwell-Chains is simply the computational effort when it comes to solving all the equations that come with each additional Maxwell-Chain.

### 3.4 Numerical realization

In this section, the focus lies on the numerical realization of the introduced differential equations within the material modeling part of this thesis. Because of the strong

formulation of these equations the use of numerical methods for an approximated solution of the governing field equations is inevitable, since most of the equations can not be solved analytically. Within this thesis the Finite Element Method (FEM) is used. The weak form of the balance equation is described here. The initial boundary value problem, which is discussed later in this section, is present in the strong form. This means that the balance equation has to be fulfilled in each material point of the body  $\mathcal{B}$ . Within the weak formulation, this fulfillment is only required in an integral sense. First, bearing in mind the local form of the balance of momentum

$$\rho \ddot{\mathbf{x}} = \operatorname{div} \mathbf{T} + \rho \mathbf{b} \quad \forall \quad \mathbf{x} \in \mathcal{B}, \quad (3.113)$$

as already introduced in section 2.2.

### Initial boundary value problem

The quasi-static form of the balance of momentum reads

$$-\operatorname{div} \mathbf{T} = \rho \mathbf{b} \quad (3.114)$$

and can be supplemented with two different kinds of boundary conditions. On the one hand side these are stress driven boundary conditions (BCs), also called Neumann BCs and on the other side displacement driven boundary conditions, also called Dirichlet BCs. Figure 3.5 depicts the different kind of boundary conditions on a body  $\mathcal{B}$ . All boundary conditions are located on the outer surface  $\partial\mathcal{B}$  of the body. Thus, the relations

$$\bar{\mathbf{t}} = \mathbf{T} \cdot \mathbf{n} \quad \text{on} \quad \Gamma_N \quad (3.115)$$

and

$$\bar{\mathbf{u}} = \mathbf{u} \quad \text{on} \quad \Gamma_D, \quad (3.116)$$

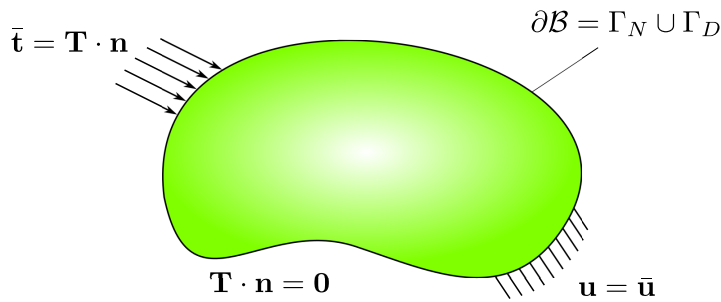
are valid, whereby both shown areas form the whole outer surface of the body.

$$\partial\mathcal{B} = \Gamma_N \cup \Gamma_D \quad \text{with} \quad \Gamma_N \cap \Gamma_D = \{\}. \quad (3.117)$$

### Weak form of the balance equation

For the derivation of the weak form of the balance equation, see Eq. (3.113), the strong form is multiplied with a test function  $\delta\mathbf{u}$  in a scalar way and integrated over the whole body  $\mathcal{B}$ . It is to mention that within this thesis, body forces and inertial forces are neglected. This reduces the balance of momentum to

$$\operatorname{div} \mathbf{T} = \mathbf{0}. \quad (3.118)$$

Figure 3.5: Possible boundary conditions of body  $\mathcal{B}$ .

With multiplication of the before mentioned test function  $\delta \mathbf{u}$  the integral over the balance of momentum reads

$$\int_{\mathbf{B}} \delta \mathbf{u} \cdot \operatorname{div} \mathbf{T} \, dv = 0. \quad (3.119)$$

For further steps and conversions of this integral the following relations are introduced

$$\operatorname{div} (\mathbf{a} \cdot \mathbf{A}) = (a_i A_{ij})_{,j} (\mathbf{e}_i \cdot \mathbf{e}_j) = (a_{i,j} A_{ij} + a_i A_{ij,j}) (\mathbf{e}_i \cdot \mathbf{e}_j), \quad (3.120)$$

$$\operatorname{div} (\mathbf{a} \cdot \mathbf{A}) = \operatorname{grad} \mathbf{a} : \mathbf{A} + \underline{\mathbf{a} \cdot \operatorname{div} \mathbf{A}}. \quad (3.121)$$

With these relations and with special regard to the underlined part, Eq. (3.119) now reads

$$\int_{\mathbf{B}} \operatorname{div} (\delta \mathbf{u} \cdot \mathbf{T}) \, dv - \int_{\mathbf{B}} \operatorname{grad} \delta \mathbf{u} : \mathbf{T} \, dv = 0. \quad (3.122)$$

With the divergence theorem or Gauss's theorem

$$\int_{\mathbf{B}} \operatorname{div} (\mathbf{A}) \, dv = \int_{\partial \mathbf{B}} \mathbf{A} \cdot \mathbf{n} \, da, \quad (3.123)$$

the equation is converted to

$$\int_{\mathbf{B}} \operatorname{grad} \delta \mathbf{u} : \mathbf{T} \, dv = \int_{\partial \mathbf{B}} \delta \mathbf{u} \cdot \underbrace{\mathbf{T} \cdot \mathbf{n}}_{\mathbf{t}} \, da. \quad (3.124)$$

Eq. (3.124) shows the weak formulation of the local balance of momentum. The left side of the equation needs to be fulfilled within the considered body  $\mathcal{B}$  in a weakly manner. The right side of the equation describes the Neumann boundary condition on the surface  $\partial \mathcal{B}$  of the body  $\mathcal{B}$ . The right side of the equation is not considered if the boundary conditions are applied using a Finite Element software. This leads to the final statement that with the presented constitutive material models in the previous sections and a discretization in space, the weak form of the balance of momentum, can be solved using for example a local Newton-Raphson algorithm.



## Chapter 4

# Extended master-curve concept for bitumen-filler mastics

*This chapter focuses on bitumen-filler mastics with regard to general master-curve relations from William, Landel, and Ferry [14] and an extension of this concept with regard to filler concentration. Based on experimental data for thermo-rheologically simple bitumen and bitumen-filler mastics a mathematical procedure is described to define a function which serves as a shift function enriching the time-temperature superposition principle by the content of filler particles. The viscoelastic experimental data is gathered with a Dynamic Shear Rheometer (DSR) for a wide frequency and temperature range. Further analyses such as He/Ne-Laser-Diffraction and Rigdens voids test support the description of the used limestone dust filler. The derived relation is tested to describe the rheological behavior of the viscoelastic material for the elastic and viscous limit, which means for very high and low frequencies. Furthermore, we compare the rheological behavior with classical formulas taken from literature. With all made assumptions and considering the experimental basis, the created function shows a good agreement even for the limit cases at high and low frequencies.*

### 4.1 Introduction

Mastics are used in almost all asphalt concretes and their effective properties highly influence the mechanical behavior of the whole composite structure. In literature, many different approaches to analyze mastics can be found, for example, with respect to the long-time response such as damage [13] and aging [64] or with respect to the rheology such as effective viscosity [26]. The main purpose for the admixed filler is the stiffening effect for the bitumen-filler mastic [42,77]. In literature, many investigations

show a dependency between physical properties and chemical composition of the filler with the effective mechanical properties and rheological behavior of the bitumen-filler mastic [27, 33, 35, 86]. In detail, investigations show the effect of filler type, grain size distribution and shape of the particles on the effective properties of bitumen-filler mastics [41]. Mastics are generally considered to be suspensions, where the mineral aggregates are suspended in the bituminous binding agent [12]. From a rheological point of view, suspensions can be divided into dilute suspensions and concentrated suspensions, depending on the volume fractions of the filler and the bituminous binding agent [10]. Comparing the two limit types for suspension, we can state that the mechanical behavior on the small scale is strongly diverging [78, 88]. Considering a dilute suspension, where the the mineral filler content is rather low, the interaction forces between mineral particles are practically not existent, because the distance between two neighboring particles is too large. The interaction forces can be formulated as soft-hard-soft, which corresponds to an interaction only between the soft bitumen and the hard particle phase. Considering a concentrated suspension, where the distance between neighboring particles gets closer or even vanishes, a permanent interaction between particles can occur. This phenomena can lead to permanent hard-hard interaction and finalize in a jammed state. In this chapter all investigations are carried out for dilute suspension, as the applied Rigden voids test [65] shows. Further investigations such as the characterization of the linear thermo-viscoelastic behavior of different bituminous mixtures and analyzing stiffness and amount of dissipated energy [63] are fields of ongoing research. Furthermore, experimental testing and characterization of different bituminous binders, also polymer-modified bituminous binders, are investigated in literature with regard to the influence of mineral fillers on the effective rheological response [5].

In this chapter, the well-established master-curve concept, see for example [14], is enriched by an additional degree, namely the filler concentration for the special case of bitumen-filler mastics. To the authors' best knowledge, such an extension is not available in literature so far. The proposed concept is applied to a broad basis of experimental Dynamic Shear Rheometer (DSR) data and the extension is conducted on the one hand in terms of the filler concentration inside the mastic and on the other hand in dependency of frequency. The motivation for this procedure is based on the observation that the experimental data shows self similar master-curves. For a certain concentration range we evaluate that dependency and extend the master-curve concept with respect to filler concentrations. The chapter itself is organized as follows: In section 4.2, the classical WLF relation (William, Landel, and Ferry) [14] is applied at six different temperatures and to five different filler concentrations. In section 4.3, the proposed approach for the master-curve concept with respect to the filler concentrations is presented.

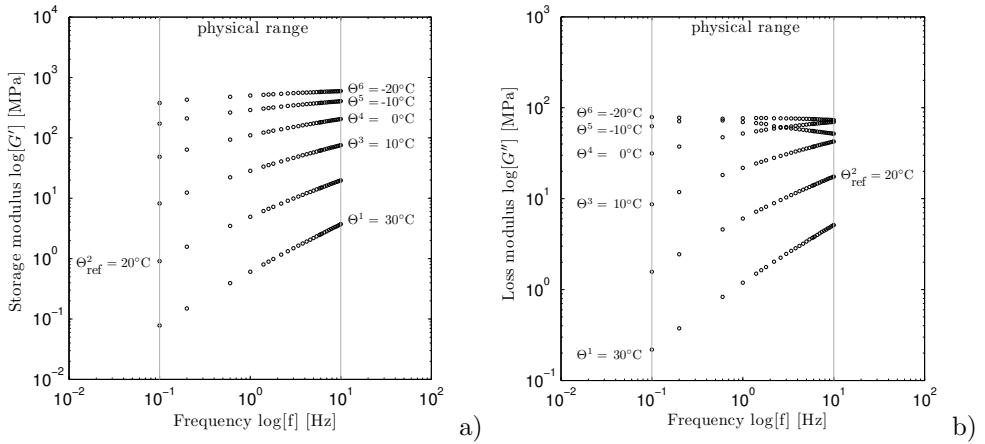


Figure 4.1: a) Storage modulus  $G'$  and b) loss modulus  $G''$  for pure 20/30 penetration grade bituminous binder for six different temperatures in a frequency range  $0.1 \text{ Hz} \leq f \leq 10 \text{ Hz}$ .

## 4.2 Material and methods

The bituminous binder under investigation in this chapter is a 20/30 penetration grade bituminous binder. The rheological behavior of the bituminous binder is determined by a DSR testing device (Anton Paar Physica MCR 101) at various frequencies and temperatures. A plate-plate configuration with plate radius  $r=8 \text{ mm}$  is used. Rheological investigations take place for six different temperatures  $\theta$  under iso-thermal conditions. Shear oscillations in a predefined frequency range from  $0.1 \text{ Hz} \leq f = \omega/(2\pi) \leq 10 \text{ Hz}$  are performed. The temperature range is set to  $-20^\circ\text{C} \leq \theta \leq 30^\circ\text{C}$  in intervals of  $10^\circ\text{C}$ . The DSR experiments enable us to determine the viscoelastic properties in form of the complex shear modulus  $G^*(\omega)$  and its phase angle  $\delta(\omega)$ , cf. [51]. The definition of the complex modulus reads  $G^* = G' + iG''$  with loss factor  $\tan \delta = G''/G'$ . Hereby  $G'$  represents the storage modulus and  $G''$  the loss modulus, respectively. The storage modulus  $G' = (\tau_0/\gamma_0) \cos \delta$  is an indicator for the stored energy which means it corresponds to the elastic part of the deformation. The loss modulus  $G'' = (\tau_0/\gamma_0) \sin \delta$  on the other hand is an indicator for the viscous energy contribution which is dissipated as heat. In both definitions,  $\tau_0$  is the shear stress amplitude,  $\gamma_0$  the corresponding shear strain amplitude. The phase angle  $\delta$  represents the phase lag between the occurring stress and strain and defines the nature of the investigated material, namely elastic ( $\delta = \pi/2$ ), purely viscous ( $\delta = 0$ ) or viscoelastic ( $0 < \delta < \pi/2$ ). At this point we also want to introduce the complex viscosity  $\eta^* = G^*/(2\pi f)$  with its magnitude  $|\eta^*|$  as the dynamic viscosity and the viscosity for the viscous fluid limit as  $\eta' = G''/(2\pi f)$  for  $f \rightarrow 0$ . Furthermore, we introduce the dynamic shear modulus  $|G^*|$ . The DSR measurements are shown in Figure 4.1 in terms of the storage  $G'$  and the loss  $G''$  modulus. In various investigations, pure bituminous

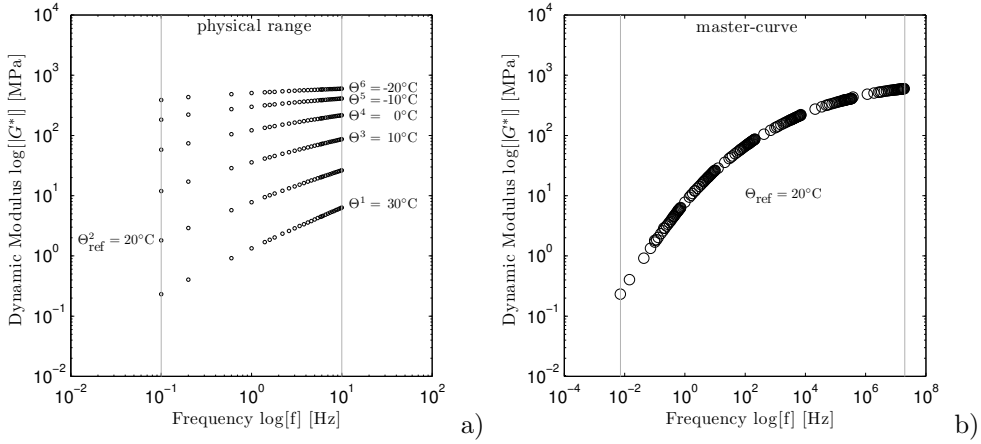


Figure 4.2: a) Dynamic modulus  $|G^*|$  for pure 20/30 penetration grade bituminous binder and b) the resulting master-curve.

binders have been identified as thermo-rheologically simple materials, see [8,94] and references therein. Based on these findings we apply the time-temperature superposition principle. For the generation of the master-curve in the frequency domain we evaluated the experimental results in form of the dynamic shear modulus  $|G^*|$ , cf. Figure 4.2, to consider the influences of both moduli  $G'$  and  $G''$ . In a second step, the pure 20/30 penetration grade bituminous binder is now investigated with a varying amount of mineral aggregates. Figure 4.3 shows the granulometric curve of the filler in the unit of the mass fraction, here abbreviated as M.-%, which is typical for the road building industry. The investigated filler is a limestone dust. The granulometric curve is based on a He/Ne-Laser-Diffraction (HELOS (H3020) equipped with a SUCCELL wet disperser). We introduce the individual phases  $\varphi^b$  as the bituminous binding agent and  $\varphi^p$  as the mineral filler and define the volume fractions as  $n^\alpha = dv^\alpha/dv$  with  $\alpha = \{b, p\}$  and  $n^b + n^p = 1$ , the volume element of the mixture  $dv$  and the volume element  $dv^\alpha$  occupied by phase  $\varphi^\alpha$ . Accordingly, we introduce the mass fraction  $w^\alpha = dm^\alpha/dm$  with the composite density  $\rho = \rho^b + \rho^p = dm/dv = dm^b/dv + dm^p/dv$  and the partial density  $\rho^\alpha = n^\alpha \rho^{\alpha R} = dm^\alpha/dv$ . Compare [75] for more information. For the investigated bitumen-filler mastic, the effective true densities are given as  $\rho^{bR} = dm^b/dv^b = 1.02 \text{ [g/cm}^3\text{]}$  and  $\rho^{pR} = dm^p/dv^p = 2.67 \text{ [g/cm}^3\text{]}$ , respectively. Since the composition of the mixture is controlled during the production process in terms of the mass fraction  $w^\alpha$ , we derive the volume fractions  $n^p$  of the filler

$$\frac{1}{n^p} = \left( 1 + \frac{\rho^{pR}}{w^p} \frac{w^b}{\rho^{bR}} \right). \quad (4.1)$$

This equation leads to Table 4.1, where the pure bituminous binder and four different mass fractions  $w^p$  and the corresponding volume fractions  $n^p$  are listed. Experimental data from DSR testing for  $w^p > 0.0$  are gathered in the same temperature and

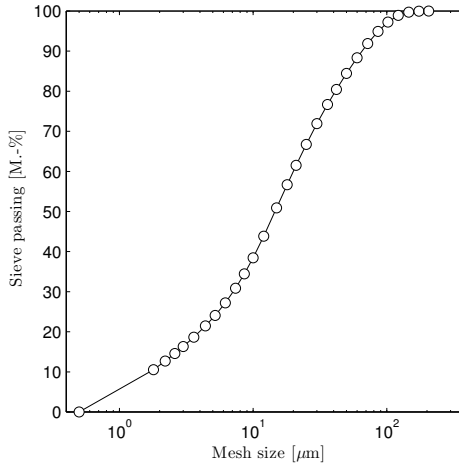


Figure 4.3: Granulometric curve of the filler.

Table 4.1: Mass fraction  $w^p$  and volume fraction  $n^p$  of the admixed filler.

$w^p$	0.00	0.20	0.36	0.50	0.65
$n^p$	0.00	0.09	0.18	0.28	0.41

frequency ranges as for the pure bituminous binder. The mastics (pure bituminous binder plus filler) are considered to be thermo-rheologically simple materials as well [2] and the master-curve concept is applied in the same manner as before. Figure 4.4 a) and b) shows the five different master-curves with respect to the dynamic modulus  $|G^*|$ , one for each filler content  $w^p$  and the respective dynamic viscosity  $|\eta^*|$ . To analyze the shift factors  $\alpha_\theta$  for each master-curve, the WLF relation [14]

$$\log[\alpha_\theta] = -\frac{c_1(\theta - \theta_{ref})}{c_2 + \theta - \theta_{ref}} \quad (4.2)$$

is applied to the data and illustrated in Figure 4.5.

### 4.3 Results and Discussion

To extend the approach of a shift factor in terms of temperature (WLF), the next step includes the dependency of the master-curves from the actual filler mass fraction  $w^p$ . To analyze the dependency of the master-curves with respect to the pure 20/30 penetration grade bituminous binder, we apply a linear interpolation to the master-curves from the dynamic shear modulus in a frequency range from  $f = 10^{-2}$  to  $f = 10^6$  Hz. This step is necessary to provide equidistant sampling points for each master-curve.

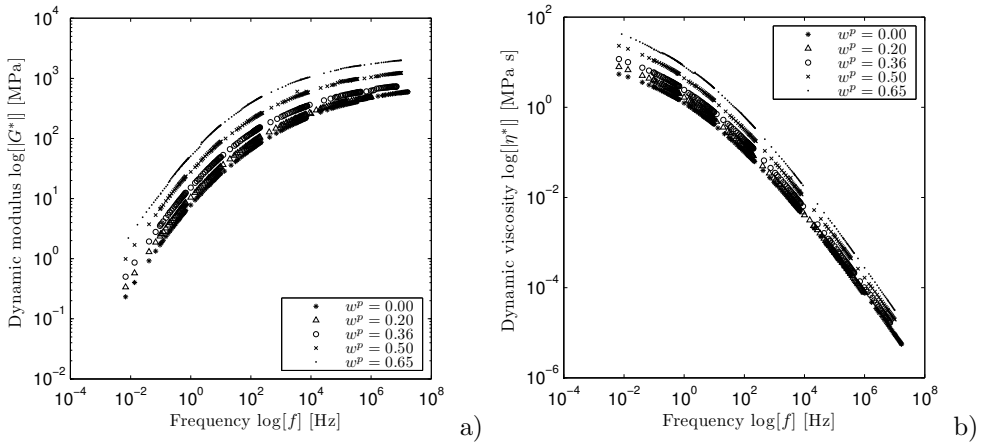


Figure 4.4: a) Master-curves of the dynamic modulus  $|G^*|$  and b) of the dynamic viscosity  $|\eta^*|$  for five different filler mass fractions  $w^p$ .

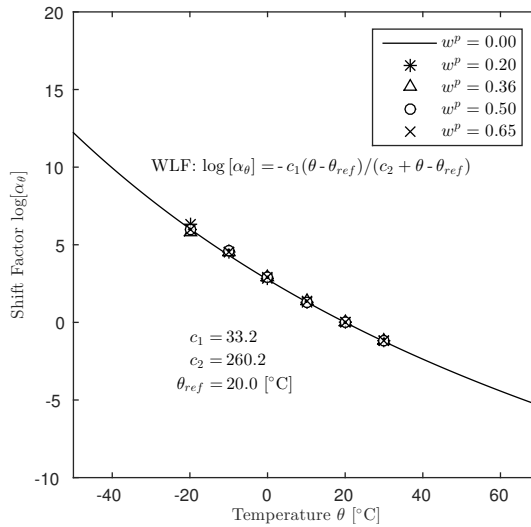


Figure 4.5: WLF function on the basis of six different temperatures  $\theta$  and five different filler mass fractions  $w^p$ .

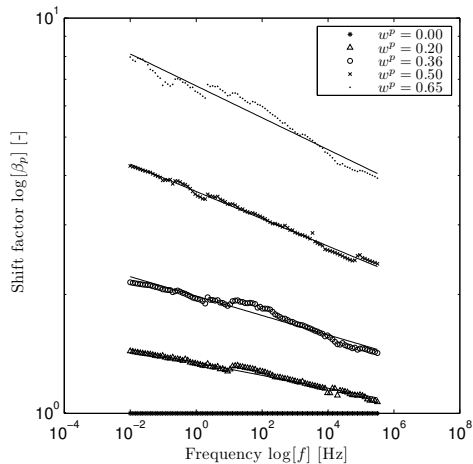


Figure 4.6: Shift factors  $\beta_p$  in a double-logarithmic representation for the five different filler mass fractions  $w^p$  with fitted linear regression functions for data set.

Considering the pure bituminous binder as the basis for this shift procedure, the shift of the self similar curves leads to the results, which are presented in Figure 4.6 in a double-logarithmic representation. We consider  $w^p = 0.65$  as the upper limit for this approach, since this already corresponds to a volume fraction of  $n^p = 0.41$ , see Table 4.1. Since the mixture tends to lose its properties as a suspension, the DSR testing is limited to a specific amount of mineral filler particles. A volume fraction  $n^p = 0.41$  is already close to that limit and, therefore, no higher volume fractions are considered. To underline this assumption by considering a maximum filler volume fraction in terms of dense packing, the present limestone dust is analyzed by performing the Rigden voids test [65]. The closest packing for the analyzed limestone dust within the Rigden voids test results in  $n_{\max}^p = 0.69$ . Comparing our determined maximum  $n^p = 0.41$  with the Rigden maximum  $n_{\max}^p = 0.69$ , we can state that our experimental data is far enough away from a possible jamming point and the derived data is not influenced by possible limitations of the experimental setup. Figure 4.6 shows the shift factor  $\beta_p$  with respect to frequency  $f$  and filler mass fractions  $w^p$ . The shift factor decreases with increasing frequency. This is due to the influence of the solid-like state at high frequencies or low temperatures, respectively. The influence of the filler particles decreases if the mastic tends to be solid-like. Since the shift factors in Figure 4.6 can be considered as linear functions, we use the linkage of a function  $F(x)$  in the logarithmic space  $\log F(x) = m \log x + n$ , with the non-logarithmic equivalent  $F(x) = x^m 10^n$ . The linear function is defined with the slope  $m$  and the intercept  $n$  in the double-logarithmic representation. Using the alteration of  $m$  and  $n$  in dependency of  $w^p$ , an overall shift function can be generated. For this reason, Figure 4.7 a) and b) shows the fitted functions for  $m$  and  $n$ . Allowing for  $0 \leq w^p \leq 0.65$ , we identify by polynomial fitting a linear function for  $m$  reads  $m = q_1 w^p$  with  $q_1 = -0.06591$  and a

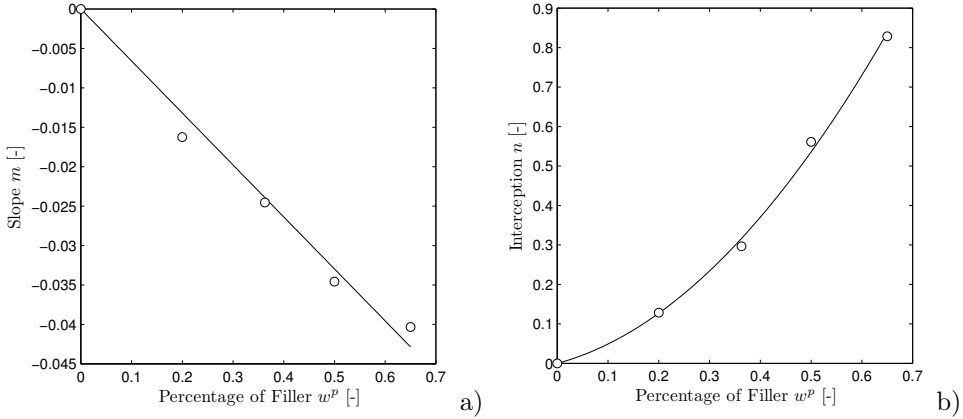


Figure 4.7: a) Linear function for slope  $m$  and quadratic function for intercept  $n$ .

quadratic function for  $n$  with  $n = q_2 (w^p)^2 + q_3 w^p$  with  $q_2 = 1.452$  and  $q_3 = 0.3453$ . These two functions are part of the overall function for the shift factor  $\beta_p = f^m 10^n$ , which is dependent on  $w^p$  and  $f$  and reads

$$\beta_p = f^{(q_1 w^p)} 10^{(q_2 (w^p)^2 + q_3 w^p)}. \quad (4.3)$$

The determined function for  $\beta_p$  and the experimental data is shown in Figure 4.8. Despite the fact that the shift factor  $\beta_p$  is based on a function with only three fitting parameters, it is possible to match the complex behavior of the experimental data in a very good accordance. With the function for  $\beta_p$  at hand, further investigations are possible. Considering  $f = 10^6$  Hz as the upper frequency limit of the master-curve and therefore an approximation for the elastic limit (at  $f \rightarrow \infty$ ) of our viscoelastic composite, an interesting field is the comparison of the underlying stiffness with classical bounds and mixing laws for effective elastic media. Figure 4.9 shows the storage modulus  $G'$  for the elastic limit ( $f = 10^6$  Hz) in comparison with the classical Hashin-Shtrikman (HS) bounds [24] for a maximum volume fraction  $n^p = 0.41$ . The HS bounds for the shear moduli take the form

$$G^{\text{HS}\pm} = G^b + \frac{n^p}{\frac{1}{(G^p - G^b)} + \frac{2 n^b (K^b + 2 G^b)}{5 G^b (K^b + \frac{4}{3} G^b)}}, \quad (4.4)$$

where the bulk modulus  $K^p = 56.2$  GPa and the shear modulus  $G^p = 32.0$  GPa of the particles are taken from literature [23].  $G^b = 0.4$  GPa as a starting point for the bituminous binder is taken from the experimental data and  $K^b = 20.0$  GPa is given due to the incompressibility of the bituminous binder. Upper and lower bounds are defined by interchanging the specific material parameters. Considering the displayed style, the formula defines the lower bound. Even though the function leads to a lower storage modulus for low volume fractions  $n^p$  of the particles as the lower HS bound, the defined function leads to a steady solution for the elastic limit. The tendency

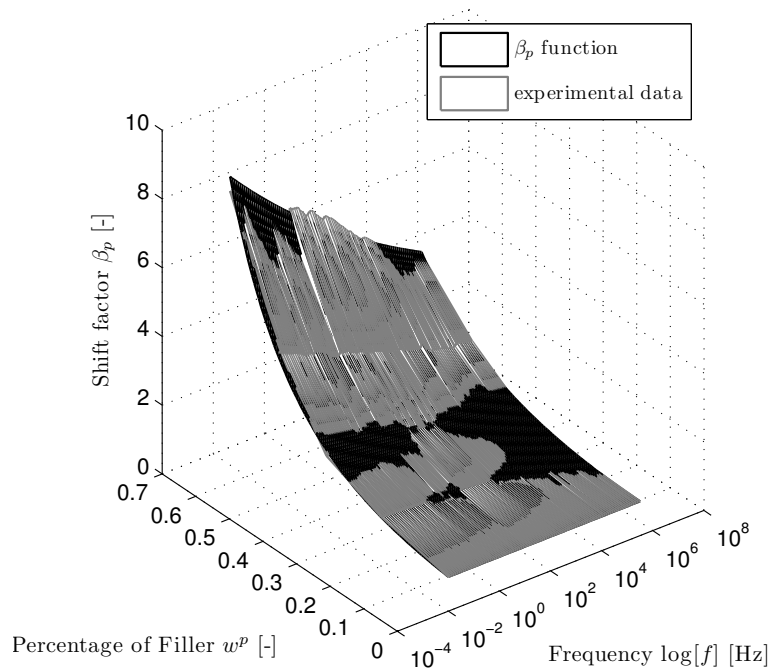


Figure 4.8: 3-dim view of the function for  $\beta_p$  and the corresponding experimental data.

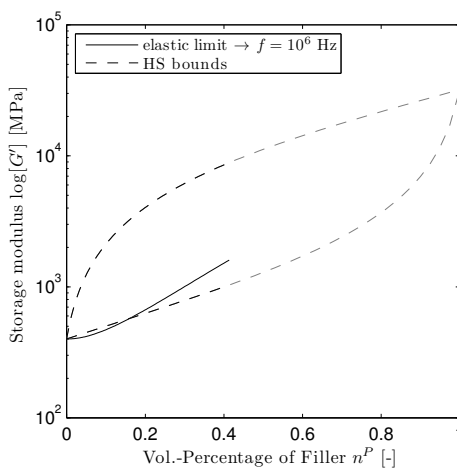


Figure 4.9: Storage modulus  $G'$  for the elastic limit ( $f = 10^6$  Hz) in comparison with lower and upper HS bounds.

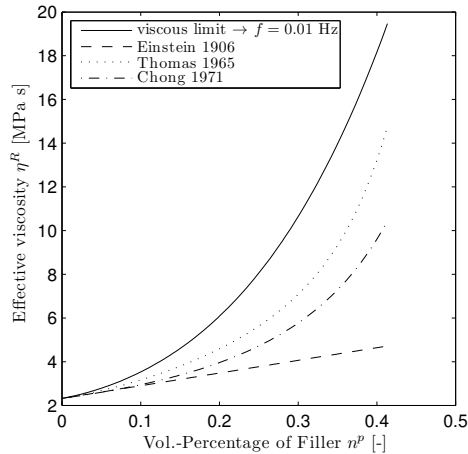


Figure 4.10: Effective viscosity  $\eta^R$  for the viscous fluid limit ( $f = 10^{-2}$  Hz) in comparison with different formulas taken from relevant literature.

to the lower HS bound is due to the fact that the supporting phase is of soft nature and not surprising. Furthermore, a strong assumption is the elastic limit for  $f = 10^6$  Hz, since the plateau region for this frequency is not yet reached, cf. Figure 4.4 a). Further remarks for the error at low volume fractions  $n^p$  are experimental deviation and the according fitting procedure of  $\beta_p$  functions parameters. Nevertheless, going one step further and analyzing the viscous fluid limit ( $f \rightarrow 0$ ) with  $\eta'$  for  $f = 10^{-2}$  Hz, we are able to compare some classical formulas for the effective viscosity  $\eta^R$  with our derived function  $\beta_p$ . As a first comparison, Einstein's equation [11] yields a linear relationship in dependency of the volume fraction of the filler  $n^p$  and reads

$$\eta^R = \eta^b \left( 1 + \frac{5}{2} n^p \right), \quad (4.5)$$

with  $\eta^b$  describing the viscosity of the pure bituminous binding agent for  $f = 10^{-2}$ . Another relation for the effective viscosity is given by Thomas [85] which takes the form

$$\eta^R = \eta^b \left[ 1 + \frac{5}{2} n^p + g(n^p) \right] \quad (4.6)$$

with a nonlinear function  $g(n^p)$  proposed as

$$g(n^p) = 10.05 (n^p)^2 + 0.00273 \exp(16.6 n^p). \quad (4.7)$$

If  $g(n^p) = 0$ ,  $\eta^R$  is linear in  $n^p$  as proposed by Einstein [11]. Considering a maximum filler volume fraction in terms of dense packing, which we already introduced in the beginning of this section as  $n_{\max}^P = 0.69$ , further formulas from literature can be considered for a comparison. As an example, the effective viscosity formula by Chong

et al. [6]

$$\eta^R = \eta^b \left[ 1 + 0.75 \left( \frac{n^p/n_{\max}^p}{1 - n^p/n_{\max}^p} \right) \right]^2 \quad (4.8)$$

makes use of this information. In Figure 4.10, we compare the three introduced approaches with the new function  $\beta_p$  for the viscous fluid limit ( $f = 10^{-2}$  Hz). By definition, all models converge towards  $\eta^b$  for  $n^p \rightarrow 0$ . Based on the experimental data, the new model predicts higher viscosities. This tendency is most likely owed to the facts which are already described for the elastic limit.

At this point we want to recall that our extension of the master-curve concept is only based on the given experimental data and the fact that we have self similar curves. This puts us in position to use only mathematical conditions to generate a function which can be used to create a master-curve for any given 20/30 bitumen-filler mastic for different reference temperatures. This enables us to create a master-curve for a not given filler concentration for further investigations or as data for material modeling in terms of rheological models, such as fractional models [81], nonlinear viscoelastic rheological models [31, 70], generalized Maxwell-Zener models or even fractional derivatives and recurrent neural networks [57].

## 4.4 Conclusions

In this chapter, the workflow from experimental data to an extended master-curve concept is described. In dependency of filler concentration and frequency, the extension is conducted on the basis of broad experimental DSR data. Our workflow is motivated by the observation that the experimental data shows self similar master-curves. With the classical WLF function and its shift factor  $\alpha_\theta$ , the described approach is an extension with a second shift factor  $\beta_p$ . Combination of both shift procedures allow to define a generalized master-curve with respect to temperature  $\theta$  and filler mass fraction  $w^p$  on the basis of a single set of experimental data for a bituminous binding agent, in this case 20/30 penetration grade bituminous binder. The agreement between the defined function for  $\beta_p$  and the experimental data is very good and the presented workflow can easily be applied to any other thermo-rheologically simple bitumen-filler mastic.

## Appendix

To complete the master-curve concept and to underline the quality of the data, Figure 4.11 a) and b) show the corresponding master-curves for the storage modulus  $G'$  and loss modulus  $G''$  as post-processed quantities from the dynamic modulus master-curve in Figure 4.2 b). Figure 4.12 shows the corresponding master-curves for the storage modulus  $G'$  and loss modulus  $G''$ . Again, these master-curves are post-processed from the master-curves of the dynamic modulus  $|G^*|$  in Figure 4.4 a). Another point

to mention is an interesting finding in the experimental data post-processed from the quantities from the dynamic modulus master-curves in Figure 4.4 a) for the different filler mass fractions  $w^p$ . In particular, in Figure 4.12 b). It occurs that the peak for each master-curve is shifted in frequency direction. Depending of the amount of admixed filler, the bituminous binding agent shows a varying frequency for the maximum dissipation and, by implication, for the maximum attenuation too. The higher the mass fraction  $w^p$  the lower the peak frequency. This is of high interest in road construction, where the attenuation plays an important role for the choice of an appropriate bitumen-filler mastic. Figure 4.12 a) shows the corresponding master-curves of storage modulus  $G'$ .

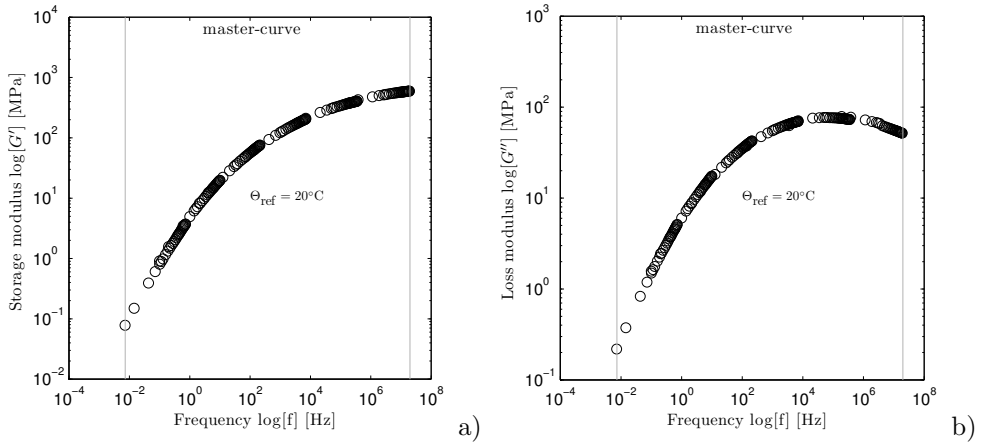


Figure 4.11: a) Master-curve for storage modulus  $G'$  and loss modulus  $G''$  for pure 20/30 penetration grade bituminous binder.

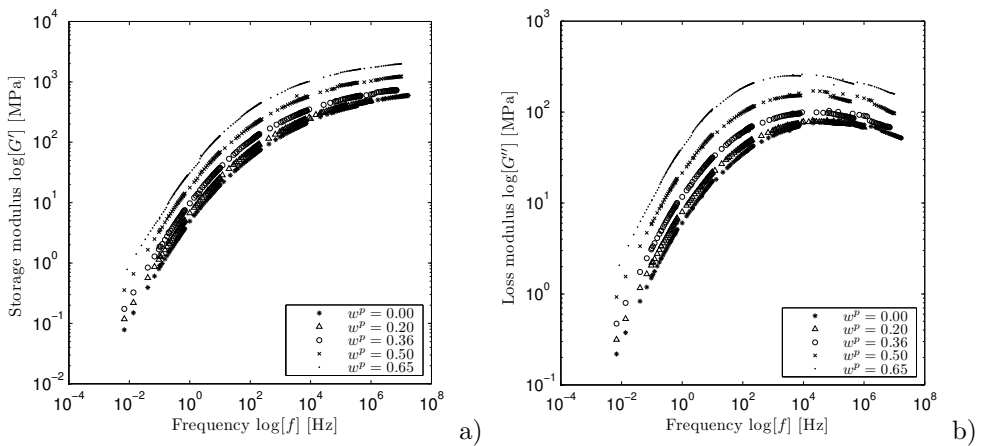


Figure 4.12: a) Master-curves of storage modulus  $G'$  and loss modulus  $G''$  for five different filler mass fractions  $w^p$ .



## Chapter 5

# Multi-scale modeling of elastic/viscoelastic compounds<sup>1</sup>

*This chapter is concerned with the requirements of an efficient multi-scale modeling approach for elastic/viscoelastic compounds such as bituminous asphalt concrete. Typically, this heterogeneous composite material consist of a mineral filler (e.g. crushed rock), a bituminous binding agent, pores and further additives. The contrast in stiffness between the different constituents is extremely high and accounts for several orders of magnitude. Prediction of effective mechanical properties of such complex materials on the macroscopic level requires a detailed knowledge of the micro-scale behavior of the particular constituents. In this chapter, the focus lies on modeling aspects due to upscaling routines based on volume averaging. Particularly, we will show that the choice of micro-level boundary conditions not only influences the effective stiffness of the viscoelastic substitute material (upper/lower limit), but also the viscous contribution to the macro-model (shift of maximal attenuation in frequency space). In order to study these fundamental homogenization properties, we introduce a simplified compound consisting of homogeneous viscoelastic binder phase and spherical filler particles with a volume fraction low compared to realistic asphalt concrete. Depending on the chosen boundary condition, stress-relaxation and creep tests are considered. After transformation of the effective stress-strain-relations from time- to frequency space, the viscoelastic properties of the compound will be discussed in frequency domain.*

---

<sup>1</sup>This chapter is published in *Journal of Applied Mathematics and Mechanics* [72] and a preliminary study in *Proceedings in Applied Mathematics and Mechanics*. [73]

## 5.1 Introduction

Highly heterogeneous viscoelastic compounds such as bituminous asphalt concrete are widely used materials e.g. in road constructions. Their alterable properties make them suitable for the most diverse fields of application under complex environmental influences. The effective properties of the compound material are strongly dominated by the underlying micro-morphology. Therefore, these materials are still a challenging matter of research.

First, asphalt concrete as a typical representative for viscoelastic compounds is a multi-phase material, which typically consists of a mineral filler, a bituminous binding agent and pores cf. [34, 87], to name only a few. However, further constituents such as polymers or waxes are admixed in various applications. The constituents are chosen with respect to the application requirements and in order to guarantee a durable usage. This means that the choice of the asphalt type and its constituents basically depends on the expected mechanical loading and the environmental influences (changing temperature, chemical modifications, abrasion etc.). For that reason it is necessary to carry out an extensive survey of the case of application for the particular asphalt composition.

Second, bituminous asphalt is also a multi-scale material accounting for a highly heterogeneous micro-level due to the particular constituents and their micro-morphology. However, for engineering applications we are interested in external loadings and exposures which take place on the effective level (macro-scale). Hence, we would like to interpret bituminous asphalt as an homogeneous substitute medium whose macro-scale material properties are controlled by the underlying micro-morphology.

In literature, a wide range of research activities are to be found concerning the continuum-mechanical characterization of bituminous asphalt concrete and further viscoelastic compounds. Various contributions base on the so-called Huet- or Huet-Sayegh model [31, 44, 70] introducing a nonlinear dashpot element on the effective level. These approaches basically focus on a phenomenological macro-scale modeling and do not take into account microscopic processes in an explicit manner. However, by means of modern visualization and image segmentation techniques (X-Ray Computed Tomography - XRCT), detailed information about micro-scale properties such as volume fractions and morphology of the constituents is available. Moreover, also the mechanical properties of the particular microscopic constituents are known. Therefore, it appears to be reasonable choosing alternatively scale-bridging approaches in order to determine the effective material properties making use of the available micro-scale data. Basically, two different upscaling methodologies are to be found in literature: The mathematical (asymptotic) homogenization scheme [16, 69, 84] on the one hand, homogenization by volume averaging [28, 56] on the other. In the present chapter we apply the latter homogenization technique.<sup>2</sup>

---

<sup>2</sup>The following study will be restricted to the regime of small deformations. Nevertheless, large (local and/or effective) deformations of asphalt concrete can be expected to be relevant in realistic

The derivation of an effective material model based on realistic micro-scale data requires an enhanced modeling concept:

- The microscopic information has to be sampled. Basically, this step can be split into two parts. On the one hand, the local morphology of the compound has to be included. This can be achieved by modern imaging techniques such as XRCT, respectively. After image segmentation, the resulting 3-dim information can be included in the modeling routine one-by-one. Alternatively, the data may be used to generate artificial representatives accounting for particularly desired properties, i.e. periodicity for example. On the other hand, the mechanical properties of the micro-constituents have to be evaluated. In case of the bituminous binder this can be achieved by rheological investigations on the bulk material.
- The upscaling routine of the viscoelastic properties from the micro- to the macro-level requires a numerical implementation, for example in terms of FE<sup>2</sup> methodology. Usually, the underlying Finite Element computations take place in the time domain. In particular, having regard to 3-dim simulations with detailed resolution, numerical efficiency is crucial in this point. Besides parallelization techniques [76], also more enhanced algorithmic approaches are to be taken into account [19].
- The effective viscoelastic properties gathered in the time domain are to be interpreted in the frequency domain. Accounting for complex frequency-dependent material parameters, for example.

In the present study, we do not intend to cover the entire modeling path for realistic microstructures of asphalt concrete. Nevertheless, we would like to concentrate on three particular points. First, the focus will be on the characterization of the micro-scale material properties. Based on experimental studies on the bituminous binder, its viscoelastic properties as well as the linear-elastic properties of the mineral filler will be determined. The material data on the micro-level will be used to generate artificial, simplified microstructures in order to, second, discuss the homogenization concept itself. We will show that the choice of the loading setup, that is the choice of boundary conditions (Dirichlet or Neumann type) as well as the particular implementation (uniform displacements/tractions or accounting for certain disturbances such as periodic ones), is crucial for the reliability of the observed effective viscoelastic properties. Besides the well-known impact of boundary conditions on effective stiffness we will highlight the influence of chosen boundary setting on the effective load settings.

For this purpose, we replace the heterogeneous elastic (mineral filler)/viscoelastic (bituminous phase) mixture on the micro-scale by a homogeneous viscoelastic medium on the effective macro-scale with special regards to the upscaling rules relating the scales. Basically, our approach is comparable to the so-called FE<sup>2</sup> schemes referred in [15, 43, 55], to name only a few. That is, the constitutive relation on the effective level is replaced by a micro-scale computation on a control volume which is considered to be representative for the entire microstructure.

viscosity to be observed in a time- (and frequency-) shift of the effective viscous processes. The third focal point of our study is concerned with the frequency domain evaluation of time domain experiments, in our case carried out as stress-relaxation or creep tests, respectively. Since most of these questions touch fundamental points of the proposed homogenization approach, we do not use realistic asphalt concrete samples for our study but restrict ourselves to 2-dim problems in the context of small deformations (geometric linearity). Our computations are based on artificially produced micro-morphologies of a two-phase compound on the micro-level consisting of circularly shaped filler particles in a homogeneous binder matrix. We use filler volume fractions of about 45% in contrast to 95% for realistic asphalt concrete. Moreover, neither pores nor further additives are taken into account.

The mineral filler particles are handled as linear-elastic solids. Since typical loading frequencies of bituminous asphalt concrete take place in the dynamic loading range of  $1 \text{ Hz} \leq f \leq 10 \text{ Hz}$ , we further make use of linear viscoelastic modeling approaches for both, the bituminous binder on the micro-level and the effective medium on the macro-level, respectively. Mass inertia effects are assumed to play a subordinate role for low frequencies and are therefore neglected.

Our study is organized as follows: In section 5.2, the micro-scale properties of the compound are investigated. On the one hand, the material properties of the mineral filler are discussed based on data available in literature [23]. On the other hand, the viscoelastic behavior of the bituminous phase is characterized by appropriate rheological shear experiments using a Dynamic Shear Rheometer (DSR) in plate-plate geometry. Applying the master-curve concept [14] the micro-scale behavior will be determined for a given reference temperature.

In section 5.3, the aspects of the homogenization approach are pointed out, in particular the various available boundary conditions on the micro-level. Afterwards, we study the effective viscoelastic properties of the compound in section 5.4 with special regard to the influence of local boundary conditions. Finally, the achieved results will be discussed and an outlook on future activities will be given.

Throughout this study, quantities of the micro- and the macro-scale are referred to as  $\diamond$  and  $(\diamond)$ , respectively.

## 5.2 Micro-scale modeling

As indicated above we assume the compound to consist of two phases, namely the bituminous binding agent and the mineral filler particles. The effective mechanical properties of this multi-phase material will be determined by an appropriate homogenization approach. Therefore we start to analyze the properties of the inherent phases. First, we presume linear-elastic behavior for the mineral filler. The quantification of the mechanical properties of the mineral filler is based on relevant literature [23]. The tests have been carried out on the rock type Diabas, which is a common mineral filler for asphalt concrete. Since the mineral filler is several orders of magnitude stiffer

than the surrounding bituminous binder, varying stiffness properties of the mineral filler have only a minor influence on the effective properties of the composite. For our computations, we use the bulk modulus  $K^s = 56.2$  GPa and the shear modulus  $G^s = 32.0$  GPa.

By contrast, we characterize the bituminous binder as a linear viscoelastic material. The rheological behavior of the bituminous binder is determined by the Dynamic Shear Rheometer (DSR) Anton Paar Physica MCR 101. A plate-plate configuration (plate radius  $r=8$  mm) has been chosen. Investigations take place for different temperatures  $\theta$  under iso-thermal conditions. Shear oscillations in a predefined frequency range from  $0.1 \text{ Hz} \leq f = \omega/(2\pi) \leq 10 \text{ Hz}$  are performed. The temperature range is chosen  $-20^\circ\text{C} \leq \theta \leq 30^\circ\text{C}$  in intervals of  $10^\circ\text{C}$ . All experiments are carried out for the pure 20/30 penetration grade bituminous binder. Based on the purely deviatoric DSR experiments we are able to characterize the viscoelastic behavior of the bituminous binder in the mentioned temperature range. However, no clear statement can be made in view of the bituminous compressibility. That implies that we assume the binder to be incompressible. Hence, the DSR experiments enable us to determine the viscoelastic properties in form of the complex shear modulus  $G_m^*(\omega)$  and its phase angle  $\delta_m(\omega)$ , cf. [51]. The definition of the complex modulus reads

$$G^* = G' + iG'' \quad \text{with} \quad \tan \delta = \frac{G''}{G'}. \quad (5.1)$$

$G'(\omega)$  represents the storage modulus and  $G''(\omega)$  the loss modulus, respectively. The storage modulus

$$G' = \frac{\tau_0}{\gamma_0} \cos \delta \quad (5.2)$$

is an index for the stored energy which means it corresponds to the elastic part of deformation. The loss modulus

$$G'' = \frac{\tau_0}{\gamma_0} \sin \delta \quad (5.3)$$

quantifies the viscous energy contribution which is dissipated as heat.  $\delta(\omega)$  is an indicator for the phase lag between the occurring stress and strain. In case the phase angle  $\delta(\omega)$  equals  $\pi/2$ , it can be stated that the investigated material is purely viscous. For  $\delta(\omega) = 0$ , the investigated material is of elastic nature. Values in between these extrema correspond to viscoelastic material behavior.

Furthermore, we introduce the dynamic shear modulus  $|G^*|$ . The loss factor is defined as  $\tan \delta(\omega)$ . The DSR measurements are shown in Figure 5.1 in terms of the storage and the loss modulus. For the identification of the appropriate viscoelastic model in the frequency domain we have used the experimental results in form of the dynamic shear modulus  $|G^*|$ , cf. Figure 5.2. In various investigations, pure bituminous binders have been identified as thermo-rheologically simple materials [8, 94] and references

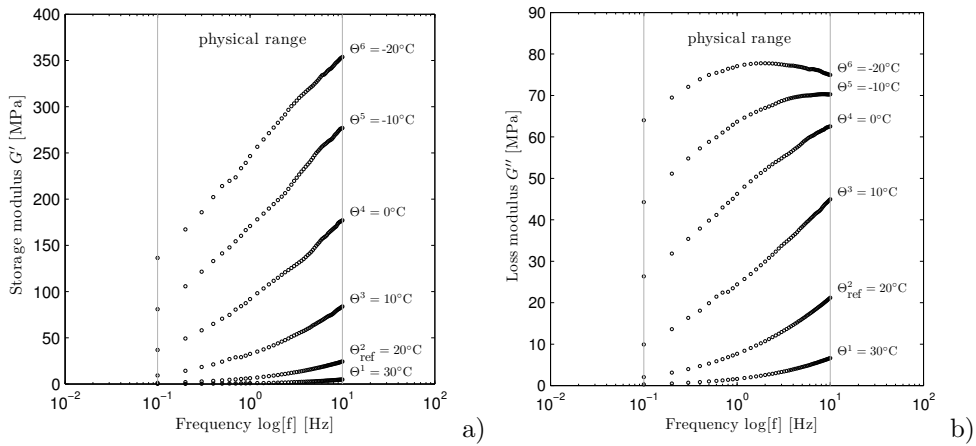


Figure 5.1: **a** Storage modulus  $G'$  and **b** loss modulus  $G''$  gained by DSR experiments for non-modified 20/30 binder. The results for six different temperatures in a frequency range from  $10^{-1}$  Hz to  $10^1$  Hz are shown.  $\Theta = 20^\circ\text{C}$  is chosen as the reference temperature for the master-curve.

therein. Therefore, we apply the time-temperature superposition principle.

It is evident that the investigated pure bituminous binder has a dominating fluid like character at low frequencies. That is  $\delta(\omega \rightarrow 0) \approx \pi/2$  for the chosen reference temperature  $\theta_{\text{ref}} = 20^\circ\text{C}$ . Although we have performed experiments in a wide temperature range and large frequency variety, we are not able to fully describe the solid-like rheological behavior at low temperatures, high frequencies, respectively. Please note that the temperature and frequency testing domain is restricted by the used DSR. The obtained master curve already covers a large frequency range. However, we are not able to describe the high-frequency domain for the dynamic modulus.

In general, various rheological models are suitable to adapt the experimentally obtained dynamic modulus of bituminous binder. In literature, fractional models [81], nonlinear viscoelastic rheological models [31, 70] and generalized Maxwell-Zener models are to be found. In the present study we refer to the generalized Maxwell-Zener model for several reasons: First, the Maxwell-Zener model can be easily extended to a 3-dim formulation based on the concept of internal variables [80]. This allows a robust and efficient numerical implementation in Finite Element codes. Second, only a subset of the observed frequency range is used for engineering applications although the master curves cover a huge frequency domain. Doing so, Maxwell-Chains out of the frequency range of interest can be neglected. Third, the characteristic frequencies of the bituminous binder related to discrete Maxwell-Chains can be directly compared with the related frequencies of the homogenized medium. Using the generalized Maxwell-Zener model, cf. Figure 5.3, it has been found that 7 linear spring-dashpot chains are required in order to describe the viscoelastic behavior of

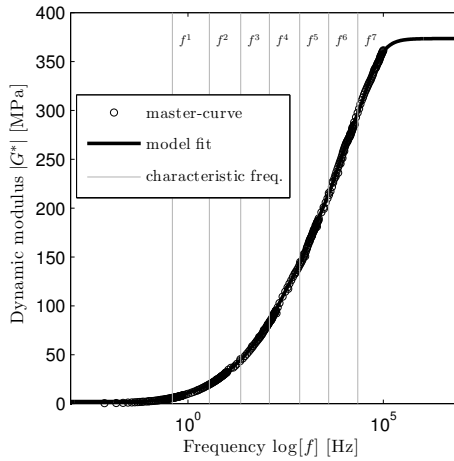


Figure 5.2: Experimental DSR results for the dynamic modulus  $|G^*|$  with master-curve (non-modified 20/30 binder). The characteristic frequencies for the generalized Maxwell-Zener model are indicated by the thin gray lines.

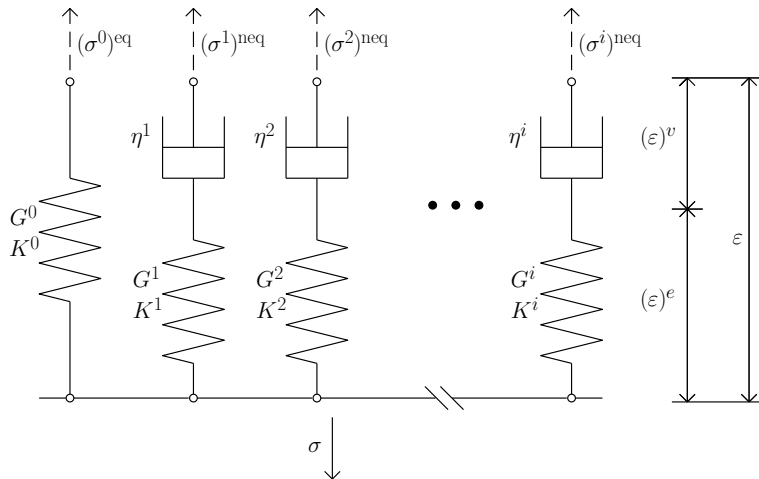


Figure 5.3: 3-dim generalized Maxwell-Zener model. The incompressibility of the binder is considered due to the fact, that  $K^i \gg G^i$ .

the bituminous binder, cf. Figure 5.2. According to the characteristic frequencies of the Maxwell-Chains  $f^i$ ,  $i = 1, \dots, 7$ , cf. Table 6.1, it has to be noted that we are physically not interested in modeling the high-frequency plateau region.

Next, we would like to recall the theory of linear viscoelasticity based on the gen-

Table 5.1: Experimentally determined parameters of the generalized Maxwell-Zener model.

		$i = 0$	$i = 1$	$i = 2$	$i = 3$	$i = 4$	$i = 5$	$i = 6$	$i = 7$
$G^i$	[MPa]	1.00E+0	4.13E+0	1.06E+1	1.63E+1	2.90E+1	3.56E+1	4.37E+1	4.65E+1
$T^i = \frac{\eta^i}{G^i}$	[s]	-	2.51E+0	2.80E-1	4.50E-2	8.20E-3	1.40E-3	2.50E-4	4.50E-5
$f^i = \frac{G^i}{\eta^i}$	[Hz]	-	4.00E-1	3.57E+0	2.22E+1	1.22E+2	7.14E+2	4.00E+3	2.22E+4

eralized Maxwell-Zener model and its extension to the 3-dim case [80]. The whole procedure is based on the rheology depicted in Figure 5.3. The starting point is provided by the stress coherence that the total stress  $\boldsymbol{\sigma}$  is the sum of the equilibrium part  $\boldsymbol{\sigma}^{\text{eq}}$  and the non-equilibrium part  $\boldsymbol{\sigma}^{\text{neq}}$ ,

$$\boldsymbol{\sigma} = \boldsymbol{\sigma}^{\text{eq}} + \boldsymbol{\sigma}^{\text{neq}}. \quad (5.4)$$

In addition to the stress coherence, the strain tensor  $\boldsymbol{\varepsilon}$  is split into an elastic part  $\boldsymbol{\varepsilon}^e$  and a viscous part  $\boldsymbol{\varepsilon}^v$

$$\begin{aligned} \boldsymbol{\varepsilon} = \boldsymbol{\varepsilon}^e + \boldsymbol{\varepsilon}^v &= (\boldsymbol{\varepsilon}^e)^{\text{vol}} + (\boldsymbol{\varepsilon}^e)^{\text{dev}} + (\boldsymbol{\varepsilon}^v)^{\text{vol}} + (\boldsymbol{\varepsilon}^v)^{\text{dev}} \\ &\text{and} \\ \boldsymbol{\varepsilon}^{\text{vol}} &= \frac{1}{3} (\text{tr } \boldsymbol{\varepsilon}) \mathbf{I} \end{aligned} \quad (5.5)$$

with the second order unity tensor  $\mathbf{I}$ . The resulting constitutive equation for the total stress of the bituminous binder reads

$$\boldsymbol{\sigma} = K (\boldsymbol{\varepsilon})^{\text{vol}} + 2 G^0 (\boldsymbol{\varepsilon})^{\text{dev}} + \sum_i K (\boldsymbol{\varepsilon}^{e,i})^{\text{vol}} + 2 G^i (\boldsymbol{\varepsilon}^{e,i})^{\text{dev}}. \quad (5.6)$$

The constitutive framework is closed by the evolution equations for the viscous deviatoric strain of the particular Maxwell-Chains

$$(\dot{\boldsymbol{\varepsilon}}^{v,i})^{\text{dev}} = \frac{2}{\tau^i} \left[ (\boldsymbol{\varepsilon}^i)^{\text{dev}} - (\boldsymbol{\varepsilon}^{v,i})^{\text{dev}} \right]. \quad (5.7)$$

The earlier mentioned incompressibility of the bituminous binder is satisfied by a choice for the bulk modulus  $K$  which is chosen five orders of magnitude larger than the particular shear modulus  $G$ . This assumption holds for the equilibrium part as well as for the elastic parts of the Maxwell-Chains,

$$K^0 \gg G^0 \quad \text{and} \quad K^i \gg G^i. \quad (5.8)$$

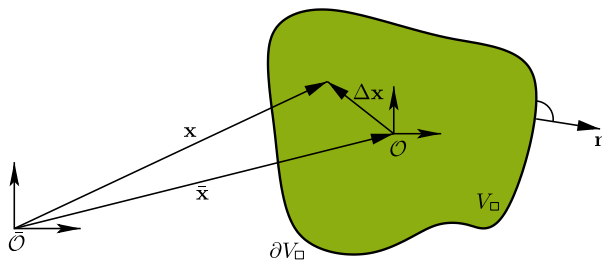


Figure 5.4: Each material point of the effective medium at position  $\bar{\mathbf{x}}$  is identified with an attached micro-volume  $V_\square$  at the local position  $\Delta \mathbf{x} \ll \bar{\mathbf{x}}$ .

Therefore, the incompressibility constraint is modeled by one single bulk modulus  $K = K^0 = K^i = 1\text{E}+6$  MPa in our model. In the context of a Finite Element setting, the bulk modulus  $K$  acts as a penalty parameter and we are still able to work with a pure displacement formulation.

### 5.3 Macro-scale modeling by homogenization

The strongly heterogeneous properties of our compound require an enhanced modeling technique. In particular, it is useful to introduce a scale separation between the heterogeneous micro-scale (fillers and wetting bituminous phase) and the homogeneous macro-scale (effective level, viscoelastic medium). This can be achieved, for example, by standard homogenization algorithms [28, 56] in the context of a mean-field approach. Based on appropriate scale-transition rules, the effective deformation and stress quantities are to be derived from a representative part of the micro-scale by volume-averaging procedures. As stated earlier,  $(\bar{\diamond})$  and  $(\diamond)$  refer to physical quantities of the macro- and the micro-scale, respectively.

The basic idea of homogenization by volume-averaging is to replace the micro-heterogeneous medium by a homogeneous substitute medium on the effective level accounting for identical mechanical properties. For this purpose, let us consider an arbitrary-shaped micro-volume  $V$  which we consider to be representative for the entire microstructure. It is nested to the effective material point in its volume centroid  $\bar{\mathbf{x}}$ , cf. Figure 5.4. Any local position can be pointed on by the overall position vector  $\mathbf{x} = \bar{\mathbf{x}} + \Delta \mathbf{x}$ . For the upcoming considerations, let us introduce the definition of averaging over the micro-volume  $V_\square = \int_{V_\square} dv$

$$\bar{\diamond} = \langle \diamond \rangle_\square = \frac{1}{V_\square} \int_{V_\square} \diamond dv \quad (5.9)$$

In general, two different choices can be met:

- First, we may prescribe a Dirichlet boundary value problem on the micro-level. The local displacement field  $\Delta \mathbf{u}$  then depends on the macroscopic deformation

state  $\bar{\varepsilon}$ . Solving the microscopic boundary value problem, the stress response  $\sigma(\Delta\mathbf{x}, t)$  of the microstructure can be transferred back to the effective level  $\bar{\sigma}(\bar{\mathbf{x}}, t)$ .

- Second, we may assume a microscopic Neumann boundary value problem depending on the macro-scale stress state  $\bar{\sigma}(\bar{\mathbf{x}}, t)$ . After solution, the effective micro-scale deformation response  $\bar{\varepsilon}(\bar{\mathbf{x}}, t)$  has to be interpreted in terms of the effective deformation state.

These two possibilities are commonly stated as Voigt- and Reuss-boundaries, respectively, because they represent upper and lower bounds for the estimated effective material properties of the underlying microstructure [28, 56]. However, the significance of Dirichlet- or Neumann-boundary conditions on the micro-level becomes even more peculiar if viscous material properties come into play: Besides their role as upper and lower bounds, the choice of micro-scale Dirichlet or Neumann boundary conditions moreover dictates the character of the experiment, that is stress-relaxation versus creeping. By consequence, the transient character of both choices cannot be compared any more one by one. In the sequel, we will discuss both cases in detail.

### 5.3.1 Microscopic Dirichlet boundary value problem – local stress relaxation test

The definition of microscopic Dirichlet boundary conditions requires a relation between the local displacement field  $\Delta\mathbf{u}(\Delta\mathbf{x}, t)$  and the overall deformation state at the corresponding macroscopic material point  $\bar{\varepsilon}(\bar{\mathbf{x}}, t)$ . Please note that all deformations and stresses in the context of homogenization are considered to equal the total deformations and total stresses, that is viscous deformations and stresses are not considered separately. Looking for the effective displacement field  $\bar{\mathbf{u}}(\bar{\mathbf{x}}, t)$  that best fits the underlying micro-scale displacement field  $\langle\mathbf{u}\rangle_{\square}$  in the volume average over  $V_{\square}$  [36], the kinematic averaging rules can be derived as

$$\begin{aligned}\bar{\mathbf{u}} = \langle\mathbf{u}\rangle_{\square} &\Leftrightarrow \langle\Delta\mathbf{u}\rangle_{\square} = \mathbf{0} \quad \text{and} \quad \bar{\varepsilon} = \overline{\text{grad}}^{\text{sym}} \bar{\mathbf{u}} \\ &= \langle\text{grad}^{\text{sym}} \Delta\mathbf{u}\rangle_{\square} = \frac{1}{V_{\square}} \int_{\partial V_{\square}} (\Delta\mathbf{u} \otimes \mathbf{n})^{\text{sym}} da\end{aligned}\quad (5.10)$$

with the surface  $\partial V_{\square}$  of the micro-volume and its outer normal vector  $\mathbf{n}$ . In order to satisfy the averaging rule Eq. (5.10), the straight-forward choice of the local displacement field on the boundary  $\partial V_{\square}$  takes a linear form and reads

$$\Delta\mathbf{u}(\Delta\mathbf{x}) = \bar{\varepsilon} \cdot \Delta\mathbf{x} + \Delta\tilde{\mathbf{u}}. \quad (5.11)$$

The perturbation  $\Delta\tilde{\mathbf{u}}$  has to be chosen in a way that the averaging rule Eq. (5.10) is valid. Since the present study is restricted to geometrically periodic micro-volumina, the perturbation  $\Delta\tilde{\mathbf{u}}$  is chosen periodic at homologous points of the micro-volume surface  $\partial V_{\square}$  [56]. For non-periodic micro-volumina, additional integral constraints could

be introduced in order to determine an appropriate perturbation field, cf. concept of minimal loading conditions [38, 53].

After the kinematical quantities of micro- and macro-scale have been related to each other, similar relations for the stresses require an additional axiomatic equivalence, namely the Hill-condition [28, 29, 56]

$$\bar{\boldsymbol{\sigma}} : \dot{\bar{\boldsymbol{\varepsilon}}} = \langle \boldsymbol{\sigma} : \dot{\boldsymbol{\varepsilon}} \rangle_{\square} = \frac{1}{V_{\square}} \int_{\partial V_{\square}} \Delta \dot{\mathbf{u}} \cdot (\boldsymbol{\sigma} \cdot \mathbf{n}) \, da. \quad (5.12)$$

The Hill-condition requires the macroscopic strain energy rate at the material point  $\bar{\mathbf{x}}$  to equal its microscopic counterpart in an averaged sense. Inserting the displacement field Eq. (5.11) in Eq. (5.12) we end up with the relation

$$\bar{\boldsymbol{\sigma}} = \frac{1}{V_{\square}} \int_{\partial V_{\square}} (\mathbf{t} \otimes \Delta \mathbf{x})^{\text{sym}} \, da, \quad (5.13)$$

where  $\mathbf{t} = \boldsymbol{\sigma} \cdot \mathbf{n}$  represents the microscopic surface traction vector on  $\partial V_{\square}$ . Whereas the periodicity condition requires periodic perturbations at homologous points of the boundary, the related surface tractions must be anti-periodic. We write

$$\Delta \tilde{\mathbf{u}}^+ = \Delta \tilde{\mathbf{u}}^- \quad \text{and} \quad \mathbf{t}^+ = -\mathbf{t}^- \quad (5.14)$$

at homologous points of the boundary  $\partial V_{\square}$ .

### 5.3.2 Microscopic Neumann boundary value problem – local creep test

Vice versa, also the relation between micro- and macro-scale stresses can be used as a starting point for the homogenization algorithm. For this purpose, we assume the total stress on the macro-level to equal the volume average of the microscopic stress state  $\bar{\boldsymbol{\sigma}} = \langle \boldsymbol{\sigma} \rangle_{\square}$ . In order to ensure this condition to be satisfied, one may choose constant tractions  $\mathbf{t}$  on the micro-boundary  $\partial V_{\square}$

$$\mathbf{t} = \bar{\boldsymbol{\sigma}} \cdot \mathbf{n}. \quad (5.15)$$

The constant tractions  $\mathbf{t}_m$  on the micro-boundary  $\partial V_{\square}$  depending on the macroscopic stress field  $\bar{\boldsymbol{\sigma}}$ , cf. Eq. (5.15), are to be inserted into the Hill-condition Eq. (5.12). We find

$$\dot{\bar{\boldsymbol{\varepsilon}}} = \langle \dot{\boldsymbol{\varepsilon}} \rangle_{\square} = \langle \text{grad}^{\text{sym}} \Delta \dot{\mathbf{u}} \rangle_{\square} \Rightarrow \bar{\boldsymbol{\varepsilon}} = \langle \boldsymbol{\varepsilon} \rangle_{\square} = \langle \text{grad}^{\text{sym}} \Delta \mathbf{u} \rangle_{\square}. \quad (5.16)$$

After integration in time, the resulting integration constant has to be evaluated by the initial conditions. Reasonably, one assumes a stress-free state at the initial time. For geometrically periodic micro-volumina, anti-periodic tractions and periodic perturbations of the displacement field are again possible.

### 5.3.3 Effective viscoelastic properties on the macro-scale

It is the aim of the homogenization scheme to numerically calculate effective linear viscoelastic properties of the composite comparable to those obtained by DSR measurements for the bituminous binder. Therefore, we formulate boundary value problems which we solve numerically. We obtain a time dependent response of the material expressed in  $\bar{\sigma}(t)$  and  $\bar{\varepsilon}(t)$ . As stated earlier, the present study is up to 2-dim problems in the  $\mathbf{e}_1 - \mathbf{e}_2$ -plane. Moreover, the simplifying assumption is met that the bituminous binder is incompressible and can be mechanically described by application of the generalized Maxwell-Zener model. The mineral filler phase is assumed to be linear-elastic and accounts for a shear stiffness five times larger than the particular counterparts of the bituminous binder. Due to the high bulk modulus of the mineral filler, cf. section 5.2, the compound behaves nearly-incompressible. The only remaining material parameter to be identified by the upscaling methodology is the effective shear modulus  $\bar{G}$ . Hence, only the symmetric shear mode depending on the shear component  $\bar{\varepsilon}_{12}(t)$  in Eq. (5.11), on  $\bar{\sigma}_{12}(t)$  in Eq. (5.15), respectively, will be examined in the upcoming considerations. As it has been stated before, the choice of the local boundary conditions influences the character of the experiment. In the present study, basically three different formulations of local boundary conditions are compared: Dirichlet boundary conditions (linear displacements field without periodic perturbation), periodic boundary conditions (Dirichlet boundary conditions with periodic perturbations) and Neumann boundary conditions (constant surface traction without periodic perturbation). They take the form of stress relaxation or creep tests, respectively, depending on the choice of the discussed boundary conditions. The time-dependent stress and strain values are transferred to frequency space with a discrete Fourier transform. Thus, we obtain  $\bar{\sigma}(\omega)$  and  $\bar{\varepsilon}(\omega)$ . From the frequency-dependent stress-strain quantities of a shear test, we are finally able to determine the effective complex shear modulus  $\bar{G}(\omega)$ ,

$$\bar{G}(\omega) = \frac{\dot{\bar{\sigma}}_{12}(\omega)}{2\dot{\bar{\varepsilon}}_{12}(\omega)}. \quad (5.17)$$

Further technical details related to the determination of  $\bar{G}(\omega)$  can be found for example in [62].

## 5.4 Viscoelastic properties on the effective scale

In the subsequent investigations we would like to go first steps towards a unified multi-scale modeling framework for viscoelastic composites. We focus on the influence of the transient character of stress-relaxation and creep test, respectively. In the present study, we consider a viscoelastic compound under the following assumptions:

- The problem is reduced to 2-dim plain strain in the  $\mathbf{e}_1 - \mathbf{e}_2$ -plane.
- The volume elements underlying our micro-scale computations account for mineral filler volume fractions of about 45%. The random distribution of the filler

particles has a uniform character, overlapping of neighboring particles is excluded. Moreover, the filler particles are arranged in a periodic manner. That is, the resulting volume element can be continued periodically, depending on the size of the unit cell.

- The viscous bituminous binder is assumed to be incompressible. As explained earlier this leads to a nearly-incompressible mixture.

The high complexity of the micro-morphology of realistic bituminous asphalt concrete is out of the scope of the following considerations and remains a challenging issue. Being aware of these limiting assumptions we will derive several qualitative conclusions in the following. For the numerical simulations, the generalized Maxwell-Zener model has been implemented in the numerical Finite-Element system COMSOL Multiphysics<sup>®</sup>. The micro-level displacement field has been discretized using triangular elements and quartic shape functions of Lagrange type. Mesh convergence has been ensured introducing an error norm  $e(t_\infty)$  based on the error of the effective shear stress  $\langle \sigma_{12}(t_\infty) \rangle$  at time  $t \rightarrow \infty$

$$e(t_\infty) = \frac{\langle \sigma_{12}(t_\infty) \rangle_\square - \langle \sigma_{12}^{\text{ref}}(t_\infty) \rangle_\square}{\langle \sigma_{12}^{\text{ref}}(t_\infty) \rangle_\square}. \quad (5.18)$$

#### 5.4.1 Influence of the micro-scale boundary conditions

Let us first study the boundary conditions on the level of the unit-cell and their impact on the effective material behavior. For this purpose, we perform numerical simulations making use of the previously discussed loading conditions, namely linear displacement boundary conditions with (PBC) and without (Dirichlet) periodic perturbations as well as constant traction (Neumann) boundary conditions. For the computations in this section we use the microstructure given in Figure 5.5. In order to highlight the influence of boundary conditions the volume element is constructed in such a way that one particle is located at the corner. The stress and strain response in time domain for the resulting stress-relaxation and creep tests, respectively, are given in Figure 5.6. Please note the Neumann boundary conditions to represent a creep test while linear displacement boundary (Dirichlet) conditions as well as periodic boundary conditions (PBC) perform a stress-relaxation test. From the numerical result in the time domain it is obvious that the effective stress response of the pure Dirichlet boundary conditions is much higher than its counterpart resulting from periodic boundary conditions. Furthermore, the difference between both stress responses strongly depends on time. It seems, the relaxation process in case of periodic boundary conditions to be much more pronounced than for pure Dirichlet boundary conditions. However, we are not able to compare stress-relaxation (Dirichlet, PBC) and creep tests (Neumann) in the time domain. To circumvent this restriction we apply the discrete Fourier transform to obtain the effective complex shear modulus  $\bar{G}^*$  in frequency domain for strain- as well as for stress-driven experiments. In Figures 5.7 and 5.8 the real part

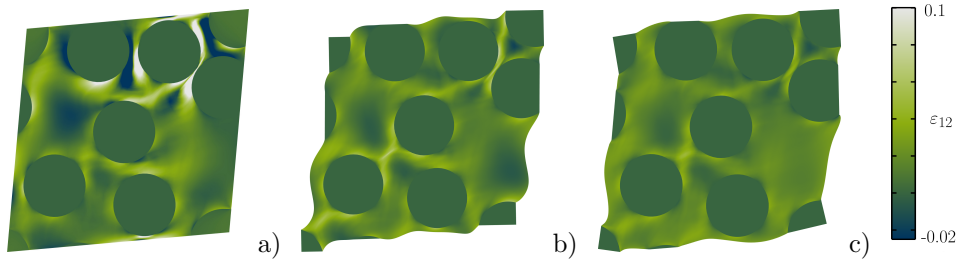


Figure 5.5: Effective shear strain state  $\varepsilon_{12}$  for the different boundary conditions on the micro-level at state of equilibrium ( $t \rightarrow \infty$ ). **a** Linear displacement (Dirichlet) boundary conditions, **b** periodic boundary conditions (PBC) and **c** constant traction (Neumann) boundary conditions for identical effective shear deformation states  $\langle \varepsilon_{12} \rangle$ .

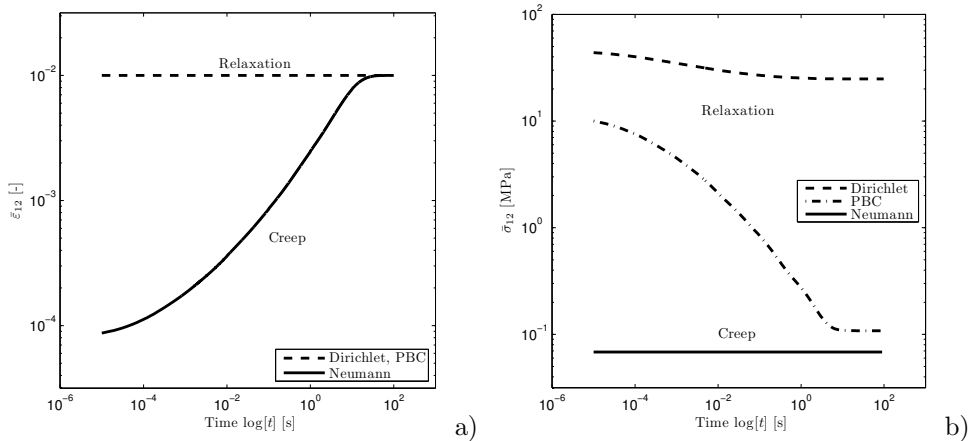


Figure 5.6: Functions of **a** effective shear strain and **b** effective shear stress over the time  $t$ . For linear displacement (Dirichlet) boundary conditions as well as for periodic boundary conditions (PBC), the shear test takes the form of a stress relaxation experiment. If constant traction (Neumann) boundary conditions are considered, the experiment is represented by a creep test.

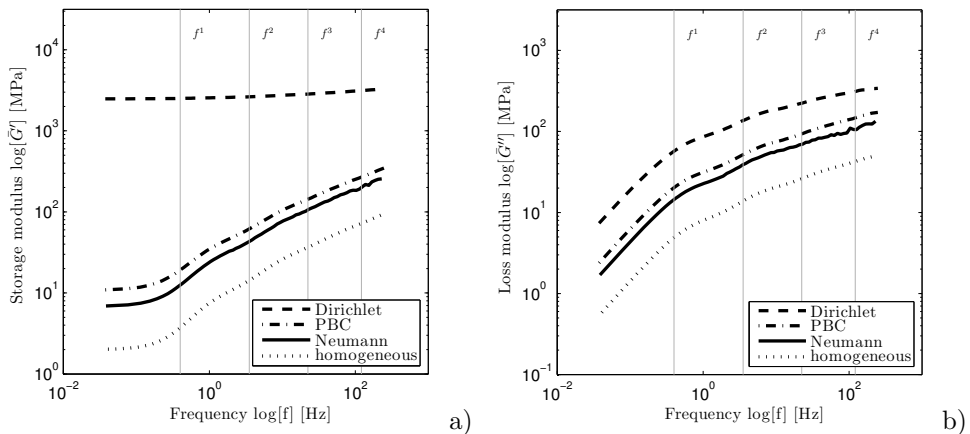


Figure 5.7: **a** Effective storage modulus  $\bar{G}'$  and **b** effective loss modulus  $\bar{G}''$  by the different types of boundary conditions on the micro-level and the homogeneous pure binder.

$\bar{G}'(\omega)$  (storage modulus), the imaginary part  $\bar{G}''(\omega)$  (loss modulus) and the loss factor  $\tan \bar{\delta}(\omega)$  are depicted in the frequency range  $10^{-2} \text{ Hz} < f < 10^3 \text{ Hz}$  in comparison to the pure bituminous binder characterized in the previous section. The typical loading of bituminous asphalt concrete takes place in the range  $1 \text{ Hz} \leq f \leq 10 \text{ Hz}$ . This corresponds to vehicle velocities of about 60 km/h on asphalt concrete pavements [32]. Having regard to Figure 5.7 it is obvious the mixture to be characterized by a higher effective storage modulus in comparison to the pure bituminous binder. However, the large difference between the results of the effective quantities obtained by the different boundary conditions on the unit-cell level is remarkable. Let us discuss two main observations: First, the basic elasticity seems to be dominating for the pure Dirichlet boundary conditions. This can be observed in time dependent stress response Figure 5.6 b) for large relaxation times as well as for the storage modulus  $\bar{G}'(\omega)$  at low frequencies, cf. Figure 5.7 a). The over-estimated basic elasticity can be explained regarding Figure 5.5 a). The corner particles have to strictly follow the prescribed linear displacements of the pure Dirichlet boundary conditions. This results in an unphysical deformation of the corner particles. As it can be observed in Figure 5.5 b) and c) the deformation is concentrated in the much weaker bituminous binder phase for periodic and Neumann boundary conditions. As a consequence, the basic elasticity is dramatically overestimated for the pure Dirichlet boundary conditions. Second, a qualitative difference in the results obtained by the different boundary conditions for the rate dependent response is to be observed compared to the frequency dependency of the pure bituminous binder. Regarding Figure 5.7 b), the loss modulus obtained by pure Dirichlet boundary conditions differs more than 400 % by its counterpart obtained by Neumann boundary conditions. It is notable this effect to be independent of frequency or relaxation time. The intrinsic damping of the material is depicted

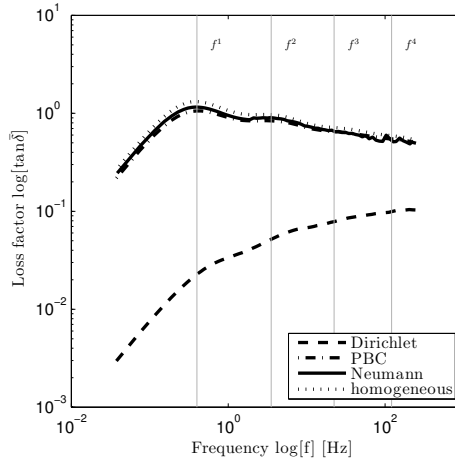


Figure 5.8: Loss factor  $\tan \bar{\delta}$  for the different boundary conditions and the homogeneous pure binder.

in form of the loss factor  $\tan \bar{\delta}(\omega)$  in Figure 5.8. Related to the overestimated basic elasticity, results derived by pure Dirichlet boundary conditions underestimate the intrinsic damping of the mixture. Moreover, the intrinsic attenuation for Dirichlet boundary conditions does not reach any pronounced maximum in the depicted frequency range. This is in contrast to periodic and Neumann boundary conditions, we observe a shift of the critical frequency depending on the formulation of boundary conditions.

It has to be noted that the intrinsic attenuation observed for Neumann and periodic boundary conditions coincide well with the data for homogeneous bituminous binder. In particular the frequency of maximum damping seems to equal  $f^1 = 0.4$  Hz, namely the slowest characteristic frequency of the pure bituminous binder, cf. Table 6.1. Thus, the first characteristic frequency  $f^1$  of the bituminous binder does not lose its predominant prominence for the effective viscoelastic response of the composite.

Moreover, it has to be pointed out that this example is not stochastically representative and it is a quite extremal case due to the positioning of one particle in the corner of the volume element. The dramatic differences between the predicted effective properties are induced by boundary effects and can therefore be expected to reduce with increasing size of the volume element. Independent from the cell size, the results for periodic conditions are, as known from literature, generally bounded by the results for pure Dirichlet (upper bound) and Neumann conditions (lower bound). In the following investigations we use periodic boundary conditions to analyze the effective viscoelastic properties of our compound.

### 5.4.2 Size of Representative Volume Element and effective properties of the compound

In order to determine the effective properties of the viscoelastic compound we first have to carry out the size of a Representative Volume Element. Keeping the filler volume fraction constant, we have therefore varied the size of the volume element between an amount of 4 and 14 filler particles. The results for the loss factor  $\tan \bar{\delta}$  are given in Figure 5.9 a). Obviously, the influence of the unit cell size in the investigated range is minor, the deviation of the different settings is very small. In the following, we consider a set of 7 particles to be representative for this primitive microstructure. Moreover, we further reduce the influence of random morphology by superimposing stress-relaxation curves in time domain for 6 different random arrangements of the 7 particles at constant cell size. The resulting stress-relaxation measurement has been used to identify the effective material parameters of a generalized Maxwell-Zener model on the macro-level. Using the relaxation times given in Table 5.1, the effective parameters of the first four Maxwell-Chains of the model are given in Table 5.2. Under the assumption of material incompressibility, these results comprises the complete information of effective mechanical behavior of the given compound.

In Figure 5.9 b) the master curve for the dynamic modulus  $|\bar{G}^*|$  resulting from the

Table 5.2: Determined parameters of the generalized Maxwell-Zener model for four characteristic frequencies under periodic boundary conditions on the effective scale.

		$i = 0$	$i = 1$	$i = 2$	$i = 3$	$i = 4$
$G^i = \bar{G}^i$	[MPa]	4.09E+0	1.26E+1	3.87E+1	5.41E+1	1.12E+2
$T^i = \bar{T}^i = \frac{\bar{\eta}^i}{\bar{G}^i}$	[s]	-	2.51E+0	2.80E-1	4.50E-2	8.20E-3
$f^i = \bar{f}^i = \frac{\bar{G}^i}{\bar{\eta}^i}$	[Hz]	-	4.00E-1	3.57E+0	2.22E+1	1.22E+2

micro-scale computation is given as well as the fitted curve applying the parameters given in Table 5.2.

Comparing the particular shear moduli in Tables 6.1 and 5.2 we find that the effective shear moduli of the compound are about four times stiffer than their micro-scale counterparts, even for the considered low filler concentration.

## 5.5 Conclusions

In the present study, we have discussed the derivation of effective material properties of viscoelastic compounds by homogenization. In the sense of a mean-field theory we have replaced the heterogeneous elastic/viscoelastic compound on the micro-level by an overall homogeneous viscoelastic medium on the macro-level applying volume av-

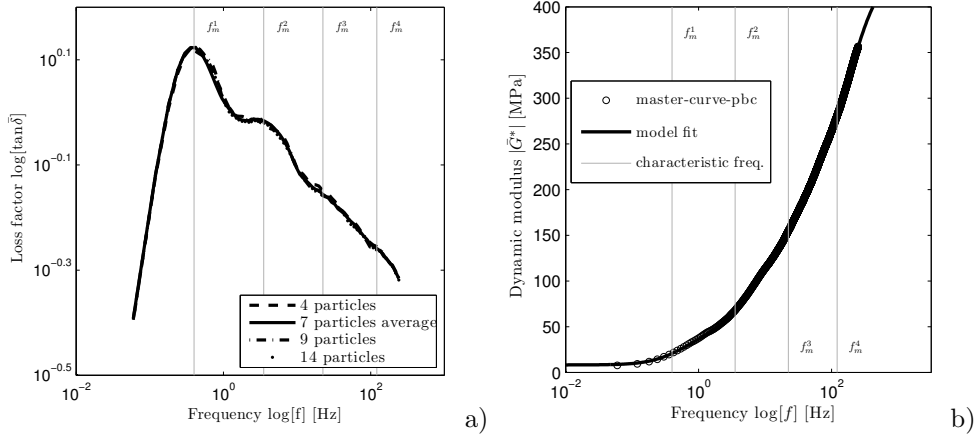


Figure 5.9: **a** Loss factor  $\tan \bar{\delta}$  for four different numbers of particles under periodic boundary conditions. **b** Numerical results and master curve for the dynamic modulus  $|\bar{G}^*|$  with 7 particles. The first four characteristic frequencies for the generalized Maxwell-Zener model are indicated by the thin gray lines.

eraging techniques. Based on data acquired for the constituents of asphalt concrete, we have carried out material studies in order to measure the viscoelastic material properties of the bituminous binder applying the master-curve concept. By knowing the linear-elastic properties of the mineral filler, we were able to set up an artificially simplified heterogeneous elastic/viscoelastic compound. This has allowed us to qualitatively study different aspects of classical homogenization techniques for viscoelastic material properties on both, macro- and micro-scale, within easily manageable computational efforts.

The key findings of our numerical investigations are that,

- first, the micro-scale boundary conditions strongly dominate the effective frequency dependent properties of the compound. On the one hand, the character of pure Dirichlet and Neumann boundary conditions as upper and lower bounds for the resulting effective stiffness in the equilibrium state have been approved. On the other hand, the impact on the viscous, frequency dependent properties have turned out to be even more dramatic. Constant traction (Neumann) and periodic boundary conditions have been found to result in material responses in the frequency domain similar to the pure bituminous binder. By contrast, the effective characteristic frequency of the compound under locally pure linear displacement (Dirichlet) boundary conditions could not be observed within the investigated frequency range.
- Second, for the simplified compound consisting of spherical filler particles accounting for about 45% volume fraction we have determined the effective vis-

coelastic properties over several decades in frequency space. Doing so, the size of the Representative Volume Element for periodic boundary conditions has been identified. Compared to the properties of the pure bituminous binder, the compound has been found about four times stiffer, even for the low filler fraction we have assumed.

At the end of this qualitative study, we would like to point the choice of boundary conditions on the micro-level to be crucial. It influences the effective properties in two ways: Depending on the boundary formulation, the equilibrium processes are predicted stiffer or softer, which is well-known as the upper and lower limit on the effective stiffness (Voigt and Reuss bounds). But, moreover, also the non-equilibrium processes are affected dramatically by the observed effective shift of the critical frequency depending on the chosen boundary condition. For this purpose, a thorough discussion of boundary formulations is necessary. This is particularly the case if more complex microstructures, e. g. from CT-scans of asphalt concrete, are considered, which generally do not show any periodic properties.



## Chapter 6

# Nonlinear modeling and computational homogenization of asphalt concrete on the basis of XRCT scans<sup>1</sup>

*This chapter provides a methodological framework to investigate the effective mechanical properties of asphalt concrete. We, therefore, use numerical tools based on morphological X-Ray Computed Tomography (XRCT) data from asphalt concrete specimens. Asphalt concrete is a multi-component material with spatially varying constituents, but in contrast to many other microstructures used in materials science, the partial microscopic material bulk properties of the constituents of asphalt concrete are accessible by physical testing and, therefore, can be considered as well investigated and known. The information gained by the XRCT is used to create artificial Statistical Volume Elements (SVEs) for our numerical investigations. We apply a discrete particle simulation to generate a densely packed sphere model with a pre-defined Particle Size Distribution (PSD) as a first representation of the mineral filler particles. This model serves as the starting point for a weighted Voronoi diagram. Finally, the volume fractions are adjusted by a stochastic shrinkage process of the Voronoi cells. The artificial microstructures are, a priori, generated in a periodic manner and, therefore, possible boundary layer effects during computational homogenization are minimized. The SVEs are considered to be statistically similar to the real structure and serve as its best possible representation. Besides*

---

<sup>1</sup>This chapter is published in *Construction and Building Materials* [75] and a preliminary study in *Proceedings in Applied Mathematics and Mechanics* [74].

*the SVE generation, this chapter focuses on the constitutive description of the bituminous binding agent, which we interpret as a viscoelastic fluid. In our analysis of the results we concentrate on the upscaling properties of morphological and material nonlinearities.*

## 6.1 Introduction

Asphalt concrete is a complex multi-component material widely used for road construction purposes. Its overall mechanical behavior strongly depends on the particular constituents, their individual behavior and their spatial distribution. The typical asphalt compound consists of three major constituents, namely stiff mineral aggregates, a soft viscoelastic binding agent and air-voids [34,89]. Depending on the volume fractions of the constituents, the type of particular constituents and the binding agent, material properties for a wide range of applications can be adjusted in a heuristic manner. Moreover, asphalt concrete represents a multi-scale material, see Figure 6.1. From the observer's point of view (length scale  $L$ ), asphalt concrete can be described as a homogeneous medium with effective material properties. Zooming in, we arrive at the heterogeneous micro-scale (length-scale  $l$ ) consisting of mineral aggregates, mastic and, possibly, pores. The mastic itself may represent a mixture of the Bitumen phase and very small aggregates  $d_{eq} \leq 63 \mu\text{m}$ . Typically, morphologies with particle sizes  $1 \text{ mm} \leq d_{eq} \leq 8 \text{ mm}$  can be reliably resolved by the X-Ray Computed Tomography (XRCT) technique with resolution on the micrometer-level. Hereby, the Particle Size Distribution (PSD) is expressed in terms of the diameter of volume equivalent spheres

$$d_{eq} = \sqrt[3]{\frac{6 V_{3D}}{\pi}}, \quad (6.1)$$

with the particle volume  $V_{3D}$  extracted from the XRCT data.

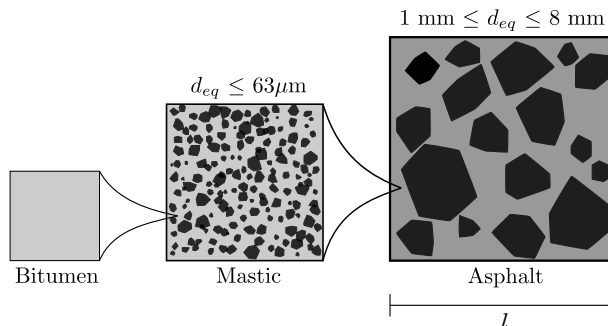


Figure 6.1: Different scales for asphalt concrete.

It is an ongoing research field to understand the highly complex interactions between the microscopic processes and the prevalent material properties of asphalt concrete on

the large scale for these strongly heterogeneous materials. Hence, numerical modeling approaches are valuable tools for this analysis.

In order to describe the microscopic processes under external loading, detailed information about two things is required. First, the material properties of the microscopic constituents and second, the morphology of the composite that represents the spatial arrangement of the constituents. Hereby, the morphology of the mineral aggregates that is, amongst others, their volume fraction, the grading curve as well as their PSD, is of particular interest. Thus, it is necessary to gain knowledge about these properties to create the best possible data basis for numerical simulations. In our study, this morphological knowledge is gained by a physical specimen which is scanned by XRCT. The 3-dim analysis software Avizo Fire (FEI Visualization Sciences Group, Version 9) gives us the opportunity to extract the morphological properties from the reconstructed volume, since some of them are not known from the production process itself. In the upcoming sections, we propose a workflow from the raw XRCT data towards statistically similar unit cells used for the computational homogenization process of the overall material properties of the compound. For this purpose, this chapter combines scientific approaches from different disciplines. We, therefore, want to give an overview on the current research in these fields and to review the findings shortly. Finite Element (FE) simulations on data gained from XRCT is a research field investigated by various groups in different areas, such as material sciences and engineering with particular regard to the image acquisition of asphalt concrete and the quantitative analysis of the microstructure to determine phase volumetric relationships and aggregate characteristics. Onifade et al. [59] studied the micro-mechanical results and displayed the load transfer chains and stress localizations between neighboring particles. You et al. [93] investigated a large biphasic example by ignoring air-voids. They introduced the mastic as a thermo-viscoelastic, thermo-viscoplastic and thermo-viscodamage material. The mineral aggregates are modeled as a linear elastic material. Coleri and coworkers carried out a prediction of the asphalt concrete shear modulus [7]. They developed 2- and 3-dim micromechanical FE models with elastic and viscoelastic constitutive behavior for the constituents. Two different asphalt mixtures were investigated with a shear frequency sweep at constant height. They found a very good accuracy for the 3-dim example. Further, they showed an interesting comparison between the virtual image of the mineral aggregates and the real structure.

Since, however, numerical simulations based on XRCT scans using triangulated surfaces are highly expensive in terms of CPU-time and the flexibility for the creation of several different microstructures is not given [93], we now want to focus on literature which is concerned with the creation of artificial microstructures. These artificial microstructures have the advantage that a large amount of microstructures can be created and investigated in a short time frame. Tehrani and coworkers introduced a custom numerical toolbox [83] that is a random object modeler, to generate random inclusions of various sizes and shapes to derive the aggregate skeleton. The asphalt concrete is modeled as a biphasic medium with linear viscoelastic behavior for the

bituminous binding agent. Results in terms of complex moduli and phase angles and also localized stress and strain distributions are studied. The calculations are carried out in 2-dim but cut out from 3-dim microstructures. In another work of Tehrani et al. [82], the results for linear viscoelastic simulations in 3-dim with only spherical inclusions are shown. However, geometrical as well as material linearity is a very strong assumption for such heterogeneous media with strongly diverging material properties as the asphalt constituents. The Discrete Particle Method plays a role in the simulation of asphalt concrete as well, as can be seen in the work of Ormel et al. [60] and Magnanimo et al. [52].

The generation of artificial microstructures using Voronoi tessellations or Voronoi diagrams is a well-established technique for modeling of crystalline structures and reinforced composites [17, 18, 90] as well as for concrete models using a random structure of spherical aggregates [21, 92]. However, it is not possible to control a PSD by the standard Voronoi tessellation. To remedy this deficiency, Lavergne and coworkers [46] proposed to generate microstructures with pre-defined PSD and grain shapes using dense sphere packing and power diagrams [3, 4] for polycrystals. They, therefore, combine the weighted Voronoi tessellations with the simulation of a Particle Dynamics approach. The used algorithm for the polydisperse sphere packing is the Lubachevsky-Stillinger algorithm [49]. In the present chapter, we extend this approach towards asphalt concrete, where the volume fraction of solid mineral aggregates is significantly smaller than 1, as it is the case for polycrystals. As the basis for our PSD we make use of a XRCT data set.

Besides the morphology on the micro-level it is important to investigate the material properties of the particular constituents with special regard to the bituminous binding agent, generally understood as a viscoelastic material. Concerning the rheological models for the bituminous binding agent, a wide range of research activities are to be found in literature. We would like to refer to the extensive literature review for the mechanical modeling of the linear viscoelastic rheological properties of the bituminous binding agent by Yusoff and coworkers [94] including the master curve procedure and the time-temperature superposition principle [14] that we apply in section 6.3. Furthermore, fractional models [81] and nonlinear viscoelastic rheological models [31, 70], to name only a few, are to be found in literature. In the present chapter we refer to the generalized Maxwell-Zener approach extended to a 3-dim continuum formulation with consideration of geometrical nonlinearities [30, 80].

Having all material properties of the viscoelastic compound on the micro-scale at hand, we derive the macroscopic response of the mixture to an external loading by a computational homogenization approach based on volume averaging techniques. Assuming separation of scales  $l \ll L$ , we apply Hill's [28] averaging framework based on a two-scale energy balance, the so-called Hill-Mandel principle of macro-homogeneity, to compute the effective material properties in terms of volume averages of their microscopic counterparts. For this purpose, we have to define a microscopic volume element being representative for the entire structure (Representative Volume Element, RVE). For practical applications, the size of the implemented microscopic volume elements

is limited by the computational power and, therefore, is generally smaller than the true RVE size. These practically used volume elements are called Statistical Volume Elements (SVEs), see [61]. We, therefore, call the SVE-based overall properties *apparent* instead of *effective* (RVE-based). The volume averaging concept allows for the formulation of various boundary conditions on the SVE level. For a comprehensive overview, see [56, 95]. The interaction between SVE size and apparent material properties has been studied, for example, by Kanit and coworkers, see [40]. It has been found that the usage of periodic boundary conditions minimizes boundary layer effects close to the SVE surface due to the external loading conditions. During the last years, the volume averaging framework was successfully interpreted as a numerical upscaling method, see [54, 55], and is widely used in so-called FE<sup>2</sup> approaches, see [15, 43, 72, 76], to name only a few. Whilst microstructural periodicity is hard to apply on real structures, artificially generated microstructures can be designed a priori in a repetitive fashion. The chosen SVE, therefore, represents a periodic unit cell with a stochastic distribution of material properties, see, for example, Schröder and coworkers [71], who proposed to generate statistically similar unit cells by a minimization process.

The chapter itself is organized as follows: In section 6.2, we describe the different steps of our algorithm to generate artificial SVEs. The XRCT data processing is presented, where we start with filtering and phase segmentation of the raw XRCT data and continue with the PSD. Finally, we describe the workflow for the generation of SVEs on the basis of the gained PSD. Therefore, we introduce the tools of dense sphere packing and the weighted Voronoi tessellation. In section 6.3 we introduce the material properties for the mineral aggregates and the viscoelastic behavior of the bituminous binding agent. Most of the attention goes to the bituminous binding agent, whose properties are characterized by rheological shear experiments using a Dynamic Shear Rheometer (DSR). In addition, section 6.3 describes the computational homogenization process and the results of the numerical studies on the micro- and macro-scale. Finally, the results are analyzed, discussed and we give an outlook on future investigations.

## 6.2 Material and methods

This section provides informations on two main aspects of our work: First, the XRCT data handling and how we reach the goal of a proper phase segmentation. Second, the generation of artificial microstructures is discussed in detail. Particular attention is paid to the algorithmic steps which lead from the identification of the relevant microstructural parameters towards the resulting set of artificial SVEs.

### 6.2.1 XRCT data processing

The specimen under investigation is a German standard open porous asphalt (PA8) with 8 mm maximum diameter for the mineral aggregates. The initial XRCT raw data is plotted in Figure 6.2 representing a cylindrical asphalt concrete specimen.

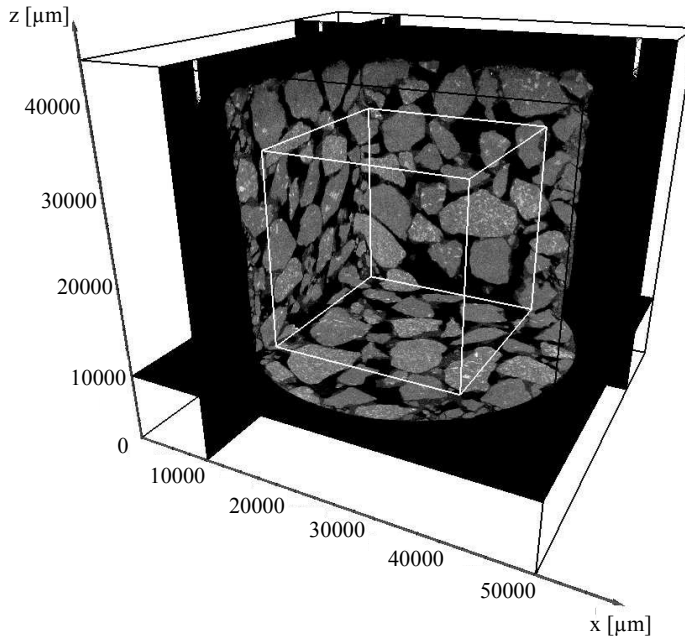


Figure 6.2: Raw data from the XRCT. Illustration in 3-dim in terms of orthogonal slices. Each voxel has a resolution of  $24.5 \mu\text{m}$ . The white cubic frame ( $1000^3$  voxels  $\hat{=} (24.5 \text{ mm})^3$ ) indicates the control volume for further analysis.

The grayscale values in the figure reflect the X-Ray absorption of the constituents in the specimen. Three different phases are present in the sample reconstruction. Taking a closer look at Figure 6.2 one could observe that the light phase which is the particle/aggregate phase, includes white spots. These spots are mineral deposits incorporated into the aggregate phase. For simplicity reasons, however, we consider the mineral aggregates to be homogeneous throughout our study.

The typical workflow for XRCT data processing is filtering of the data, setting thresholds for each phase and an analysis with respect to the desired structural properties. This allows us to segment the data into the individual constituents.

The XRCT data used in this chapter is provided by the Bundesanstalt für Materialforschung und -prüfung (BAM) and was produced by a microfocus X-Ray source, with maximum 225 kV, maximum 200 W and a focal spot size of  $6 \mu\text{m}$ . The scintillator material is sodium iodide (NaI). The measurement parameters for the present scan were 140 kV and  $160 \mu\text{A}$ . 2400 angles (slides/radiographs) on  $360^\circ$  were carried out with an integration time of  $10 \times 2$  seconds per angle.

To divide the raw image into the phases of interest, filtering of the raw images is inevitable. Three different materials can be defined in the specimen, mineral aggregates, bituminous binding agent with its filler and air voids. The main goal of the

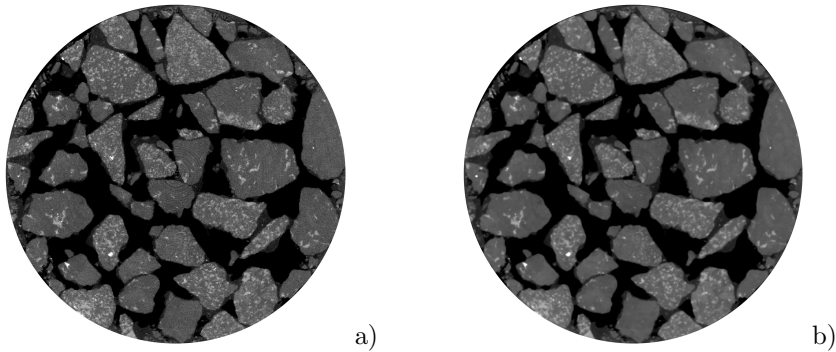


Figure 6.3: 2-dim slices before a) and after b) applying the non-local means filter.

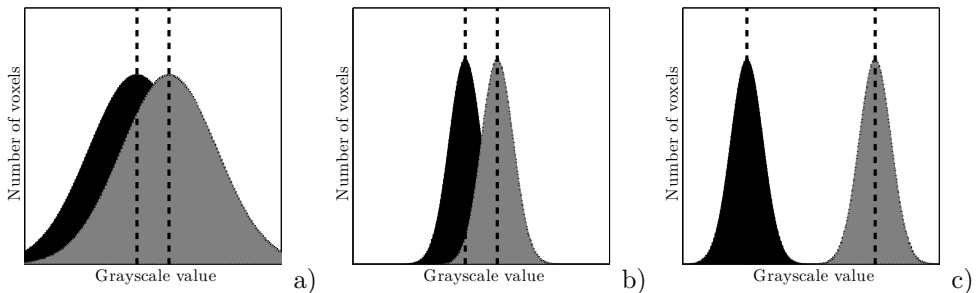


Figure 6.4: Visualisation of a) large intra-class variance, b) small inter-class variance and c) small intra-class variance in combination with a large inter-class variance.

filtering process is to facilitate the phase segmentation. Since the available XRCT reconstruction has, per se, a very good quality and the phases are clearly visible, the only filtering step that we apply is the non-local means filter, cf. 6.3.

This filter mainly denoises the image and clears the gray scale histogram for the segmentation process. The threshold value for each phase is set on the basis of this cleared histogram. Figure 6.4 shows the different variances for the interpretation of a histogram. The schematic example in c) shows the desired conditions for phase segmentation. It shows two phases with small intra-class variance and large inter-class variance.

Even though we are only interested in the PSD of the mineral aggregates and their volume fraction, we want to show, that a phase segmentation for all three phases is possible. Figure 6.5 shows the normalized histogram of the present asphalt concrete specimen a) before and b) after applying the non-local means filter. The number of voxels are normalized with regard to the occurring maximum. A low grayscale value, which means low absorption, represents a dark color, a high value represents a bright color.

Figure 6.6 shows the segmented data and visualizes the different constituents. In Figure 6.6 b) and c) it can be seen that the bituminous phase  $\varphi^f$  covers the surface

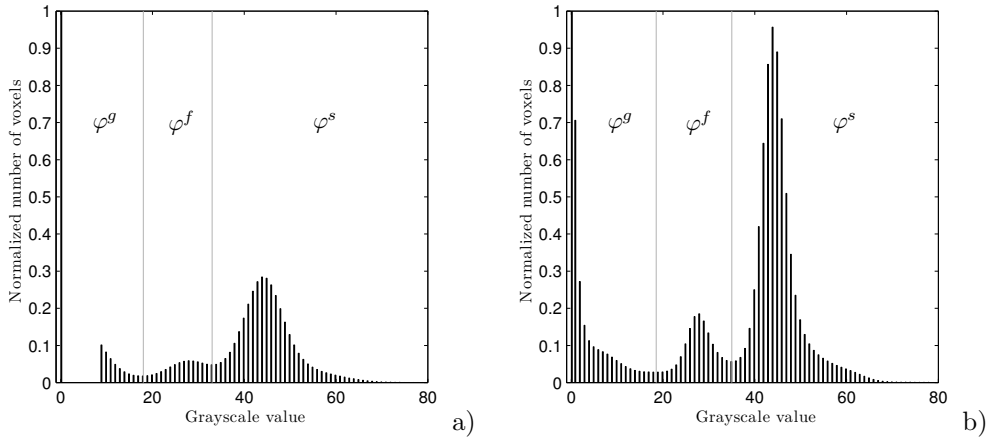


Figure 6.5: Normalized histogram for a three phase asphalt concrete with phases  $\varphi^g$ ,  $\varphi^f$  and  $\varphi^s$  a) before and b) after applying the non-local means filter.

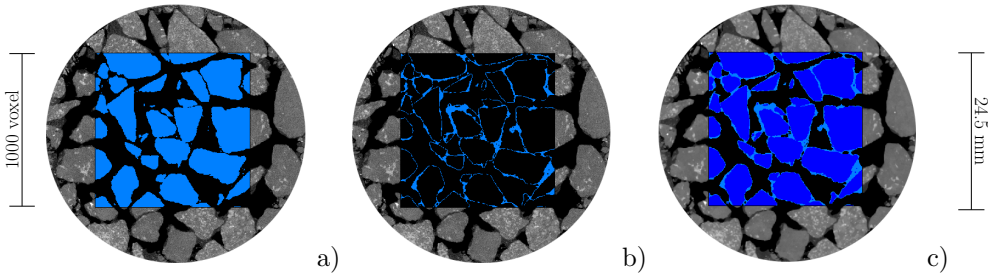


Figure 6.6: 2-dim illustration of the a) mineral aggregates  $\varphi^s$ , b) the bituminous binding agent  $\varphi^f$  and c) a biphase coloration of both. The black phase indicates air  $\varphi^g$ .

of the solid aggregates and forms bridges between neighboring aggregates. Figure 6.7 shows the same sub-figures in a 3-dim rendering of the  $1000^3$  voxel control volume. Once the segmentation is executed, the XRCT scan can be analyzed with respect to the individual phases. For our purposes, the volume fractions of the constituents and the PSD are of major interest. For a better understanding we introduce the volume fractions of the individual phases  $\varphi^\alpha$ ,  $\alpha = \{s, f, g\}$ , as  $n^\alpha = dv^\alpha/dv$  with the volume element of the mixture  $dv$  and the volume element  $dv^\alpha$  occupied by phase  $\varphi^\alpha$ , Figure 6.6 and 6.7. We define the porosity as  $\phi = n^g = 1 - n^s - n^f$ . Accordingly, we introduce the mass fraction  $w^\alpha = dm^\alpha/dm$  with the mass element  $dm = \rho dv$  and  $dm^\alpha = n^\alpha \rho^{\alpha R} dv$ , the density of the mixture  $\rho$  and the effective (true) density  $\rho^{\alpha R} = dm^\alpha/dv^\alpha$  of the individual constituents  $\varphi^\alpha$ . Inside the control volume highlighted in Figure 6.2, the volume fraction of the bituminous binding agent accounts for  $n^f = 0.124$ , air  $n^g = 0.271$  and mineral aggregates  $n^s = 0.605$ . The cumulative PSD for  $\varphi^s$  derived from the XRCT dataset is shown in Figure 6.9 b) and

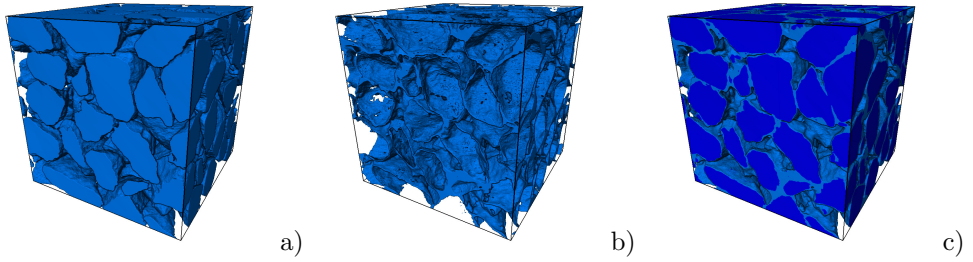


Figure 6.7: 3-dim illustration of the  $1000^3$  voxel cube showing the a) mineral aggregates  $\varphi^s$ , b) the bituminous binding agent  $\varphi^f$  and c) a biphasic coloration of both constituents.

undergoes further analysis in the following sections.

### 6.2.2 Generation of artificial microstructures

After the identification of the relevant microstructural parameters, namely the different volume fractions and the PSD of the mineral aggregates, we now describe the generation of artificial microstructures on the basis of dense sphere packings and Voronoi tessellations. Our aim is to focus on the workflow and the advantages of this procedure compared to a numerical investigation based on XRCT data. In particular the unessential richness of detail of the segmented dataset leads to unacceptably small SVE sizes which are accessible to numerical simulations at reasonable costs. The following arguments underline the advantages of artificial microstructures: First, artificial microstructure generation involves simplified geometries of the mineral aggregates and, therefore, allows for a suitable triangulation of the resulting structure. Second, the artificial generation makes it possible to create manifold microstructures with almost identical statistical properties (PSD, volume fractions  $n^\alpha$ ) and stochastic spatial distributions of the constituents. This gives rise to proper statistical analyses of the overall material properties. Third, the artificial microstructures can, a priori, be created in a spatially periodic manner. Hence, periodic boundary conditions may be applied in the computational homogenization framework. This makes it possible to study reasonably small SVE sizes. Altogether, the usage of artificial, yet statistically similar, microstructures leads to a significant numerical speed-up.

In the sequel, we aim to establish a novel technique for the efficient generation of artificial substitutes for asphalt concrete. For simplicity reasons, we restrict ourselves, so far, on the description of a biphasic asphalt concrete. Hence, the pore space is ignored and is assumed to be filled with the bituminous binding agent phase. Being aware that the proper consideration of the true porosity will influence the effective properties of asphalt concrete significantly, this important problem remains subject to ongoing research. The statistical generation of the biphasic asphalt requires the following workflow which will be discussed in more detail below: First, the PSD is adjusted using the Lubachevsky-Stillinger algorithm. Second, the geometry of the

artificial mineral aggregates is generated by a weighted Voronoi tessellation. Third, we trigger the volume fraction of the mineral aggregates ( $n^s$ ) by an appropriate shrinking process.

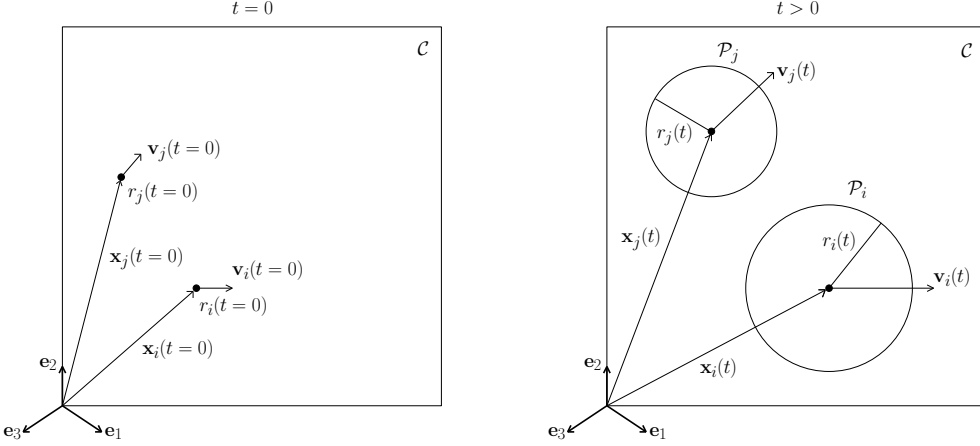


Figure 6.8: Graphical visualization of the Lubachevsky-Stillinger algorithm. The spherical particles  $\mathcal{P}_i$  and  $\mathcal{P}_j$ ,  $i, j = 1, 2, \dots, N$ , move within a unit cube  $\mathcal{C}$ . Their radius is computed as  $r_i(t) = g_i t$  with the individual but constant growth rate  $g_i$ .

The Lubachevsky-Stillinger algorithm [9, 49] represents a discrete particle simulation technique to generate dense sphere packings. To this end, the motion of growing particles and the interaction between the growing particles in terms of elastic collisions is computed. In the initial state ( $t = 0$ ), we generate a set of  $N$  infinitesimal spherical seed points with radius  $r_i(t = 0) = 0$  in an unit cube  $\mathcal{C}$ . We assign a random initial velocity  $\mathbf{v}_i(t = 0)$ , and an individual growth rate  $g_i$ ,  $i = 1, 2, \dots, N$ , to each particle. The particle growth is controlled by the relation  $r_i(t) = g_i t$ . The growth rate  $g_i$  is chosen in accordance to the PSD of the available XRCT data. Once in motion, the spheres might touch or overlap with each other. The time  $t$  at which a collision between the particles  $i$  and  $j$  occurs is calculated as

$$|\mathbf{x}_i - \mathbf{x}_j + (\mathbf{v}_i - \mathbf{v}_j) t| = (r_i + r_j) + (g_i + g_j) t, \quad (6.2)$$

where  $\mathbf{x}_i$  defines the position vector pointing on the volume centroid of the particle  $i$ ,  $i = 1, 2, \dots, N$ , cf. Figure 6.8. Hereby, we have used the vector norm  $|\diamond| = \sqrt{\diamond \cdot \diamond}$ ,  $\diamond$  representing any member of the particular Euclidean vector space  $\mathbb{E}^3$ . Eq. (6.2) leads to the quadratic equation

$$a t^2 + 2 b t + c = 0 \quad (6.3)$$

with

$$a = |\mathbf{v}_i - \mathbf{v}_j|^2 - (g_i + g_j)^2, \quad (6.4)$$

$$b = (\mathbf{x}_i + \mathbf{x}_j) \cdot (\mathbf{v}_i - \mathbf{v}_j) - (r_i + r_j) (g_i + g_j), \quad (6.5)$$

$$c = |\mathbf{x}_i - \mathbf{x}_j|^2 - (r_i + r_j)^2. \quad (6.6)$$

The quadratic equation leads to three different cases [46]. First, it has no solution, the two spheres never collide. Second, it has one single solution, the two spheres get in contact but do not experience an overlap. Third, it has two solutions, the two spheres collide as rigid bodies. The first of these two solutions identifies the first contact of the two spheres. Knowing the velocities and the current masses of the colliding spheres allows for a computation of the updated velocities after the collision and an updated overall scenario until the next collision occurs. It is important to remark that the described algorithm does not aim to satisfy the conservation laws for mass, momentum and energy of the system rather than to perform a sufficiently random distribution of the polydisperse spheres. The growth process stops if the kinetic pressure of the particle system exceeds or if the time step between the collision events falls below a predefined value. The resulting particle system is considered as a dense packing. An example for a polydisperse particle distribution generated by the

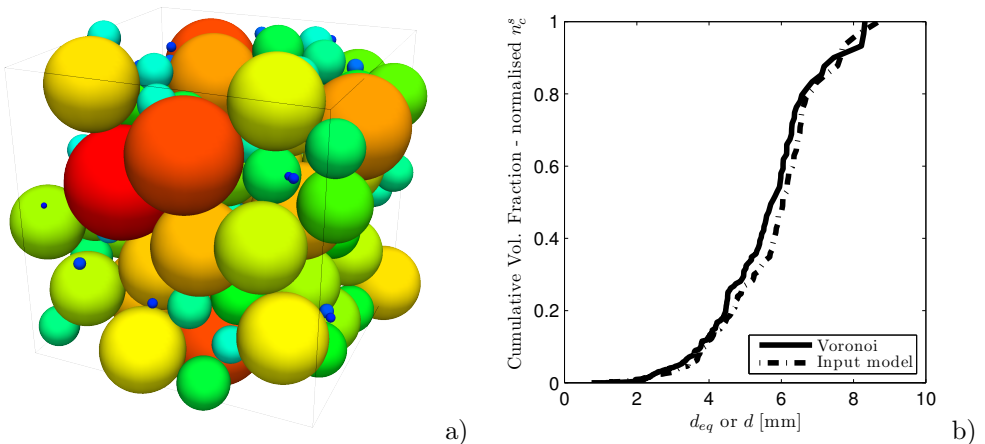


Figure 6.9: a) Final dense sphere packing structure and b) cumulative volume fraction of the dense sphere packing structure (Input model) and the Voronoi tessellation (Voronoi). The results are normalized to the maximum of the volume fraction  $n^s$ .

Lubachevsky-Stillinger algorithm and based on the above mentioned XRCT data is visualized in Figure 6.9 a). Hereby, small particles with  $d_{eq} \leq 1$  mm are, for simplicity reasons, ignored. Figure 6.9 b) shows the cumulative PSD function, where the result of the Lubachevsky-Stillinger algorithm is assigned as the input model. It is important to recall that the resulting PSD is in accordance to the distribution measured in the XRCT data. We classify the mineral aggregate particles with increasing size

$d_{eq}(n_i^s) := 2r_i$  such that

$$n_i^s = \{n_1^s; n_2^s; \dots; n_N^s\} \quad \text{with} \quad d_{eq}(n_1^s) < d_{eq}(n_2^s) < \dots < d_{eq}(n_N^s). \quad (6.7)$$

The normalized cumulative volume fraction  $n_c^s$  is then defined as

$$n_c^s = \frac{1}{n^s} \sum_{i=1}^N n_i^s. \quad (6.8)$$

We want to mention that even though we apply periodicity in the beginning, it is also possible to create the complete microstructure with consideration of a hard wall cube. This would lead to a non-periodic microstructure.

In the next step, the final state of the Lubachevsky-Stillinger algorithm is used to extract the positions and the radii of the  $N$  spheres serving now as the input data for the weighted Voronoi tessellation of the corresponding  $N$  Voronoi cells. Hereby, the basic idea of the Voronoi tessellation is to determine if an arbitrary chosen point with position vector  $\mathbf{y}$  inside the unit cube  $\mathcal{C}$  belongs to the Voronoi cell  $V_i$ . Defining the Euclidian distance between the point with position vector  $\mathbf{y}$  and the position  $\mathbf{x}_i$  of the Voronoi cell  $V_i$  as  $d(\mathbf{y}, \mathbf{x}_i) = |\mathbf{y} - \mathbf{x}_i|$ , we use the radical Voronoi tessellation [67], also known as Power Diagram [3,4] which weights each cell according to the corresponding radius  $r$  resulting from the dense sphere packing,

$$V_i = \{\mathbf{y} \in \mathcal{C} \mid d(\mathbf{y}, \mathbf{x}_i)^2 - r_i^2 \leq d(\mathbf{y}, \mathbf{x}_j)^2 - r_j^2 \quad \forall \quad i \neq j\}, \quad (6.9)$$

$i, j = 1, 2, \dots, N$ . Since we are using a dense sphere model to determine the seed points for the Voronoi tessellation, it is guaranteed that the number of particles before and after the tessellation is identical. By nature, the resulting Voronoi tessellation fills the unit cube completely. Hence, the volume fraction of the mineral aggregates after Voronoi tessellation accounts for  $n^s = 1$ . In the next step, we shrink the Voronoi particles to adjust the required volume fraction  $n^s < 1$  of the mineral aggregates as well as of the volume fraction  $n^f = 1 - n^s$  of the bituminous binding agent.

The shrinking process is established in a random fashion. Hence, neighboring particles in the shrunk configuration possess generally non-planar and, therefore, non-parallel surfaces. The shrinking procedure is executed in due consideration of the periodicity of the SVE. This means, each periodic twin is shrunk in the same manner. To this end, we consider the Voronoi cell  $V_i$  and the position vectors  $\mathbf{c}_k$ ,  $k = 1, 2, \dots, N_c$ , pointing from the local origin  $\mathcal{O}_i$  towards the corner points of the Voronoi cell, see Figure 6.10. We define a shrinking displacement  $s_k$  of the corner position  $\mathbf{c}_k$  as

$$s_k = \gamma_k (u - v) + v \quad \text{with} \quad \{\gamma_k \in \mathbb{R} \mid 0 \leq \gamma_k \leq 1\}. \quad (6.10)$$

Hereby, the parameter  $\gamma_k$  is randomly chosen and, therefore, the shrinking displacement  $s_k$  is bounded by  $v < s_k < u$ . The new local coordinate is then calculated as

$$\mathbf{c}_k^s = \mathbf{c}_k s_k. \quad (6.11)$$

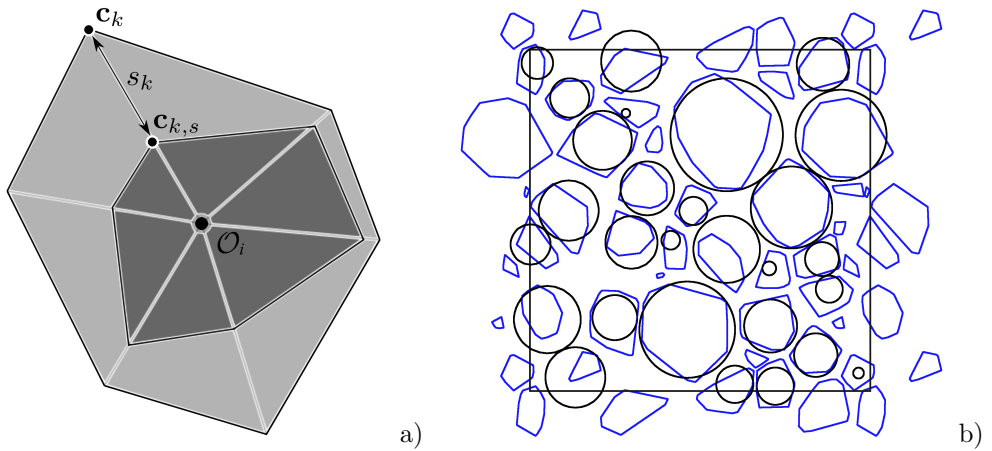


Figure 6.10: a) Illustration of the stochastic shrinking of a corner point  $k$ . The local coordinate  $\mathbf{c}_k$  before and  $\mathbf{c}_k^s$  after the shrinking process is evaluated with respect to the origin  $\mathcal{O}_i$  of the Voronoi cell  $V_i$ ,  $i = 1, 2, \dots, N$ ,  $k = 1, 2, \dots, N_c$ . The randomly chosen parameter  $s_k$  represents the displacement of the corner position  $\mathbf{c}_k$  towards  $\mathcal{O}_i$ . b) Comparison of a 2-dim slice taken from a 3-dim dense sphere packing and the corresponding shrunk Voronoi cells. For some particles, the spheres are outside of the slice and only the shrunk cells are visible.

This means that each corner of the Voronoi cell is shifted within this aforementioned range towards the center of the Voronoi cell. Due to its random character, the shrinking procedure is a priori not self-similar. The choice of the bounding parameters  $u$  and  $v$  is also the leverage point for the control of the volume fraction  $n^f$  of the bituminous binding agent. By setting the range to a higher or lower level, or by reducing the range itself, one is able to stimulate the desired volume fraction of the second phase. Moreover,  $u$  and  $v$  may be chosen in dependence of the equivalent cell size  $d_{\text{eq}}$ . It is possible to define the shrinking range in such a way that the desired volume fraction  $n^f$  is reached, if the values  $u = 0.99$  and  $v = 0.7$  are considered. This leads to a minimum shrinking of 1% and a maximum shrinking of 40% and guarantees that no Voronoi cell stays in contact with another cell. By doing so, a minimum amount of bituminous binding agent is always located between two particles, just as in a physical specimen. Figure 6.10 b) illustrates a 2-dim cut through the unit cube with the densely packed spheres and the Voronoi cells (polygons). The periodicity of the Voronoi cells is clearly visible. Voronoi cells without a complementary circle are either periodic counterparts or are extensions of a cell where the corresponding sphere does not intersect the displayed plane. Once the size and the location of each particle is defined, cutting the particle volumes outside the unit cube, see Figure 6.11, yields the perfectly periodic unit cell required for our further investigations.

In order to validate our microstructure generation scheme we now compare the PSD of the periodic unit cell to that one of the initial XRCT data. It is important to recall

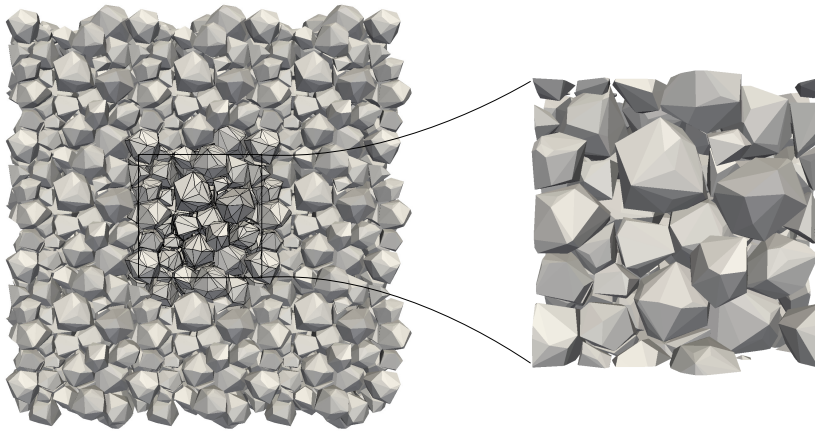


Figure 6.11: Unit cube (right-hand side) with periodic continuation (left-hand side).

first that the PSD of the Lubachevsky-Stillinger algorithm is by definition equivalent to that one observed in the highlighted control volume of the analyzed XRCT data, and, second, that small particles  $d_{eq} \leq 1$  mm are ignored. Hence, the XRCT control volume contains 180 particles. The cumulative volume fraction of the XRCT data and of the Voronoi tessellation is displayed in Figure 6.9 b). Both cumulative curves

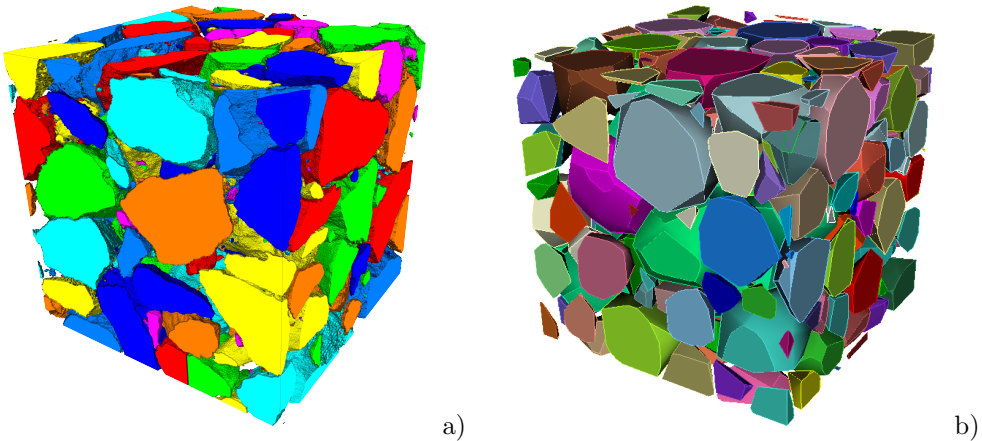


Figure 6.12: a)  $1000^3$  voxel cube from the XRCT scan and b) one random artificial counterpart from the Voronoi tessellation.

show a very good self-similar slope. In Figure 6.12 the artificial microstructure used for the evaluations in Figures 6.9 b) is visualized in comparison to the XRCT control volume.

## 6.3 Nonlinear viscoelastic properties on the effective scale

In this section we aim to apply the previously introduced algorithm to derive the effective viscoelastic material response of asphalt concrete in terms of a computational homogenization concept. Hence, we adapt a viscoelastic material model for the bituminous binding phase in a geometrically nonlinear setting. The overall properties of the compound are computed as volume averages of their microstructural counterparts. Hereby, microscopic quantities are assigned as  $\diamond$ , the macroscopic versions of  $\diamond$  are denoted as  $\bar{\diamond}$ .

### 6.3.1 Micro-scale modeling and homogenization

Due to the complex morphology of open porous asphalt concrete we introduce the following assumptions: First, we assume the voids of the open porous asphalt to be filled with the bituminous binding agent. Hence, we have to investigate a two-phase compound consisting of mineral aggregates  $\varphi^s$  and the bituminous binding agent  $\varphi^f$  ( $n^f + n^s = 1$ ). Second, only mineral aggregates with  $d_{eq} \geq 1$  mm enter the mechanical model in a discrete fashion. The spatial distribution is carried out with the algorithm presented in section 6.2. By contrast, filler particles with  $d_{eq} \leq 63 \mu\text{m}$  are considered to be part of the bituminous binding agent, see Figure 6.1. Thus, the viscoelastic bituminous binding agent itself  $\varphi^f$  is interpreted as a mixture of the pure bitumen  $\varphi^b$  and the smallest filler particles  $\varphi^p$ . Hereby, we use  $m^p/m^f = 0.65$ . In other words, the small filler particles account for 65% of the effective bituminous binding agent's mass. Finally, particle sizes  $63 \mu\text{m} < d_{eq} < 1$  mm are ignored in accordance with the XRCT data. The mineral aggregates are known to be much stiffer than the bituminous binding agent and the characteristic strains observed in the particles are small. Therefore, the aggregates are modeled using a linear-elastic description (Hooke's law) with the bulk modulus  $K^s = 56.2$  GPa and the shear modulus  $G^s = 32.0$  GPa which are typical values for the rock type Diabas [23], commonly used in road construction.

The viscoelastic properties of the material incompressible bituminous binding agent, namely the complex shear modulus  $G^*$  and the loss factor  $\tan \delta$  with phase angle  $\delta$  with

$$G^* = G' + i G'' \quad \text{and} \quad \tan \delta = \frac{G''}{G'} \quad (6.12)$$

are determined with a DSR in predefined temperature ranges  $-20^\circ\text{C} \leq \theta \leq 30^\circ\text{C}$  in intervals of  $10^\circ\text{C}$  and frequency ranges  $0.1 \text{ Hz} \leq f = \omega/(2\pi) \leq 10 \text{ Hz}$ .  $G'$  represents the storage modulus and  $G''$  the loss modulus, respectively. The storage modulus

$$G' = \frac{\tau_0}{\gamma_0} \cos \delta \quad (6.13)$$

is an index for the recoverable energy contribution which means it describes the elastic

part of the deformation. The loss modulus

$$G'' = \frac{\tau_0}{\gamma_0} \sin \delta \quad (6.14)$$

quantifies the viscous energy contribution which is dissipated as heat.  $\tau_0$  and  $\gamma_0$  are the constant initial load and the constant initial deformation, respectively.  $\delta$  is an indicator for the phase shift between the occurring shear stress and shear strain. The bituminous binding agent is considered as a thermo-rheologically simple material [8, 94] and, therefore, we apply the time-temperature superposition principle. By using the time-temperature superposition principle, a master-curve for the DSR results is created. The reference temperature for the master-curve is chosen as  $\theta_{ref} = 20^\circ\text{C}$ .

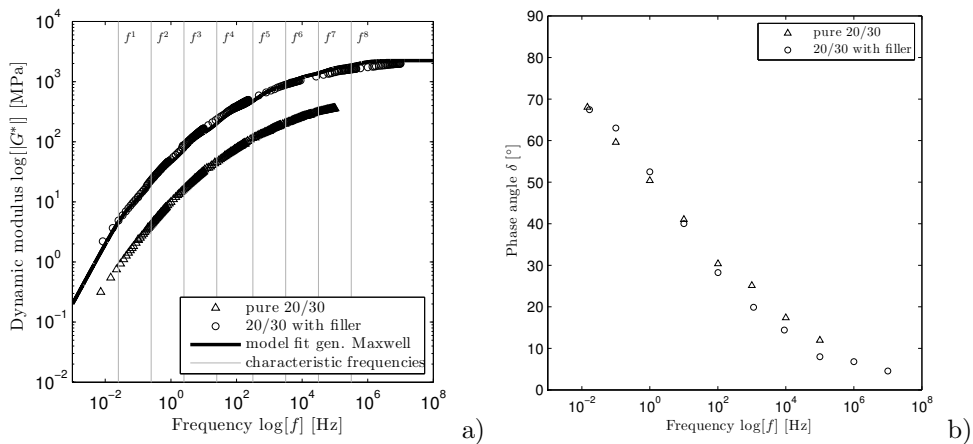


Figure 6.13: a) Experimental DSR results in a logarithmic plot for the dynamic modulus  $|G^*|$  with master-curve (first, non-modified 20/30 bituminous binding agent with  $m^p/m^f = 0.65$  and, second,  $m^p/m^f = 0.0$ ). The characteristic frequencies  $f^i$  for the generalized Maxwell-Zener model are indicated by the vertical lines. b) Phase angle.

The viscoelastic behavior of the bituminous binding agent is modeled with a generalized Maxwell-Zener approach. To account for the behavior of the loss and storage modulus, we used the equation for the dynamic modulus  $|G^*|$  to fit the parameters. The results of the model-fit are listed in Table 6.1. We found eight Maxwell-chains,  $i = 1, 2, \dots, 8$ , to be sufficient to describe the material behavior in the desired frequency range. This is in accordance to approximately one Maxwell-chain per decade. The dynamic viscosity for the single Maxwell-Chains is introduced as  $\eta_i$ ,  $T^i$  is the characteristic relaxation time of a single chain and  $f^i = \omega^i/(2\pi)$  its characteristic frequency. The dependency is  $\omega^i = G^i/\eta^i = 1/T^i$ . Figure 6.13 a) compares the master-curves of the mastic (bituminous binding agent including the small filler particles) and of the pure 20/30 penetration grade bituminous binding agent. Their slope in the double logarithmic scale at low frequencies is an indicator for a fluid like

behavior [14]. Figure 6.13 b) strengthens this assumption since the phase angle tends towards  $\pi/2 = 90^\circ$  at low frequencies,  $\lim_{\omega \rightarrow 0} \delta = 90^\circ$ . Based on these findings, we model the behavior of the bituminous binding agent in the generalized Maxwell-Zener model, where the purely elastic chain is ignored.

### 6.3.2 3-dim nonlinear viscoelastic modeling approach

In this section we want to give a brief overview of the modeling approach for nonlinear viscoelasticity in 3-dim in the context of microscopic simulations. Using the experimental data we are able to prescribe the scale transition rules for replacing the heterogeneous viscoelastic micro-scale by a homogeneous macroscopic substitute. We, therefore, impose that macroscopic quantities are computed as volume averages of their microscopic counterparts. We write  $\bar{\diamond} = \langle \diamond \rangle_{\square} = \frac{1}{V_{\square}} \int_{V_{\square}} \diamond dv$ , with  $V_{\square} = \int_{V_{\square}} dv$  being the volume of the chosen microscopic SVE. All details concerning the computational homogenization concept using periodic boundary conditions can be found, for example, in [43].

For the purpose of the nonlinear description at this point, we introduce the tangent map  $\mathbf{F} = \partial \mathbf{x} / \partial \mathbf{X} = \text{Grad } \mathbf{x} = \text{Grad } \mathbf{u} + \mathbf{I}$ . Here,  $\mathbf{X}$  is the position vector of a material point of the mixture in the undeformed (reference) configuration,  $\mathbf{x}$  the position vector in the deformed (current) configuration and  $\mathbf{u}$  the displacement vector. We execute, for each chain  $i = 1, 2, \dots, 8$ , of the above identified generalized Maxwell-Zener model, the multiplicative split of the deformation gradient into an elastic part  $\mathbf{F}_e^i$  and an inelastic or viscous part  $\mathbf{F}_v^i$ , see [45, 47, 48], and write  $\mathbf{F} = \mathbf{F}_e^i \cdot \mathbf{F}_v^i$ . Moreover, we introduce in the usual way the right Cauchy-Green deformation tensor  $\mathbf{C} = \mathbf{F}^T \cdot \mathbf{F}$  as a measure of the reference configuration  $\mathcal{B}_0$  and the left Cauchy-Green deformation tensor  $\mathbf{B} = \mathbf{F} \cdot \mathbf{F}^T$  as a quantity of the current configuration  $\mathcal{B}$ . This allows to introduce the viscous part of the right Cauchy-Green deformation tensor  $\mathbf{C}_v^i = (\mathbf{F}_v^i)^T \cdot \mathbf{F}_v^i$  and the elastic part of the left Cauchy-Green deformation tensor  $\mathbf{B}_e^i = \mathbf{F}_e^i \cdot (\mathbf{F}_e^i)^T$ . For more details we refer exemplarily to standard textbooks [25, 30]. The tensors  $\mathbf{C}_v^i, i = 1, 2, \dots, 8$ , are interpreted as internal variables of the viscoelastic model described by an evolution equation. For further use we introduce the displacement gradient with respect to the reference configuration  $\mathbf{H} = \text{Grad } \mathbf{u}$  and the Green-Lagrange strain tensor  $\mathbf{E} = \frac{1}{2} (\mathbf{C} - \mathbf{I})$ . Given an appropriate strain energy density function  $W$ , the Cauchy stress tensor is computed as

$$\mathbf{T} = 2 \frac{1}{J} \mathbf{B} \cdot \frac{\partial W}{\partial \mathbf{B}}, \quad (6.15)$$

with the Jacobian  $J = \det \mathbf{F}$ . Even though the applied macroscopic strains are small, we expect that the microscopic strain field may localize, in particular between neighboring particles. In other words, we expect locally large, i.e. finite strains. To take this fact into account, the springs in the generalized Maxwell-Zener model are modeled in terms of a Neo-Hookean strain energy density function with a volumetric-

deviatoric split

$$W = W_{\text{eq}}(\mathbf{B}) + \sum_{i=1}^8 W_{\text{neq}}(\mathbf{B}_e^i) \quad (6.16)$$

$$= W_{\text{eq}}^{\text{vol}}(\mathbf{B}) + W_{\text{eq}}^{\text{dev}}(\mathbf{B}) + \sum_{i=1}^8 W_{\text{neq}}^{\text{dev},i}(\mathbf{B}_e^i) \quad (6.17)$$

$$= \frac{K^0}{2} (J-1)^2 + \frac{G^0}{2} (I_1 - 3) + \sum_{i=1}^8 \frac{G^i}{2} (I_1 - 3). \quad (6.18)$$

Hereby,  $G^0$  and  $G^i$  are the shear moduli of the springs and  $K^0$  is the bulk modulus. The volumetric contribution  $W_{\text{eq}}^{\text{vol}}(\mathbf{B})$  is introduced in the sense of a weak compressible material, mainly for numerical reasons [30]. Moreover,  $I_1 = \lambda_1 + \lambda_2 + \lambda_3$  is the first strain invariant and  $J^2 = \lambda_1 \lambda_2 \lambda_3$ . With the Cauchy stress defined as

$$\mathbf{T} = \mathbf{T}_{\text{eq}}^{\text{vol}} + \mathbf{T}_{\text{eq}}^{\text{dev}} + \sum_{i=1}^8 \mathbf{T}_{\text{neq}}^{\text{dev},i} \quad (6.19)$$

$$= 2 \frac{1}{J} \left( \mathbf{B} \cdot \frac{\partial W_{\text{eq}}^{\text{vol}}}{\partial \mathbf{B}} + \mathbf{B} \cdot \frac{\partial W_{\text{eq}}^{\text{dev}}}{\partial \mathbf{B}} + \sum_{i=1}^8 \mathbf{B}_e^i \cdot \frac{\partial W_{\text{neq}}^{\text{dev},i}}{\partial \mathbf{B}_e^i} \right) \quad (6.20)$$

and the given strain energy density function, the constitutive equation reads

$$\mathbf{T} = K^0 (J-1) \mathbf{I} + \frac{1}{J} G^0 \mathbf{B}^0 + \sum_{i=1}^8 \frac{1}{J} G^i \mathbf{B}_e^i. \quad (6.21)$$

It is important to remark that the DSR experiments for the bituminous binding agent resulted in a viscoelastic fluid. Hence, the equilibrium part of the stress tensor ( $\mathbf{T}_{\text{eq}}$ ) has no deviatoric contribution ( $G^0 \approx 0$  MPa), and the constitutive equation in its final version states

$$\mathbf{T} = K^0 (J-1) \mathbf{I} + \sum_{i=1}^8 \frac{1}{J} G^i \mathbf{B}_e^i. \quad (6.22)$$

Given this constitutive relation, it remains to define the viscoelastic equation system to be solved for the micro-scale. The evolution of the before mentioned internal variables is described in terms of an evolution equation of the form

$$\frac{d}{dt} (\mathbf{C}_v^i) = \dot{\mathbf{C}}_v^i = \frac{2}{JT_i} \left[ \mathbf{C} - \frac{1}{3} \text{tr} \left( \mathbf{C} \cdot (\mathbf{C}_v^i)^{-1} \right) \mathbf{C}_v^i \right], \quad (6.23)$$

cf. [25]. Here,  $\dot{\mathbf{C}}_v^i = d\mathbf{C}_v^i/dt$  is the material time derivative. As shown in [79], this evolution equation can be solved in a fully implicit manner without any Newton-Raphson iteration and is, therefore, accessible to the classical Euler-backward method. The viscoelastic equation system is completed by the quasi-static balance of linear momentum  $\text{div } \mathbf{T} = \mathbf{0}$  accounting for periodic boundary conditions  $[\mathbf{u}] = \bar{\mathbf{H}} \cdot [\mathbf{x}]$  and

$\mathbf{t}^+ + \mathbf{t}^- = \mathbf{0}$ . Hereby, we follow [37] and split the boundary  $\partial V$  into an image part  $\partial V_{\square}^+$  and a mirror part  $\partial V_{\square}^-$ . The jump operator is defined as  $\llbracket \diamond \rrbracket (\mathbf{x}) = \diamond(\mathbf{x}^+) - \diamond(\mathbf{x}^-)$ . For the numerical implementation, we transform the balance of linear momentum into its weak representation, accounting for the above mentioned kinematic boundary conditions. Hence, we seek solutions in the trial space  $\mathbb{U}_{\square}$  of admissible displacements that are sufficiently regular in  $V_{\square}$ . We, furthermore, introduce the corresponding trial space of self-equilibrated fluxes  $\mathbb{T}_{\square}$  that are sufficiently regular on the image boundary  $\partial V_{\square}^+$ . We write the equations for finding  $\mathbf{u}, \mathbf{t} \in \mathbb{U}_{\square} \times \mathbb{T}_{\square}$  in an updated Lagrange approach as

$$\langle \mathbf{T} : \text{grad } \delta \mathbf{u} \rangle_{\square} - \frac{1}{V_{\square}} \int_{\partial V_{\square}^+} \mathbf{t} \cdot \llbracket \delta \mathbf{u} \rrbracket da = 0, \quad (6.24)$$

$$-\frac{1}{V_{\square}} \int_{\partial V_{\square}^+} \delta \mathbf{t} \cdot \llbracket \mathbf{u} \rrbracket da = - \left[ \frac{1}{V_{\square}} \int_{\partial V_{\square}^+} \delta \mathbf{t} \otimes \llbracket \mathbf{x} \rrbracket da \right] : \bar{\mathbf{H}}, \quad (6.25)$$

with  $\mathbf{t} = \mathbf{T} \cdot \mathbf{n}$  which hold for any admissible test functions  $\delta \mathbf{u}, \delta \mathbf{t} \in \mathbb{U}_{\square} \times \mathbb{T}_{\square}$ . Hereby, the differential operators  $\text{div}(\diamond)$  and  $\text{grad}(\diamond)$  refer to spatial derivatives with respect to the current position vector  $\mathbf{x}$ . It is important to remark that Eq. (6.24) represents Hill's macro-homogeneity condition for the computational homogenization of a heterogeneous Cauchy continuum towards a homogeneous substitute model. The macroscopic stress response is computed as

$$\bar{\mathbf{T}} = \langle \mathbf{T} \rangle_{\square} = \frac{1}{V_{\square}} \int_{\partial V_{\square}^+} (\mathbf{t} \otimes \mathbf{x})^{\text{sym}} da. \quad (6.26)$$

Although the experimental results which are the basis for the parameter fitting are carried out in a geometrically linear regime, we extrapolate the extracted linear model towards a viscoelastic model at moderate geometrical nonlinearities. Hence, the parameters listed in Table 6.1 are assumed to remain valid for the nonlinear material model. To satisfy the earlier mentioned incompressibility of the bituminous binding agent, the global bulk modulus  $K^0$  is chosen much larger than the sum of all shear moduli  $G^i$ . This leads to a weak compressibility corresponding to a Poisson's ratio of  $\nu \approx 0.48$  at small deformations.

### 6.3.3 Influence of the macroscopic loading velocity, and fluid-like properties of the mastic

In this subsection we want to address the effect that the prescribed macroscopic strain velocity strongly influences the apparent macroscopic properties of the material under investigation. To this end, we study a homogeneous viscoelastic medium (no solid aggregates,  $n^f = 1$ ) which is modeled in accordance to the above identified material properties of the bituminous binding agent, see Table 6.1. Figure 6.14 shows

Table 6.1: Experimentally determined parameters of the generalized Maxwell-Zener model with consideration of  $G^0 \approx 0$  MPa.

	$i = 1$	$i = 2$	$i = 3$	$i = 4$	$i = 5$	$i = 6$	$i = 7$	$i = 8$
$G^i$ [MPa]	3.15E+0	1.32E+1	4.42E+1	1.05E+2	2.09E+2	2.54E+2	2.65E+2	2.28E+2
$T^i$ [s]	3.98E+1	3.98E+0	3.98E-1	3.98E-2	3.20E-3	3.16E-4	3.16E-5	3.16E-6
$f^i$ [Hz]	2.51E-2	2.51E-1	2.51E+0	2.51E+1	3.16E+2	3.16E+3	3.16E+4	3.16E+5

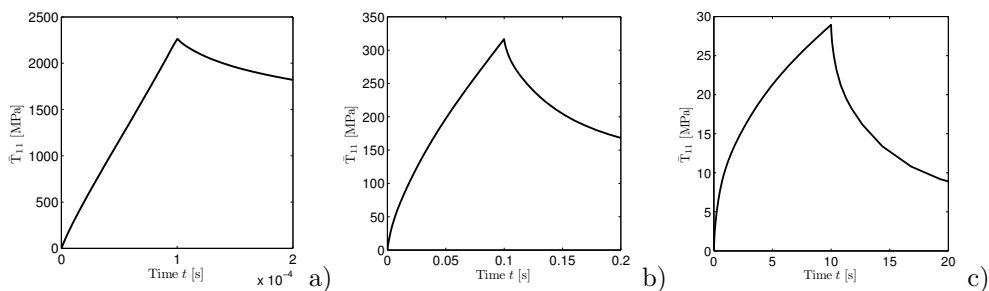


Figure 6.14: Three different states for the stress relaxations. The loading times range from  $t^* = 1\text{E-}4\text{s}$  over  $t^* = 1\text{E-}1\text{s}$  to  $t^* = 1\text{E+}1\text{s}$ . The applied stretch is always  $\bar{\lambda}_1 = 2.0$ .

stress relaxation curves for three different loading velocities in an uniaxial tension test. The applied maximum stretch  $\bar{\lambda}_1 = \frac{L}{L_0}$  is chosen as  $\bar{\lambda}_1 = 2.0$  and is reached after a)  $t^* = 1\text{E-}4\text{s}$ , b)  $t^* = 1\text{E-}1\text{s}$  and c)  $t^* = 1\text{E+}1\text{s}$ . Since we have included a large variety of individual relaxation times  $T^i$ ,  $i = 1, 2, \dots, 8$ , in our underlying generalized Maxwell-Zener model, we get strongly deviating results for the different loading velocities. For a), the peak stress accounts for 2.25 GPa, whereas the peak stress in c) reaches 28 MPa. Moreover, the varying slope during the loading process brings to the fore that, in particular for the slow loading process in c), the 7 fastest dashpots become active already during the loading process. Hence, they can not contribute to the overall stress relaxation which is, consequently, driven by the slow relaxation time  $T^1$ , only, see Table 6.1.

Besides the loading velocity effects, it is important to remark again the fluid-like properties of the mastic (bituminous binding agent including the smallest filler particles). To this end, Figure 6.15 shows stress relaxation curves for the nonlinear model in comparison to the linear model at different maximum stretches and, therewith, the deviation between the nonlinear and the linear model. The normalized value of  $\bar{T}_{11}$  is defined as  $\bar{T}_{11}/(\bar{T}_{11})_{\text{Neo-Hooke}}$  for each applied stretch  $\bar{\lambda}_1$ ,  $\bar{\lambda}_2$  and  $\bar{\lambda}_3$ . Comparing the curves, we observe that, first, the geometrically linear description underestimates

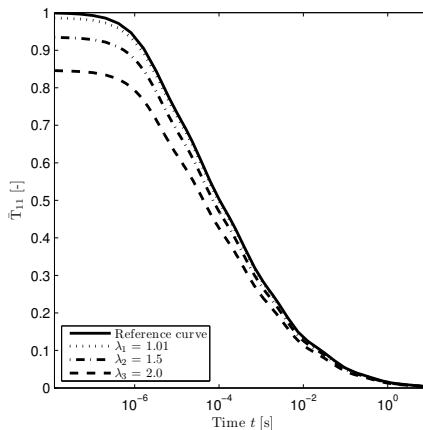


Figure 6.15: Normalized deviation of the stress relaxation curves for three different stretches with respect to the geometrically nonlinear Neo-Hookean result.

the apparent stresses tremendously. Second, the apparent stress tends towards zero at  $t \rightarrow \infty$  which shows the fluid-like behavior of the mastic.

### 6.3.4 Nonlinear effects on the small scale and apparent macroscopic behavior

Finally, we want to apply the above introduced workflow by executing numerical experiments on SVEs with microstructures. The microstructural boundary value problem is solved using the mesh generator Trelis and the Finite-Element package Abaqus. We investigate five different periodic SVE representations, each consisting of 23 statistically generated aggregates according to the proposed algorithm. The volume fraction of the mineral aggregates  $n^s \approx 0.6$  corresponds to that one observed in the XRCT scan. Ignoring voids ( $n^g = 0$ ), the pore space is saturated by the nearly incompressible bituminous binding agent with  $n^f \approx 0.4$ . Typically, the resulting meshes consist of approximately 4 Mio. linear tetrahedral elements with approximately 2 Mio. degrees of freedom. A meshed example of an asphalt concrete unit cube is illustrated in Figure 6.16. This rather high number of degrees of freedom results from the slender bitumen interfaces between neighboring aggregates. All numerical experiments are carried out as stress relaxation tests, where we apply the kinematic loading in terms of the smooth step function, see Figure 6.17 a), with  $t^* = 1\text{E-}3\text{s}$ . Hence, all identified relaxation times are active during the stress relaxation test, see Table 6.1.

The results for uniaxial kinematic boundary conditions applied on the selected five SVEs are shown in Figure 6.17 b). We observe that the individual stress relaxation curves scatter significantly from peak stress perspective. Hence, the apparent behavior of the asphalt concrete on the effective scale varies strongly, even though the SVEs

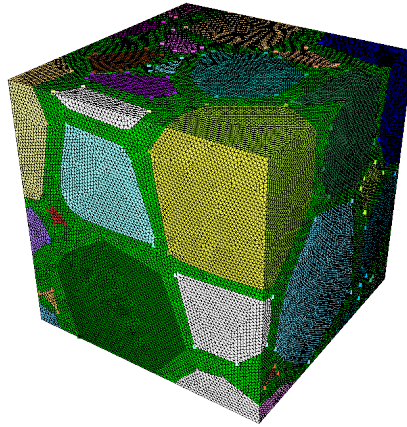


Figure 6.16: Example mesh with approximately 2 Mio. degrees of freedom.

are generated by identical input parameters. This scattering brings to the fore the importance of the individual location and orientation of the mineral aggregates. In Figure 6.18, the strain localization inside the asphalt concrete cube is highlighted. Hereby, we observe moderately nonlinear local deformations even though the overall deformation accounts for  $\bar{H}_{11} = -0.02$ , only. Hence, the geometrically linear description used for the macroscopic loading is inappropriate for the description of the local deformation processes. Similar effects are to be observed under shear or further tensile kinematic loading conditions, see Figure 6.19.

Figure 6.19 shows the von Mises stress results  $\bar{T}_v$  for further kinematic boundary conditions applied on the stochastically generated five SVEs. Again, the effective strain is applied in terms of a smooth step function, cf. Figure 6.17 a). Hereby, we observe that some stress relaxation curves are crossing each others. From a physical view-point this underlines the strong coupling of the local and the global relaxation processes. It is, moreover, important to remark that the apparent properties are slightly anisotropic. The source of this anisotropy lies in the stochastic generation process of the still rather small SVEs. This indicates that, as expected, the chosen SVEs can not be considered as RVEs.

Figure 6.20 shows the von Mises stress  $\bar{T}_v$  for an example SVE under simple shear boundary conditions. The smooth step strain is set to  $t^* = 1E-3s$  and  $t^* = 1E-6s$ . The von Mises stress  $\bar{T}_v$  is normalized to its relaxed value at  $t = 4E+2s$ . Figure 6.20 illustrates two interesting findings. First, the effect of the loading velocity condition as already illustrated and described in Figure 6.14 for the homogeneous bituminous binding agent. The before mentioned difference in the peak stress at  $t = t^*$  is significant and not negligible when discussing effective or apparent behavior of asphalt concrete. The second point we want to discuss are the underlying three different kinematic loading amplitudes for both curves shown in Figure 6.20. The macroscopic strain for the example SVE is set to  $\bar{H}_{12} = 0.01$ ,  $\bar{H}_{12} = 0.001$  and  $\bar{H}_{12} = 0.0001$ .

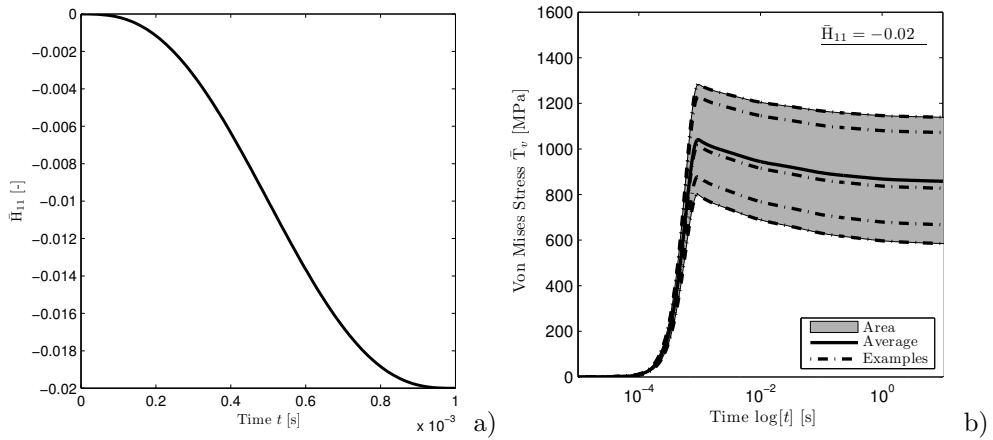


Figure 6.17: a) Strain boundary condition for the uniaxial pressure with a smooth step function. The maximum displacement of  $\bar{H}_{11} = -0.02$  is reached after  $t^* = 1E-3$  s, whilst all further components  $\bar{H}_{ij} = 0$ ,  $i, j = 1, 2, 3$ . b) Relaxation of the von Mises stress  $\bar{T}_v$  for five different examples on the effective scale.

In their normalized version presented in Figure 6.20, all resulting relaxation curves coincide regardless of the loading amplitude. Even though we have a nonlinear behavior on the micro-scale for the larger macroscopic strain boundary conditions, the volume fraction of the highly effected areas are too small to give these heterogeneities enough weight to have an influence on the volume averaged apparent behavior of the compound.

As an outlook we want to refer to Figure 6.21. The Figure shows in a) the difference between the applied macroscopic strain (simple shear) and the observed strain at a manually chosen microscopic integration point from a strongly deformed zone in Figure 6.18. The figure underlines our assumption that the microscopic behavior does not necessarily follow the predefined strain rate on the macro-scale. After  $t^* = 1E-3$  s the macroscopic loading is kept constant, but we still observe an increase in strain on the micro-scale. Hence, the local kinematic reorganization process remain active throughout the entire relaxation of the compound.

## 6.4 Conclusions

In this chapter, the workflow from XRCT scans towards numerical investigations of SVEs for asphalt concrete is described. Hereby, we introduce a novel algorithm to create artificial and simplified microstructures which allow for efficient 3-dim numerical simulations. To this end, we extract essential microstructural parameters from the acquired XRCT data, namely the volume fractions of the particular constituents and the particle size distribution of the mineral aggregate phase. First, we apply a discrete particle dynamics technique to generate dense sphere packings. Second, we use the

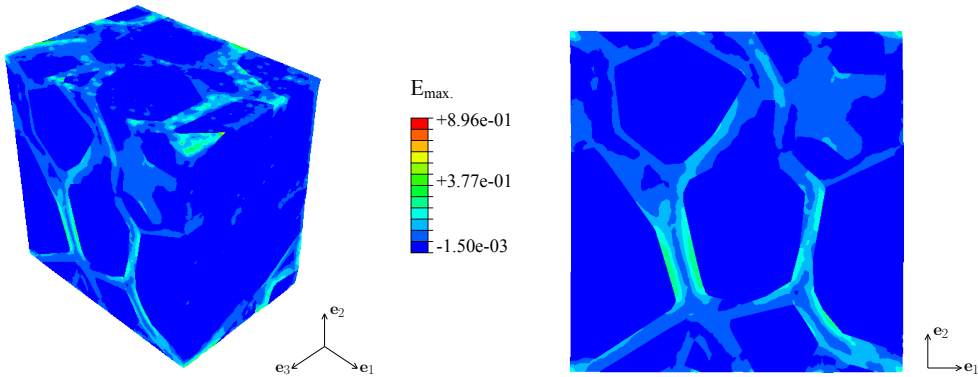


Figure 6.18: Maximum principal strain  $E_{\max.} = \max(E_1, E_2, E_3)$  inside an example SVE under uniaxial pressure  $\bar{H}_{11} = -0.02$ .

center coordinates of the spheres as seed points and define a growth rate proportional to the individual radii of the dense sphere packing. Hence, we have all ingredients at hand to accomplish a weighted Voronoi tessellation. The resulting Voronoi cells are considered as precursor cells for the mineral aggregates. Due to the nature of the Voronoi technique, however, the volume fraction of the cells has to be adapted. Third, we shrink the individual Voronoi cells in a stochastic manner to trigger the correct volume fraction of the mineral aggregates. The volume between the mineral aggregates is filled by the bituminous binding agent. With this generation technique, even nonstandard particle size distributions can be reproduced reliably. Hereby, the predefined particle size distributions may also base on given granulometric curves as used in road construction, cf. Chapter 7. In this case, a XRCT scan is not required. Thus, the presented tool is highly flexible and the resulting artificial and simplified microstructures are accessible to realistic 3-dim simulation scenarios with reasonable numerical efforts. This allows to compare arbitrary combinations of material properties for the bituminous binding agent and the mineral aggregates in a short time range at considerably lower costs compared to physical experiments.

After the generation of appropriate artificial microstructures we assign material properties to the mineral aggregates and to the bituminous binding agent. Whereas we use linear elasticity for the mineral aggregates with material parameters known from literature, we assume moderate but finite deformations for the bituminous phase. Hence, the binding agent is described by a nonlinear generalized Maxwell-Zener model. The required material parameters are gained from physical testings on a Dynamic Shear Rheometer. We successfully execute 3-dim numerical simulations under usage of several artificial microstructures with almost identical volume fractions and particle size distribution but with statistically generated and arranged mineral aggregates. All microstructures undergo stress relaxation tests. We observe that the microstructure's morphology significantly influences the individual relaxation behavior. This effect can be explained by the distinct localization of the viscous activity in the narrow regions

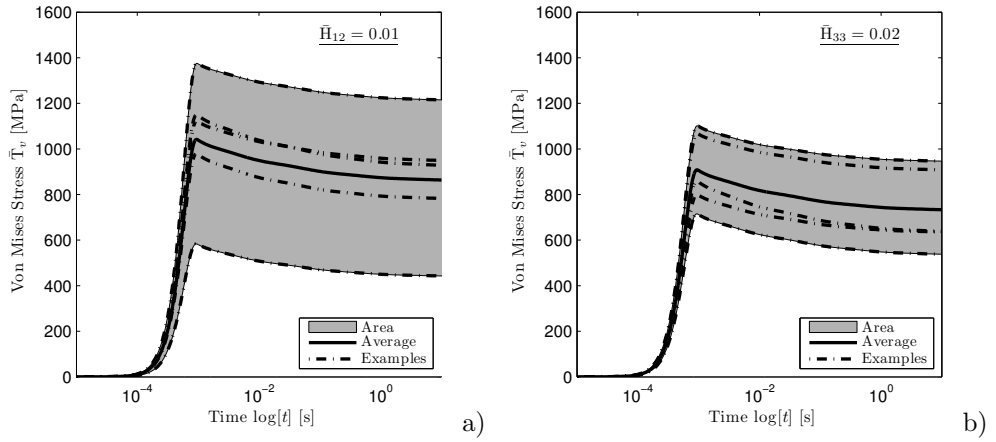


Figure 6.19: a) Stress relaxation for five different examples on the effective scale for simple shear boundary conditions with a smooth step function. The maximum displacement of  $\bar{H}_{12} = 0.01$  is reached after  $t^* = 1E-3$ s. b) Stress relaxation under uniaxial tension  $\bar{H}_{33} = 0.02$ .

between neighboring mineral aggregates which is different for each microstructural representation. However, the nonlinear description is only required at very small volume fractions. Considering the effective material properties as volume averages of their microscopic counterparts over the considered SVE we show that both formulations, linear and nonlinear viscoelasticity, result in identical relaxation curves. Thus, a geometrically linear description on the micro-level seems to be sufficient for small deformations applied on the large scale. Rearrangements of the mineral aggregates during the deformation process are not observed. In other words, the aggregates do not switch their positions. However, such a behavior has to be expected if finite deformations are applied on the macro-level.

After all, it is important to remark that the proposed generation tool is restricted to the description of mastic asphalt concrete. In other words, air voids as presented in Figure 6.6 are, until now, not included and are subject to forthcoming research activities.

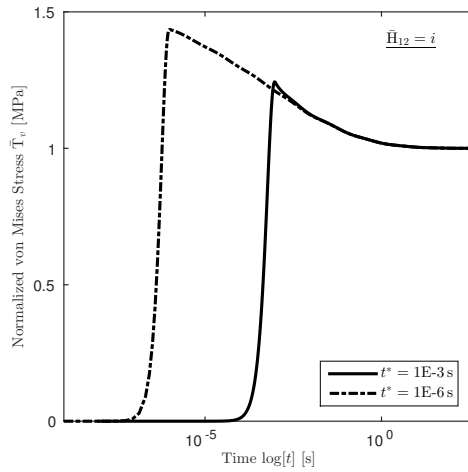


Figure 6.20: Normalized stress relaxation curve for different smooth step loads with  $t^* = 1E-3\text{ s}$  and  $t^* = 1E-6\text{ s}$  for one exemplary SVE. Both curves have an underlying set of three different strain boundary conditions:  $\bar{H}_{12} = 0.01$ ,  $\bar{H}_{12} = 0.001$  and  $\bar{H}_{12} = 0.0001$ .

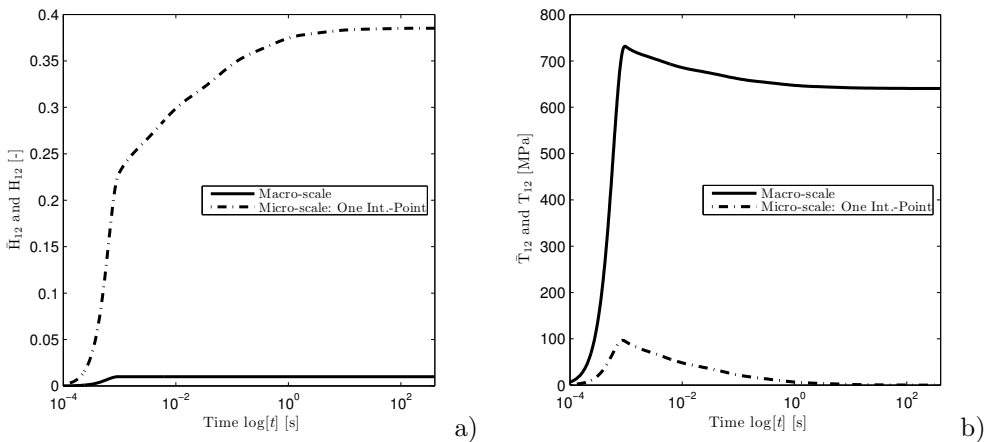


Figure 6.21: a) Difference of strain and b) difference of stress between the effective scale and a single integration point in the bituminous binding agent for the simple shear boundary condition.

## Chapter 7

# Artificial microstructures on the basis of granulometric data

*This chapter deals with an extension of the algorithm for artificial microstructures introduced in Chapter 6. The generation of artificial microstructures in almost all fields of interest is bound to requirements or even norms and standards. To satisfy these requirements, this chapter shows in detail the capabilities of the introduced algorithm. Based on one mastic asphalt (MA8S) and one porous asphalt (PA8), this chapter gives details about the calculations that are necessary to create microstructures that serve as statistically similar representations and can be used for further mechanical or other simulation. In comparison to a workflow with X-Ray Computed Tomography (XRCT) scans, this procedure is highly flexible and allows the possibility of applying a wide range of statistics to the generated microstructures.*

### 7.1 Introduction

Asphalt concrete in road construction is often defined by granulometric definitions from norms or standards, such as in [1] for the German industry. For a valid simulation of these granulometric microstructures, the previously introduced algorithm (Chapter 6) is used to create the spatial arrangement of mineral aggregates based on granulometric curves without additional X-Ray Computed Tomography (XRCT) data. As basis for these investigations, the phases for solid aggregates  $\varphi^s$ , filler  $\varphi^p$ , bituminous binding agent  $\varphi^b$  and air  $\varphi^g$  are defined with corresponding effective densities  $\rho^{bR} = 1.02 \text{ g/cm}^3$  and  $\rho^{sR} = \rho^{pR} = 2.67 \text{ g/cm}^3$ . The filler phase  $\varphi^p$  is defined as the phase of the solids, which is not represented in a discrete manner in the constructed artificial microstructure. In this chapter we focus on the discrete distribution of  $\varphi^s$ , which comes from the residue of the sieve. To underline the capabilities of the

invented algorithm, we focus on the discrete generation of microstructures for two completely different asphalt concrete types. First, a mastic asphalt (MA8S) and second, a porous asphalt (PA8) [1]. On condition that the given norm in [1] serves as a guideline, we consider the mesh sizes 0.063 mm and 0.71 mm to be filler for the MA8S and mesh sizes between 0.063 mm and 0.25 mm for the PA8, see Table 7.1. This assumption is necessary to guarantee the best possible boundary conditions for the creation of the artificial microstructures. For a better understanding of the given

Table 7.1: Mesh sizes and sieve values for MA8S and PA8 [1].

mesh		MA8S		PA8	
i	[mm]	passing	residue $u_i$	passing	residue $u_i$
1	11.2	1	0.05	1	0.05
2	8.0	0.95	0.125	0.95	0.85
3	5.6	0.825	0.275	0.1	0.025
4	2.0	0.55	0.085	0.075	0.015
5	0.71	0.465	0.145	0.06	0.01
6	0.125	0.32	0.08	0.05	0.01
7	0.063	0.24	0.24	0.04	0.04

and needed numbers for the calculation of all relevant information for the creation of the artificial microstructures, an index  $\diamond_a$  used in this chapter means a value with regard to the complete asphalt concrete and an index  $\diamond_m$  with regard to all mineral aggregates, which are all solids  $\varphi^s$  and filler particles  $\varphi^p$ . Index  $\diamond_c$  belongs to the required cube of the algorithm, which is defined in more detail later in this chapter. As a first start, we again define the sphere volume

$$V_i = \frac{4}{3}\pi \left(\frac{d_i}{2}\right)^3, \quad (7.1)$$

with  $d_i$  being the diameter of the corresponding sphere, for the used Lubachevsky-Stillinger algorithm [49], cf. Chapter 6. Since a lot of parameters in this Chapter are taken from [1], the author highly encourages the reader to compare the numbers used in this Chapter with the numbers given as standard in the literature. Compared to XRCT data, the use of granulometric data requires a lot more precalculations to guarantee a good statistical equivalence to the prescribed norms of the microstructure, but in comparison to real XRCT data, the additional effort is reasonable. The next

section explains in detail the required numbers and defines the necessary formulas for the artificial microstructure.

## 7.2 Parameters for the discrete microstructure

Since some of the values which are necessary for the detailed definition of the algorithm are not given from norms explicitly, calculation of these values from the given ones is necessary. The first required values are the mass fractions with respect to the complete asphalt concrete  $\diamond_a$  for the different phases, which are defined as

$$w_a^p = w_a^{s+p} w_m^p, \quad (7.2)$$

$$w_a^s = w_a^{s+p} - w_a^p, \quad (7.3)$$

$$w_a^f = w_a^{b+p} = w_a^b + w_a^p. \quad (7.4)$$

The upper index  $\diamond^f$  defines, as in some chapters before, the compound of the pure bituminous binder  $\varphi^b$  and the fine filler particles  $\varphi^p$ . To identify the real volume for the algorithm, consideration of a fictive volume for the asphalt concrete has to take place. This means, calculation of the exact volume fraction for each constituent, whereas the volume fraction of the gaseous phase in the asphalt concrete compound  $n_a^g$  is given from the type of asphalt concrete that we consider. For all other constituents, the volume fraction is derived via

$$n_a^s = \frac{w_a^s / \rho^{sR}}{w_a^s / \rho^{sR} + w_a^p / \rho^{pR} + w_a^b / \rho^{bR}} (1 - n_a^g), \quad (7.5)$$

$$n_a^p = \frac{w_a^p / \rho^{pR}}{w_a^s / \rho^{sR} + w_a^p / \rho^{pR} + w_a^b / \rho^{bR}} (1 - n_a^g), \quad (7.6)$$

$$n_a^b = \frac{w_a^b / \rho^{bR}}{w_a^s / \rho^{sR} + w_a^p / \rho^{pR} + w_a^b / \rho^{bR}} (1 - n_a^g). \quad (7.7)$$

On the basis of the different volume fraction we now focus on the number of discrete particles  $N_i$  that need to be modeled, where  $i$  defines the sieve number and  $N = \sum N_i$  the total number of all particles. Considering  $N_1$  to be the largest particle size and setting the number to  $N_i = 1$  for  $i = 1$ , all further numbers are calculated as

$$N_i = \frac{N_{i-1} V_{i-1}}{u_{i-1}} \frac{u_i}{V_i}, \quad \text{for } i = 2, 3, 4 \quad \text{with} \quad (7.8)$$

$$d_1 > d_2 > \dots, > d_i, \quad i = 1, 2, \dots, 4. \quad (7.9)$$

In the given formula,  $u_i$  defines the residue in the specific sieve size, which is defined by the type of asphalt concrete (here MA8S or PA8), see Table 7.1. Although the residue  $u_i$  in the before presented formula is related to the specific volume and number of each sphere, the residue can be interpreted as a mass fraction as well. In the end,  $u_i$  is a percentage and considering only one material makes it independent of the density, which is the same for all particle sizes. For the next step we need to consider a cubic

domain which we refer to with index  $\diamond_c$  and we define the volume of the discrete mineral aggregates within this cubic domain as

$$v_c^s = \sum V_i N_i. \quad (7.10)$$

For all three other constituents  $\varphi^b$ ,  $\varphi^p$  and  $\varphi^g$  we derive the volume of the sum of all with

$$v_c^{b+p+g} = \frac{v_c^s}{v_a^s} (v_a^b + v_a^p + v_a^g), \quad (7.11)$$

which leads to the complete volume of the cubic domain

$$v_c = v_c^s + v_c^{b+p+g}. \quad (7.12)$$

At this point, the actual volume of the cubic domain  $v_c$  is known and the calculation of relative numbers like volume fractions for the different phases  $n_c^\alpha = dv_c^\alpha/dv_c$  with  $\alpha = \{b, g, p, s\}$ , for the cubic domain, is possible.

Another important value that is triggered with the artificial microstructure algorithm, is the volume of the filler in the newly calculated cubic domain

$$v_c^p = n_a^p v_c. \quad (7.13)$$

With these informations at hand, the absolute volume of solids and filler reads

$$v_c^{s+p} = v_c^s + v_c^p \quad (7.14)$$

and the length of a side of the cube is

$$l_c = v_c^{1/3}. \quad (7.15)$$

With all these formulas, the artificial creation of different asphalt concrete types is possible. As already mentioned before, this chapter focuses on the a mastic asphalt (MA8S) and a porous asphalt (PA8). The next section shows the explicit calculation results for these two asphalt concrete types and furthermore, compares the artificial results with the given standard.

### 7.3 Results and Discussion

As an overview of the calculated and given values, Table 7.2 lists the values for the two considered asphalt concretes. For a better understanding, the given values from [1] are marked as bold symbols. The calculated values are printed in normal style.

Considering our two specific asphalt concrete types (MA8S and PA8) and presuming only one large particle  $N_1 = 1$  due to the restricted size of the modeling domain for both presented asphalt concrete types, the number of all discretely modeled particles are listed in Table 7.3. As a last summary for all calculated values, we derive the information listed in Table 7.4, which contains the specific values for our SVE or cube  $\diamond_c$

Table 7.2: Given values are marked with blue color, all other values are derived.

	$w_a^{s+p}$	$w_a^b$	$w_m^p$	$n_a^g$	$w_a^p$	$w_a^s$	$w_a^{b+p}$	$n_a^s$	$n_a^p$	$n_a^b$
MA8S	0.930	0.070	0.465	0.000	0.432	0.498	0.502	0.446	0.166	0.388
PA8	0.935	0.065	0.060	0.242	0.056	0.879	0.121	0.602	0.117	0.038

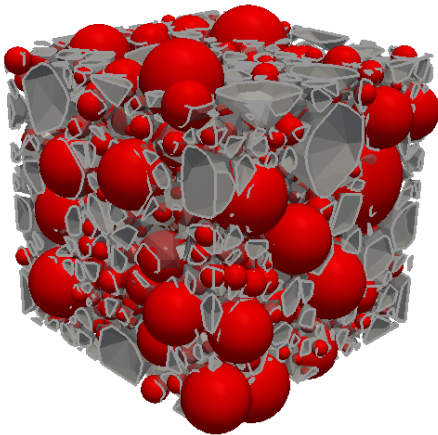
Table 7.3: Discretely modeled particles.

			MA8S		PA8	
i	$d_i$ [mm]	$V_i$ [mm <sup>3</sup> ]	$N_i$	$V_i N_i$ [mm <sup>3</sup> ]	$N_i$	$V_i N_i$ [mm <sup>3</sup> ]
1	9.6	463.25	1	463.25	1	463.25
2	6.8	164.64	7	1158.12	48	7878.19
3	3.8	28.73	89	2547.86	8	231.62
4	1.355	1.30	605	787.52	107	138.97

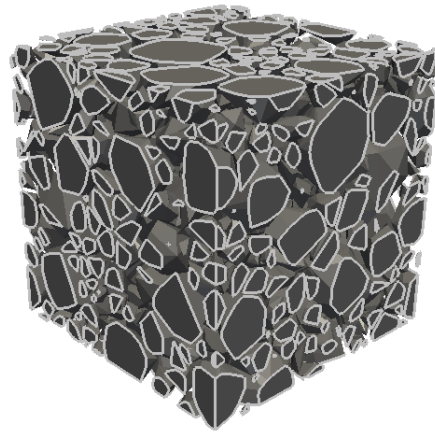
in SI units. For a better understanding and to visualize the steps of the algorithm, Figure 7.1 presents the dense sphere packing in terms of the Lubachevsky-Stillinger algorithm [49, 58] and the shrunk Voronoi cells. The spheres have a single representation under periodic conditions, whereas the Voronoi cells visualize the periodicity of the SVE as status quo. Figure 7.2 shows the upper and lower bounds for the granulometric curve of the MA8S and PA8 asphalt concrete [1] and the granulometric curve of the discretely modeled particles from the invented algorithm. As typically used for granulometric curves in the road building community, the unit of the mass fraction is here abbreviated as M.-%. The modeled particles stay within the bounds and reflect a good similarity with a potential real specimen. Referring to the step-wise character of the MA8S curve in Figure 7.2 a), this comes from the nature of the implemented algorithm and the requirement of different classes of particles sizes, comparable to the mesh sizes for the real specimen. If needed, the number of classes can easily be adjusted within the code, but this accompanies a computational expense. In a further step, these microstructures can be used e.g. for numerical simulations or geometrical analysis.

Table 7.4: Absolute values for MA8S and PA8 depending on the number of mineral aggregates.

	MA8S	PA8
$N$	702	164
$v_c^s$ [mm] <sup>3</sup>	4956.74	8709.04
$v_c^{b+p+g}$ [mm] <sup>3</sup>	6145.38	5752.40
$v_c$ [mm] <sup>3</sup>	11102.12	14461.44
$v_c^p$ [mm] <sup>3</sup>	4308.19	555.90
$v_c^{s+p}$ [mm] <sup>3</sup>	9264.93	9264.93
$l_c$ [mm]	22.30	24.36



a)



b)

Figure 7.1: a) The densely packed spheres after the Lubachevsky-Stillinger algorithm and their representation after the shrinking procedure of the weighted Voronoi diagram. b) The final microstructure for the mastic asphalt concrete MA8S with  $N = 605$  discretely modeled particles.

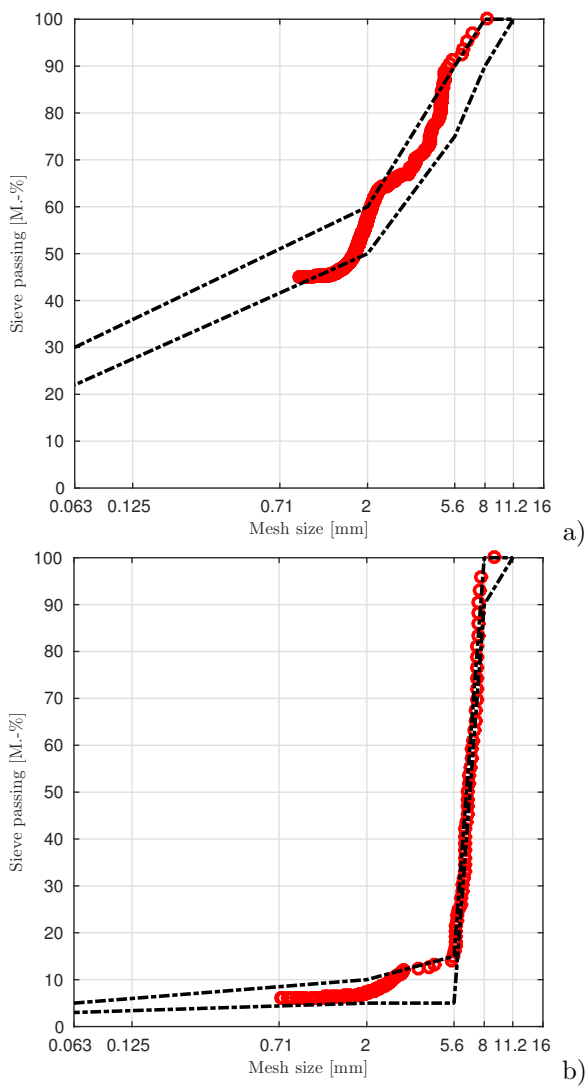


Figure 7.2: Discretely modeled particles and requirements for a) the MA8S and b) the PA8 asphalt concrete.



## Chapter 8

# Conclusions and outlook

The scope of this work was to model and numerically investigate asphalt concrete from a micro- and macro-scale point of view and to investigate the morphological conditions within the compound. Some background information and motivation concerning asphalt concrete was given in Chapter 1. After that, Chapter 2 and 3 were focused on the theoretical framework, in particular kinematics, balance equations and constitutive modeling.

The core part of this thesis starts with Chapter 4, which was concerned with the micro-scale behavior of bitumen-filler mastics and the workflow from experimental data to an extended master-curve concept. In dependency of filler concentration and frequency, the extension was conducted on the basis of broad experimental Dynamic Shear Rheometer (DSR) data for one specific bitumen-filler combination. The presented workflow was motivated by the observation that the experimental data showed self similar master-curves for the different filler concentrations. With the classical WLF function (William, Landel, and Ferry) and its shift factor  $\alpha_\theta$ , the described approach was introduced as an extension with a second shift factor  $\beta_p$ . With this second shift factor the presented procedure allowed to define a generalized master-curve with respect to temperature  $\theta$  and filler mass fraction  $w^p$ . This was conducted on the basis of a single set of experimental data for a bituminous binding agent, in this case 20/30 penetration grade bituminous binder. The defined function for  $\beta_p$  and the experimental data showed a very good agreement and it is to be noted that the presented workflow can easily be applied to any other thermo-rheologically simple bitumen-filler mastic.

The study presented in Chapter 5 dealt with the derivation of effective material properties of viscoelastic compounds by homogenization. In the sense of a mean-field theory a heterogeneous elastic/viscoelastic compound on the micro-level was replaced by an overall homogeneous viscoelastic medium on the macro-level using volume averaging techniques. Based on data acquired for the constituents of asphalt concrete, material studies were carried out to measure the viscoelastic material properties of the bituminous binder, applying the master-curve concept. Knowing

the linear-elastic properties of the mineral filler, an artificially simplified heterogeneous elastic/viscoelastic compound was set up. Following this, a qualitative study with regard of different aspects of classical homogenization techniques for viscoelastic material properties on both, micro- and macro-scale, was carried out with easily manageable computational effort. One key finding of these numerical investigations was that the micro-scale boundary conditions strongly dominate the effective frequency dependent properties of the investigated compound. On the one hand, the character of pure Dirichlet and Neumann boundary conditions as upper and lower bounds for the resulting effective stiffness in the equilibrium state have been confirmed. On the other hand, the impact on the viscous, frequency dependent properties has turned out to be even more dramatic. Constant traction (Neumann) and periodic boundary conditions have been found to result in material responses in the frequency domain similar to the pure bituminous binder. By contrast, the effective characteristic frequency of the compound under locally pure linear displacement (Dirichlet) boundary conditions could not be observed within the investigated frequency range. Another key finding was the determination of the effective viscoelastic properties over several decades in frequency space for the simplified compound consisting of spherical filler particles accounting for about 45% volume fraction.

A final statement concerning the choice of boundary conditions on the micro-level and its high importance was also made. First, it was shown that the choice influences the effective properties in a way that the equilibrium processes are predicted stiffer or softer, which is also known as the upper and lower limit on the effective stiffness (Voigt and Reuss bounds). Second, it was shown that the non-equilibrium processes are as well affected by an effective shift of the critical frequency. For this purpose, it was stated that a thorough discussion of boundary formulations is necessary, in particular for more complex microstructures, which generally do not show any periodic properties e. g. from X-Ray Computed Tomography (XRCT) data.

In connection with this, Chapter 6 presented a workflow, which described the way from XRCT data towards numerical investigations of Statistical Volume Elements (SVEs) for asphalt concrete. This approach circumvents the difficulty on non-periodic microstructures mentioned before. The described workflow includes a novel algorithm to create artificial and simplified microstructures which allow for efficient 3-dim numerical simulations. Starting point was the extraction of essential microstructural parameters from XRCT data, namely the volume fractions of the particular constituents and the particle size distribution of the mineral aggregate phase. In a first step, a discrete particle dynamics technique to generate dense sphere packings was applied. In a second step, the center coordinates of the spheres were used as seed points and the individual radii of the dense sphere packing were used as growth rate to accomplish a weighted Voronoi tessellation. The resulting Voronoi cells were considered as precursor cells for the mineral aggregates. However, due to the nature of the Voronoi technique, the volume fraction of the cells was adapted. The last step in the algorithm was presented as a stochastic shrinking of the individual Voronoi cells to trigger the correct volume fraction of the mineral aggregates. It was stated that the

---

volume between the mineral aggregates is filled by the bituminous binding agent and by using this generation technique, even nonstandard particle size distributions can be reproduced reliably. Furthermore, the basic data for this algorithm not necessarily needs to be XRCT data, as Chapter 7 showed. In general, this tool is highly flexible and the resulting artificial and simplified microstructures are accessible for realistic 3-dim simulation scenarios with reasonable numerical efforts.

Chapter 6 also discussed the 3-dim numerical simulations. Material properties to the mineral aggregates and to the bituminous binding agent were assigned and constitutive behavior discussed. Linear elasticity was used for the mineral aggregates with material parameters known from literature, whereas moderate but finite deformations for the bituminous phase were assumed. The binding agent was therefore described by a nonlinear generalized Maxwell-Zener model. The required material parameters were, as in the chapters before, gained from physical testing on a Dynamic Shear Rheometer. 3-dim numerical simulations were carried out successfully with almost identical volume fractions and particle size distributions but with statistically generated and arranged mineral aggregates. Stress relaxation tests were the focus of this study. Within this study it was found that the microstructure's morphology significantly influences the individual relaxation behavior, which was explained by the distinct localization of the viscous activity in the narrow regions between neighboring mineral aggregates varying from microstructure to microstructure. Another conclusion drawn was that the nonlinear description is only required at very small volume fractions. The study compared the linear and nonlinear viscoelasticity formulations over identical SVEs and it was found that the effective material properties as volume averages of their microscopic counterparts result in identical relaxation curves. In other words it was stated that a geometrically linear description on the micro-level is sufficient for small deformations applied on the large scale. Any kind of rearrangements of the mineral aggregates during the deformation process were not observed, but need to be considered when finite deformations are applied on the macro-level.

Finally an extension to the algorithm introduced in Chapter 6 was presented in Chapter 7. Based on the fact that the generation of artificial microstructures in almost all fields of interest is bound to requirements or even norms and standards, the capabilities of the algorithm with regard to these boundary conditions were shown in detail. The capabilities were shown exemplary for one mastic asphalt (MA8S) and one porous asphalt (PA8). Details about the necessary calculations to create these microstructures were given and in comparison to a workflow with XRCT scans, it was shown that this procedure is highly flexible and allows the application of statistics to the generated microstructures.

As an outlook it is to note that some important aspects were not covered within this thesis. For example, the fact that the proposed generation tool is restricted to the description of mastic asphalt concrete or only the mineral aggregate part of a porous asphalt. In future investigations it would be of high interest to cover air voids within the compound to extend the range of possible applications for this tool and the subsequent numerical simulations to even more asphalt concrete types. Another field of

interest building on this thesis is the possibility to include other methods to investigate the overall mechanical properties of the compound, for example order reduction methods to create substitute models [20, 39, 66].

Concluding this thesis, the presented interpretation of experimental data, the extension of the master curve concept, the study concerning boundary conditions and constitutive modeling in combination with the novel algorithm to create artificial and simplified microstructures, lead to a deeper physical understanding of the behavior of asphalt concrete. The thesis showed a thorough examination of asphalt concrete from the experimental determination of single constituents right up to 3-dim simulations of the compound.

# Chapter A

## APPENDIX

### A.1 Linear-viscoelasticity

This part of the appendix is concerned with the different formulation for the angular frequency-dependent elastic moduli  $C(\omega)$  within the Finite Difference method as presented in [68] and the shown approach in this thesis according to the Finite Element method. To recall the presented formulation in this thesis, see Eq. (3.32) and Eq. (3.82) for the 0-dim and the 3-dim case respectively.

## One-dimensional

To check if both expressions are the same, the reference formulation for the Finite Difference method is taken from [68]. The angular frequency-dependent elastic moduli  $C(\omega)$  in the Finite Difference scheme are given as

$$C(\omega)_{0-dim}^{FDM} = E_0 + E_1 - E_1 \frac{\omega_m}{i\omega + \omega_m}. \quad (\text{A.1})$$

Proof that both expressions are the same in a 0-dim formulation with  $C(\omega)_{0-dim}^{FEM}$  as in Eq. (3.32):

$$\begin{aligned} C(\omega)_{0-dim}^{FDM} &= C(\omega)_{0-dim}^{FEM} \\ E_0 + E_1 - E_1 \frac{\omega_m}{i\omega + \omega_m} &= E_0 + \frac{\omega^2 E_1 + i\omega \omega_m E_1}{\omega^2 + \omega_m^2} \\ E_1 - E_1 \frac{\omega_m}{i\omega + \omega_m} &= \frac{\omega^2 E_1 + i\omega \omega_m E_1}{\omega^2 + \omega_m^2} \\ E_1 \frac{i\omega + \omega_m}{i\omega + \omega_m} - E_1 \frac{\omega_m}{i\omega + \omega_m} &= \frac{\omega^2 E_1 + i\omega \omega_m E_1}{\omega^2 + \omega_m^2} \\ E_1 \frac{i\omega}{i\omega + \omega_m} &= \frac{\omega^2 E_1 + i\omega \omega_m E_1}{\omega^2 + \omega_m^2} \\ \frac{E_1 i\omega (i\omega - \omega_m)}{(i\omega + \omega_m)(i\omega - \omega_m)} &= \frac{\omega^2 E_1 + i\omega \omega_m E_1}{\omega^2 + \omega_m^2} \\ \frac{-E_1 \omega^2 - E_1 i\omega \omega_m}{-\omega^2 - \omega_m^2} &= \frac{\omega^2 E_1 + i\omega \omega_m E_1}{\omega^2 + \omega_m^2} \\ \frac{\omega^2 E_1 + i\omega \omega_m E_1}{\omega^2 + \omega_m^2} &= \frac{\omega^2 E_1 + i\omega \omega_m E_1}{\omega^2 + \omega_m^2} \quad \checkmark \end{aligned}$$

### Three-dimensional

The procedure for the 3-dim formulation is similar and presented here with the angular frequency-dependent elastic moduli  $C(\omega)$  in the Finite Difference scheme given as

$$C(\omega)_{3-dim}^{FDM} = 2 E_0 + 2 E_1 - 2 E_1 \frac{2 \omega_m}{i \omega + 2 \omega_m}. \quad (\text{A.2})$$

Proof that both expressions are the same in a 3-dim formulation with  $C(\omega)_{3-dim}^{FEM}$  as in Eq. (3.82)::

$$\begin{aligned} C(\omega)_{3-dim}^{FDM} &= C(\omega)_{3-dim}^{FEM} \\ 2 E_0 + 2 E_1 - 2 E_1 \frac{2 \omega_m}{i \omega + 2 \omega_m} &= 2 E_0 + \frac{\omega^2 2 E_1 + i \omega \omega_m 4 E_1}{\omega^2 + 4 \omega_m^2} \\ 2 E_1 - 2 E_1 \frac{2 \omega_m}{i \omega + 2 \omega_m} &= \frac{\omega^2 2 E_1 + i \omega \omega_m 4 E_1}{\omega^2 + 4 \omega_m^2} \\ 2 E_1 \frac{i \omega + 2 \omega_m}{i \omega + 2 \omega_m} - 2 E_1 \frac{2 \omega_m}{i \omega + 2 \omega_m} &= \frac{\omega^2 2 E_1 + i \omega \omega_m 4 E_1}{\omega^2 + 4 \omega_m^2} \\ 2 E_1 \frac{i \omega}{i \omega + 2 \omega_m} &= \frac{\omega^2 2 E_1 + i \omega \omega_m 4 E_1}{\omega^2 + 4 \omega_m^2} \\ \frac{2 E_1 i \omega (i \omega - 2 \omega_m)}{(i \omega + 2 \omega_m) (i \omega - 2 \omega_m)} &= \frac{\omega^2 2 E_1 + i \omega \omega_m 4 E_1}{\omega^2 + 4 \omega_m^2} \\ \frac{-2 E_1 \omega^2 - 4 E_1 i \omega \omega_m}{-\omega^2 - 4 \omega_m^2} &= \frac{\omega^2 2 E_1 + i \omega \omega_m 4 E_1}{\omega^2 + 4 \omega_m^2} \\ \frac{\omega^2 2 E_1 + i \omega \omega_m 4 E_1}{\omega^2 + 4 \omega_m^2} &= \frac{\omega^2 2 E_1 + i \omega \omega_m 4 E_1}{\omega^2 + 4 \omega_m^2} \quad \checkmark \end{aligned}$$



# Bibliography

- [1] Forschungsgesellschaft für Straßen- und Verkehrswesen, Technische Lieferbedingungen für Asphaltmischgut für den Bau von Verkehrsflächenbefestigungen, (TL Asphalt-StB 07), Arbeitsgruppe Asphaltbauweisen (2007).
- [2] D. Anderson and W. Goetz, Mechanical behavior and reinforcement of mineral filler-asphalt mixtures, *Journal of the Association of Asphalt Paving Technologists* **42**, 37–66 (1973).
- [3] F. Aurenhammer, Power Diagrams: Properties, Algorithms and Applications, *SIAM Journal on Computing* **16**, 78–96 (1987).
- [4] F. Aurenhammer and H. Imai, Geometric relations among Voronoi diagrams, *Geometriae Dedicata* **27**, 65–75 (1988).
- [5] F. Cardone, F. Frigio, G. Ferrotti, and F. Canestrari, Influence of mineral fillers on the rheological response of polymer-modified bitumens and mastics, *Journal of Traffic and Transportation Engineering (English Edition)* **2**, 373–381 (2015).
- [6] J. Chong, E. Christiansen, and A. Baer, Rheology of concentrated suspensions, *Journal of Applied Polymer Science* **15**, 2007–2021 (1971).
- [7] E. Coleri, J. T. Harvey, K. Yang, and J. M. Boone, Development of a micromechanical finite element model from computed tomography images for shear modulus simulation of asphalt mixtures, *Construction and Building Materials* **30**, 783–793 (2012).
- [8] E. Dickinson and H. Witt, The dynamic shear modulus of paving asphalts as a function of frequency, *Journal of Rheology* **18**, 591–606 (1974).
- [9] A. Donev, S. Torquato, and F. H. Stillinger, Neighbor List Collision-driven Molecular Dynamics Simulation for Nonspherical Hard Particles. I. Algorithmic Details, *Journal of Computational Physics* **202**, 737–764 (2005).
- [10] D. A. Drew and S. L. Passman, *Theory of multicomponent fluids* (Springer, New York, 1999).

- 
- [11] A. Einstein, Eine neue Bestimmung der Moleküldimensionen, *Annalen der Physik* **19**, 289–306 (1906).
- [12] A. Faheem and H. Bahia, Conceptual phenomenological model for interaction of asphalt binders with mineral fillers, *Asphalt Paving Technology-Proceedings* **78**, 679–720 (2009).
- [13] A. Faheem, H. Wen, L. Stephenson, and H. Bahia, Effect of mineral filler on damage resistance characteristics of asphalt binders, *Asphalt Paving Technology-Proceedings* **77**, 885–907 (2008).
- [14] J. Ferry, *Viscoelastic properties of polymers* (John Wiley & Sons, New York, 1980).
- [15] F. Feyel and J.L. Chaboche, FE<sup>2</sup> multiscale approach for modelling the elastoviscoplastic behaviour of long fiber SiC/Ti composite materials, *Computer Methods in Applied Mechanics and Engineering* **183**, 309–330 (2000).
- [16] J. Fish, K. Shek, M. Pandheeradi, and M. S. Shephard, Computational plasticity for composite structures based on mathematical homogenization: Theory and practice, *Computer Methods in Applied Mechanics and Engineering* **148**, 53–73 (1997).
- [17] F. Fritzen and T. Böhlke, Periodic three-dimensional mesh generation for particle reinforced composites with application to metal matrix composites, *International Journal of Solids and Structures* **48**, 706–718 (2011).
- [18] F. Fritzen, T. Böhlke, and E. Schnack, Periodic three-dimensional mesh generation for crystalline aggregates based on Voronoi tessellations, *Computational Mechanics* **43**, 701–713 (2009).
- [19] F. Fritzen, S. Forest, T. Böhlke, D. Kondo, and T. Kanit, Computational homogenization of elasto-plastic porous metals, *International Journal of Plasticity* **29**, 102–119 (2012).
- [20] F. Fritzen and T. Böhlke, Reduced basis homogenization of viscoelastic composites, *Composites Science and Technology* **76**, 84–91 (2013).
- [21] E. Ghossein and M. Lévesque, A fully automated numerical tool for a comprehensive validation of homogenization models and its application to spherical particles reinforced composites, *International Journal of Solids and Structures* **49**, 1387–1398 (2012).
- [22] R. Greeve, *Kontinuumsmechanik. Ein Grundkurs* (Springer, Berlin, 2003).
- [23] Z. Gurocak, S. Alemdag, and M. Zaman, Rock slope stability and excavatability assessment of rocks at the Kapikaya dam site, Turkey, *Engineering Geology* **96**, 17–27 (2007).

- [24] Z. Hashin and S. Shtrikman, A variational approach to the theory of the elastic behaviour of multiphase materials, *Journal of the Mechanics and Physics of Solids* **11**, 127–140 (1963).
- [25] P. Haupt, *Continuum Mechanics and Theory of Materials* (Springer, Berlin Heidelberg, 2002).
- [26] E. Hesami, D. Jelagin, N. Kringos, and B. Birgisson, An empirical framework for determining asphalt mastic viscosity as a function of mineral filler concentration, *Construction and Building Materials* **35**, 23–29 (2012).
- [27] W. Heukelom, The role the filler in bituminous mixes, *Journal of the Association of Asphalt Paving Technologists* **35**, 558–399 (1965).
- [28] R. Hill, Elastic properties of reinforced solids: Some theoretical principles, *Journal of the Mechanics and Physics of Solids* **11**, 357–372 (1963).
- [29] R. Hill, On constitutive macro-variables for heterogeneous solids at finite strain, *Proceedings of the Royal Society of London A* **326**, 131–147 (1972).
- [30] G. A. Holzapfel, *Nonlinear Solid Mechanics* (Wiley Chichester, 2000).
- [31] C. Huet, Etude par une méthode d'impédance du comportement viscoélastique des matériaux hydrocarbonés, PhD-thesis (Faculté des Sciences de l'Université de Paris, Paris, 1963).
- [32] H. Hürtgen, Bestimmung des Elastizitätsmoduls von Asphalt aus konventionellen Mischgut- und Bindemitteldaten, *Bitumen* **2**, 52–58 (1982).
- [33] S. Huschek and C. Angst, Mechanical properties of filler-bitumen mixes at high and low service temperatures, *Journal of the Association of Asphalt Paving Technologists* **49**, 440–475 (1965).
- [34] J. Hutschenreuther and T. Wörner, *Asphalt im Strassenbau* (Verlag für Bauwesen, Berlin, 1998).
- [35] I. Ishai and J. Craus, Effect of the filler on aggregate-bitumen adhesion properties in bituminous mixtures, *Journal of the Association of Asphalt Paving Technologists* **46**, 228–258 (1977).
- [36] R. Jänicke, *Micromorphic media: Interpretation by homogenisation*, PhD-thesis (<http://scidok.sulb.uni-saarland.de/volltexte/2010/3209>) (Shaker Verlag, Aachen, 2010).
- [37] R. Jänicke, F. Larsson, K. Runesson, and H. Steeb, Numerical identification of a viscoelastic substitute model for heterogeneous poroelastic media by a reduced order homogenization approach, *Computer Methods in Applied Mechanics and Engineering* **298**, 108–120 (2016).

- [38] R. Jänicke and H. Steeb, Minimal loading conditions for higher order numerical homogenisation schemes, *Archive of Applied Mechanics* **80**, 1075–1088 (2012).
- [39] R. Jänicke, F. Larsson, K. Runesson, and H. Steeb, Numerical identification of a viscoelastic substitute model for heterogeneous poroelastic media by a reduced order homogenization approach, *Computer Methods in Applied Mechanics and Engineering* **298**, 108–120 (2016).
- [40] T. Kanit, S. Forest, I. Galliet, V. Mounoury, and D. Jeulin, Determination of the size of the representative volume element for random composites: statistical and numerical approach, *International Journal of Solids and Structures* **40**, 3647–3679 (2003).
- [41] A. Kavussi and R. Hicks, Properties of bituminous mixtures containing different fillers, *Journal of the Association of Asphalt Paving Technologists* **66**, 153–186 (1997).
- [42] Y. Kim and D. Little, Linear viscoelastic analysis of asphalt mastics, *Journal of Materials in Civil Engineering* **16**, 122–132 (2004).
- [43] V. G. Kouznetsova, W. A. M. Brekelmans, and F. P. T. Baaijens, An approach to micro-macro modeling of heterogeneous materials, *Computational Mechanics* **27**, 37–48 (2001).
- [44] J. Krishnan and K. Rajagopal, On the mechanical behaviour of asphalt, *Mechanics of Materials* **37**, 1085–1100 (2005).
- [45] E. Kröner, Allgemeine Kontinuumstheorie der Versetzungen und Eigenspannungen, *Archive for Rational Mechanics and Analysis* **4**, 273–334 (1959).
- [46] F. Lavergne, R. Brenner, and K. Sab, Effects of grain size distribution and stress heterogeneity on yield stress of polycrystals: A numerical approach, *Computational Materials Science* **77**, 387–398 (2013).
- [47] E. H. Lee, Elastic-plastic deformation at finite strains, *Journal of Applied Mechanics* **36**, 1–6 (1969).
- [48] E. H. Lee and D. T. Liu, Finite strain elastic plastic theory with application to plane wave analysis, *Journal of Applied Physics* **38**, 19–27 (1967).
- [49] B. Lubachevsky and F. Stillinger, Geometric properties of random disk packings, *Journal of Statistical Physics* **60**, 561–583 (1990).
- [50] J. Lubliner, *Plasticity Theory* (Macmillan Publishing Company, New York, 1990).
- [51] C. Macosko, *Rheology: Principles, Measurements, and Applications (Advances in Interfacial Engineering)* (Wiley-VCH, New York, Chichester, 1994).

- [52] V. Magnanimo, H. ter Huerne, and S. Luding, Modeling of asphalt durability and self-healing with discrete particles method, Proceedings of the 5th Eurasphalt and Eurobitume Congress pp. 1–10 (2012).
- [53] S.D. Mesarovic and J. Padbidri, Minimal kinematic boundary conditions for simulations of disordered microstructures, Philosophical Magazine **85**, 65–78 (2005).
- [54] J.C. Michel, H. Moulinec, and P. Suquet, Effective properties of composite materials with periodic microstructure: A computational approach, Computer Methods in Applied Mechanics and Engineering **172**, 109–143 (1999).
- [55] C. Miehe and A. Koch, Computational micro-to-macro transitions of discretized microstructures undergoing small strains, Archive of Applied Mechanics **72**, 300–317 (2002).
- [56] S. Nemat-Nasser and M. Hori, Micromechanics: overall properties of heterogeneous solids (Amsterdam New York North-Holland, 1993).
- [57] M. Oeser and S. Freitag, Fractional derivatives and recurrent neural networks in rheological modelling – Part I: Theory, International Journal of Pavement Engineering **17**, 87–102 (2015).
- [58] V. Ogarko and S. Luding, A fast multilevel algorithm for contact detection of arbitrarily polydisperse objects, Computer Physics Communications **183**, 931–936 (2012).
- [59] I. Onifade, D. Jelagin, A. Guarin, B. Birgisson, and N. Kringos, Asphalt internal structure characterization with X-ray computed tomography and digital image processing, in: Multi-Scale Modeling and Characterization of Infrastructure Materials, edited by N. Kringos, B. Birgisson, D. Frost, and L. Wang, RILEM Bookseries Vol. 8 (Springer Netherlands, 2013), pp. 139–158.
- [60] T. Ormel, V. Magnanimo, H. ter Huerne, and S. Luding, Modeling of asphalt and experiments with a discrete particles method, Proceedings of the 7th International Conference on Maintenance and Rehabilitation of Pavements and Technological Control pp. 1–10 (2012).
- [61] M. Ostoja-Starzewski, Material spatial randomness: From statistical to representative volume element, Probabilistic Engineering Mechanics **21**, 112–132 (2006).
- [62] B. Quintal, H. Steeb, M. Frehner, and S.M. Schmalholz, Quasi-static finite element modeling of seismic attenuation and dispersion due to wave-induced fluid flow in poroelastic media, Journal of Geophysical Research **116**, 2156–2202 (2011).

- [63] D. A. Ramirez Cardona, S. Pouget, H. Di Benedetto, and F. A. Olard, Viscoelastic behaviour characterization of a gap-graded asphalt mixture with sbs polymer modified bitumen, *Materials Research* **18**, 373–381 (2015).
- [64] R. Recasens, A. Martínez, F. Jiménez, and H. Bianchetto, Effect of filler on the aging potential of asphalt mixtures, *Transportation Research Record: Journal of the Transportation Research Board* **1901**, 10–17 (2005).
- [65] P. J. Rigden, The use of fillers in bituminous road surfacings. a study of filler-binder systems in relation to filler characteristics, *Journal of the Society of Chemical Industry* **66**, 299–309 (1947).
- [66] S. Roussette, J. Michel, and P. Suquet, Nonuniform transformation field analysis of elastic–viscoplastic composites, *Composites Science and Technology* **69**, 22–27 (2009).
- [67] C. H. Rycroft, Voropp: A three-dimensional Voronoi cell library in C++, *Chaos: An Interdisciplinary Journal of Nonlinear Science* **19** (2009).
- [68] E. Saenger, F. Enzmann, Y. Keehm, and H. Steeb, Digital rock physics: Effect of fluid viscosity on effective elastic properties, *Journal of Applied Geophysics* **74**, 236–241 (2011).
- [69] E. Sanchez-Palencia, *Non-homogeneous Media and Vibration Theory*, Lecture Notes in Physics, No. 127 (Springer, Berlin, 1980).
- [70] G. Sayegh, Variation des modules de quelques bitumes purs et enrobeés bitumineux (PhD-thesis (Faculté des Sciences de l’Université de Paris, Paris (in French), 1965).
- [71] J. Schröder, D. Balzani, and D. Brands, Approximation of random microstructures by periodic statistically similar representative volume elements based on lineal-path functions, *Application and Applied Mathematics* **81**, 975–997 (2011).
- [72] T. Schüler, R. Manke, R. Jänicke, M. Radenberg, and H. Steeb, Multi-scale modelling of elastic/viscoelastic compounds, *ZAMM - Journal of Applied Mathematics and Mechanics* **93**, 126–137 (2013).
- [73] T. Schüler, R. Jänicke, and H. Steeb, Bituminous asphalt concrete: Aspects on scale-bridging, *Proceedings in Applied Mathematics and Mechanics* **12**, 333–334 (2012).
- [74] T. Schüler, R. Jänicke, and H. Steeb, Asphalt concrete: From micro-CT scans towards multiscale modelling of effective properties, *Proceedings in Applied Mathematics and Mechanics* **14**, 543–544 (2014).

- [75] T. Schüler, R. Jänicke, and H. Steeb, Nonlinear modeling and computational homogenization of asphalt concrete on the basis of XRCT scans, *Construction and Building Materials* **109**, 96–108 (2016).
- [76] H. G. Sehlhorst, R. Jänicke, A. Düster, E. Rank, H. Steeb, and S. Diebels, Numerical investigations of foam-like materials by nested high-order finite element methods, *Computational Mechanics* **45**, 45–59 (2009).
- [77] N. Shashidhar and P. Romero, Factors Affecting the Stiffening Potential of Mineral Fillers, *Journal of the Transportation Research Board* **1638**, 94–100 (1998).
- [78] A. Shenoy, *Rheology of Filled Polymer Systems* (Springer, Netherlands, 1999).
- [79] A. V. Shutov, R. Landgraf, and J. Ihlemann, An explicit solution for implicit time stepping in multiplicative finite strain viscoelasticity, *Computer Methods in Applied Mechanics and Engineering* **265**, 213–225 (2013).
- [80] J. C. Simo and T. J. R. Hughes, *Computational Inelasticity* (Springer-Verlag, New-York, 1998).
- [81] J. Stastna, D. D. Kee, and M. B. Powley, Complex viscosity as a generalized response function, *Journal of Rheology* **29**, 457–469 (1985).
- [82] F. F. Tehrani, J. Absi, F. Allou, and C. Petit, Investigation into the impact of the use of 2D/3D digital models on the numerical calculation of the bituminous composites' complex modulus, *Computational Materials Science* **79**, 377–389 (2013).
- [83] F. F. Tehrani, J. Absi, F. Allou, and C. Petit, Heterogeneous numerical modeling of asphalt concrete through use of a biphasic approach: Porous matrix/inclusions, *Computational Materials Science* **69**, 186–196 (2013).
- [84] K. Terada, T. Miura, and N. Kukuchi, Digital image-based modeling applied to the homogenization analysis of composite materials, *Computational Mechanics* **20**, 331–346 (1997).
- [85] D. Thomas, Transport characteristics of suspension: VIII. A note on the viscosity of Newtonian suspensions of uniform spherical particles, *Journal of Colloid Science* **20**, 267–277 (1965).
- [86] D. Tunicliff, Binding Effects of Mineral Fillers, *Journal of the Association of Asphalt Paving Technologists* **36**, 114–156 (1967).
- [87] S. Velske, H. Mentlein, and P. Eymann, *Strassenbau, Strassenbautechnik* (Werner Verlag, Köln, 2009).
- [88] G. Vinogradov and M. A. Y., *Rheology of Polymers* (Springer, Berlin Heidelberg, 1980).

- 
- [89] L. Wang, *Mechanics of Asphalt: Microstructure and Micromechanics: Microstructure and Micromechanics* (McGraw-Hill Education, 2010).
- [90] J. Wimmer, B. Stier, J. W. Simon, and S. Reese, Computational homogenisation from a 3d finite element model of asphalt concrete - linear elastic computations, *Finite Elements in Analysis and Design* **110**, 43–57 (2016).
- [91] P. Wriggers, *Nonlinear finite element methods* (Springer, Berlin Heidelberg, 2008).
- [92] P. Wriggers and S. Moftah, Mesoscale models for concrete: Homogenisation and damage behaviour, *Finite Elements in Analysis and Design* **42**, 623–636 (2006), The Seventeenth Annual Robert J. Melosh Competition.
- [93] T. You, R. K. A. Al-Rub, M. K. Darabi, E. A. Masad, and D. N. Little, Three-dimensional microstructural modeling of asphalt concrete using a unified viscoelastic–viscoplastic–viscodamage model, *Construction and Building Materials* **28**, 531–548 (2012).
- [94] N. I. M. Yusoff, M. T. Shaw, and G. D. Airey, Modelling the linear viscoelastic rheological properties of bituminous binders, *Construction and Building Materials* **25**, 2171–2189 (2011).
- [95] T. Zohdi and P. Wriggers, *Introduction To Computational Micromechanics, Lecture Notes in Applied and Computational Mechanics* (Springer, Berlin Heidelberg, 2005).

# Curriculum Vitae - Thorsten Schüler

Place and Date of Birth: Essen, Germany — 2 February 1986

## School Education

August 1996 -  
June 2005                      **High school degree**  
Gymnasium Borbeck an der Prinzenstraße  
Essen, Germany

## University Education

October 2006 -  
July 2011                      **Mechanical Engineering**  
Ruhr-Universität Bochum, Germany

April 2009 -  
March 2010                    **Student assistant**  
Chair of Continuum Mechanics  
Ruhr-Universität Bochum, Germany

August 2011 -  
February 2016                **PhD student and research assistant**  
Chair of Continuum Mechanics  
Ruhr-Universität Bochum, Germany

## Non-university Education and Experience

March 2004 -  
April 2004                      **Scholarship**  
Alfried Krupp von Bohlen and Halbach-Foundation  
Internship at T-Mobile UK  
Sunderland, England

September 2005 -  
May 2006                      **Civil Service**  
Alten- und Pflegeheim Haus Abendfrieden  
Oberhausen, Germany

July 2006 -  
August 2006                    **Internship**  
TMD Friction EsCo GmbH  
Essen, Germany

April 2010 -  
May 2010                      **Internship**  
Salzgitter Mannesmann Forschung GmbH  
Duisburg, Germany

June 2010 -  
December 2010                **Student research project and internship**  
Texas A&M University  
College Station, USA

since March 2016              **Calculation engineer**  
Siemens AG  
Mülheim an der Ruhr, Germany

**Mitteilungen aus dem Institut für Mechanik  
RUHR-UNIVERSITÄT BOCHUM  
Nr. 174**

**ISBN 978-3-935892-52-0**